Simultaneous Magneto-Optical Trapping of Ytterbium and Caesium

Ruben Freytag

Department of Physics

Imperial College London

Thesis submitted in partial fulfilment of
the requirements for the degree

Doctor of Philosophy

July 2015

Declaration of originality

I declare that the work presented in this thesis mainly originated from me. All work obtained from others or with the help of others is clearly indicated throughout the thesis. References are given for all information taken from other sources.

Copyright declaration

Abstract

This thesis presents progress toward the production of ultracold CsYb molecules. To this end, an apparatus capable of producing magneto optical traps of Yb and Cs was designed, built and tested. Both atoms are produced in a dual species oven and both slowed to low speeds by a single Zeeman slower. From the Zeeman slower atoms are captured in a dual-species magneto-optical trap.

To cool caesium the 852 nm D_2 transition is addressed by two lasers for cooling and repump. For ytterbium the 399 nm ${}^1S_0 \rightarrow {}^1P_1$ transition is addressed for the Zeeman slower and the 556 nm ${}^1S_0 \rightarrow {}^3P_1$ transition is addressed for the magneto-optical trap. The 399 nm light is produced by two homebuilt diode lasers in an injection-seeding setup, which can produce up to 100 mW. The 556 nm light is produced from a commercial frequency doubled fiber laser, which can produce up to 260 mW.

The Zeeman slower is characterised experimentally for both Cs and Yb, and the results compared to those of a numerical simulation of the slower for Yb. The velocity distribution exiting the slower is very sensitive to the exact magnetic field profile, the laser power and detuning of the laser light.

The number of atoms loaded into the magneto-optical trap was investigated as a function of the magnetic field gradient, the laser power and the laser detuning. The capture velocity of the Yb MOT is small because the linewidth of the MOT transition is narrow, and so we investigated the influence of broadening the laser linewidth by adding multiple finely-spaced sidebands to the laser light. After optimisation the caesium MOT trapped 5.5×10^8 atoms at $125 \pm 4\,\mu$K. The ytterbium MOT trapped 4.7×10^9 atoms at $81 \pm 2\,\mu$K. Lastly we demonstrate that both MOTs can be produced in the same vacuum chamber simultaneously.

Acknowledgements

First I would like to thank my two supervisors Mike Tarbutt at Imperial College and Simon Cornish at Durham University. Mike has always been helpful and approachable. He has an incredible talent for explaining physics clearly and I learned a lot from him especially in the beginning of my PhD. He has always been happy to spent time and effort in helping out with any problem. Simon has always been very engaged with the work happening on the project and was always available to offer help and guidance. He encouraged me to work rigorously and thereby strongly improved my qualities as an experimental scientist. Without the dedication and commitment of both of them this work would not exist.

I would like thank everyone that contributed to the YbCs project. At Imperial College I worked with Michael Petersen, who showed patience in guiding me during my initial "steps" in the lab. He taught me a lot about working in a laboratory. At Durham I had the pleasure to work Steve Hopkins, who seemingly had an innovative solution for any problem that presented itself. Especially I would like to thank Kirsteen Butler and Stefan Kemp, who were both hard working and dedicated students that helped me wherever they could. Mostly though I am extremely grateful for their company during the many hours spent in lab.

I would also like to thank Jon Dyne and Stephen Maine from the Mechanical Workshop for all the work in constructing the countless parts needed for my experiment and always answering my questions regardless how simple or complicated they were. I would like to thank Val Gerulis for all his help with electronics and his cheerful presence in the lab. Furthermore I would like to thank Lilian Wanjohi, Miranda Smith and Sanja Maricic for all their administrative work and always caring about my progress.

I would also like to thank my friends Didier, Vignesh and Fern. I'm glad I started my PhD with you and could not have asked for better friends.

Fern, our countless midweek pub trips kept me going during the week and I will never forget appearing as a Ninja during your magic trick. Didier, we definitely had the best office in physics and I am grateful for all the help I got from you in lab. Vignesh, I had a lot of fun playing games with you. I remember the hours of playing Uncharted and am very glad I introduced you to board games.

I would also like to thank the UCL, Imperial and Ruislip Handball clubs and all my team mates. Handball has been a big part of my life in London. I have formed many close friendships through handball and would like to mention, Stefan Bauer, Lucas Carstens, Yannick Seis and Tim Zühlsdorff (even though I knew you long before handball).

Lastly I would like to thank my wonderful girlfriend Emma. You have been a strong support and help. You have always been patient with me and the amount of work I had to do. I'm very glad to have met you and that I am moving to Stockholm with you.

Contents

List of Figures

Chapter 1

Introduction

Cold molecules have been proposed and used in a wide variety of experiments serving very different purposes. They have already been successfully used in a number of high precision experiments. Several microwave and millimetre wave transitions of CH radicals have been measured to a high precision, in order to test the hypothesis that the fundamental constants may be varying, which is significant for astrophysics [3, 4]. Similarly, OH molecules have been used to search for a possible time variation of the fine-structure constant [5]. Ultracold molecules on a lattice were used to measure various molecular parameters, which can give insights to the fundamental physics involved in molecular binding energies [6]. Furthermore Cs_2 molecules have been investigated as sensitive probes of a variation in the electron-to-proton mass ratio[7, 8]. Molecules have been used for many years in determining the electron electric dipole moment (EDM) to high precision [9, 10, 11]. Such a measurement is especially important as different fundamental particle theories predict different values for the EDM. A definite measurement of the EDM could therefore eliminate or confirm some possible theories. The most recent experiment uses a cold beam of ThO molecules and finds an upper bound for the electron EDM of $8.7 \times 10^{-29} e$ cm [12].

Other tests of fundamental physics also can be conducted with cold molecules. Molecules can be used to measure parity violations [13]. Studies with lithium molecules have also revealed that molecular collisions do not follow the universal predictions of long-range van der Waals interactions. These effects can be explained through careful analysis of the vibrational states, but were not observed previously [14, 15]. Lechner *et al.* have also proposed using cold molecules to investigate quantum glass phases [16].

When Feynman introduced the idea of a computer based on the fundamental prin-

ciples of quantum mechanics [17], researches started to explore the possibilities of such a system with ultracold atoms. This led to an increased effort to understand strongly-interacting systems [18, 19] and placing ultracold atoms on an optical lattice [20, 21]. While building a universal quantum computer with atoms is still out of reach, an optical lattice could also be used to mimic condensed matter systems [22, 23, 24]. Such a system, known as a quantum simulator, could give some insight into some unexplained physics. Replacing the atoms for molecules allows for stronger long range interactions [25] and should therefore resemble a condensed matter system more closely. Molecules on neighbouring lattice sights are coupled through the dipole-dipole interaction. These interactions can be manipulated and made spin dependent with a microwave field. Such a lattice has been realised with KRb molecules and the spin dependent interactions have been demonstrated [26]. Additionally a quantum computer using polar molecules has been proposed by DeMille [27], which uses molecules on a 1D lattice interacting with an electric field to tune interactions. There have also been proposals to build a hybrid quantum processor where ultracold polar molecules are coupled to superconducting microwave stripline resonators [28]. Here, the rotational state of the polar molecules act as the qubits, while the exchange of quantum information between qubits is via microwave photons in the resonator. All these systems require ultracold molecules, often in an optical lattice. There are several ways to produce such molecules through direct cooling methods or binding ultracold atoms together to form molecules. The different methods are explored in section 1.1. Apart from quantum computing and simulations cold molecules can be used for wide variety of other applications.

The CsYb molecule is especially of interest with respect to the scheme on an optical lattice [25]. As it is a hetero-nuclear molecule it should exhibit a strong electric dipole moment, which is important for engineering the dipole-dipole interactions. Furthermore the ground state CsYb molecule will have a spin, which will allow for spin dependent interactions. A more detailed discussion of why CsYb was chosen is given in section 2.3.3.

1.1 Producing Cold Molecules

With the rising interest in molecular systems an ever increasing number of methods for producing cold molecules have been developed. These methods usually fall in one of two categories. Direct cooling starts with the molecule at room temperature and employs

various techniques to reduce the temperature. Indirect cooling uses established atomic cooling techniques to cool the atoms which will form the molecule. After the atoms are cooled different methods can be employed to bind the atoms together. Direct cooling is in principle more versatile than indirect cooling as many direct cooling methods can be used for a large variety of different molecules. Indirect cooling is restricted to molecules made up from atoms that can be cooled effectively. However, as atomic cooling methods have been developed for a longer time these methods have been able to reach colder temperatures.

1.1.1 Direct Cooling

There are several direct cooling methods. A common way to produce cold molecular beams is through Stark deceleration. Stark deceleration can slow down a molecular beam through rapidly switching electric fields. This has been demonstrated for several species, including YbF [29], H_2CO [5], CO [30], NH_3 [31], OH [32] and NH [33]. Similarly a cold molecular beam can be produced with a multistage Zeeman slower [34]. Recently Chervenkov *et al.* demonstrated a continuous source of cold molecules which exploited a decelerating force from a centrifuge [35]. Deceleration of different molecules was achieved and in principle any molecule that can be guided by electrodes can be slowed.

Significant progress has been made in cooling molecules directly through laser cooling. The technique of laser cooling was first demonstrated by Wineland *et al.* in 1978 [36] with Mg ions and soon after applied to slow down and cool a beam of neutral atoms [37]. In 1995 Cornell and Wieman used laser and evaporative cooling to create the first Bose-Einstein Condensate (BEC) of neutral rubidium atoms [38]. Recently this technique has been expanded to molecules. However, this is only possible for molecules with favourable Franck-Condon factors as excited molecules can make transitions to many different vibrational states. Therefore even in molecules with favourable Franck-Condon factors several repump transitions need to be addressed. Laser cooling molecules directly has been demonstrated with CaF [39], YO [40] and SrF [41]. With YO and SrF magneto-optical traps have been constructed that are able to cool molecules to milliKelvin temperatures. However, even with several repump lasers the lifetime of these traps is still very short, and it is therefore important to transfer the molecules into a different trap quickly after cooling is complete.

A method that has not yet been demonstrated is to cool molecules by bringing them

in contact with cold atoms. This method is called sympathetic cooling. The principles of it haven been discussed theoretically in many papers, for example the cooling of NH molecules in a magnetic trap using ultracold Mg atoms [42], and using Li atoms for cooling in a magnetic trap [43] and in a microwave trap [44]. A different form of sympathetic cooling produces cold molecules by bringing them into contact with a buffer gas, such as cold helium[45].

There is promise that direct cooling methods will lead to an ultracold molecular ensemble that can be used for quantum simulations. Zeppenfeld *et al.* have demonstrated Sisyphus cooling with CH_3F molecules [46], and evaporative cooling has been demonstrated with OH radicals [47].

1.1.2 Indirect Cooling

Indirect cooling produces molecules by binding together ultracold atoms. As laser cooling has been achieved mainly for alkali and rare-earth atoms, the indirect cooling methods are limited to a small range of possible molecules. The advantage however is that atoms can be cooled to lower temperatures, which will result in colder molecules. Indirect cooling is done through two main methods.

In photoassociation (PA) laser light is used to excite unbound atoms to an electronically excited bound molecular state [48]. These loosely bound molecules can spontaneously decay to the electronic ground state. However as decay to a high vibrational level is more likely, the molecules need to be transferred to the ro-vibrational ground state, which can be achieved through laser excitations [49]. The spontaneous decay can also be manipulated by careful selection of the excited state [50]. The PA rate can be enhanced by exploiting a Feshbach resonance as demonstrated with LiRb [51, 52]. A list of photoassociated molecules is given in [48].

Magneto-association through a Feshbach resonance is the second commonly employed method for creating ultracold molecules. A detailed explanation of how Feshbach molecules are created is given in section 2.3. There is a large selection of homo- and hetero-nuclear bi-alkali molecules that have been associated; Li_2 [53, 54], Na_2 [55], K_2 [56], Rb_2 [57, 58], Cs_2 [59], KRb [60], LiK [61], NaLi [62], NaK [63], RbCs [64, 65], NaRb [14]. However none of these molecules have a ground state spin. Therefore several groups are working towards binding ytterbium with an alkali; LiYb [66, 67] and RbYb [68]. In this experiment we are working towards associating caesium and ytterbium with use of a Feshbach resonance.

Stellmer *et al.* have formed Sr_2 rare-earth molecules through stimulated Raman adiabatic passage (STIRAP) association directly [69]. This was achieved by forming an optical lattice with two Sr atoms on each lattice site so that a direct STIRAP association was possible.

1.2 Thesis Outline

This thesis describes the progress made towards building a dual magneto-optical trap of caesium and ytterbium. As the project started out with a trap for lithium and ytterbium the initial setup is described as well. However the lithium experiment was discontinued and the equipment for ytterbium was moved from Imperial College London to Durham University to join with an existing caesium magneto-optical trap (MOT).

The thesis consists of 5 main chapters. Chapter 2 outlines the basic atomic physics theory required to help understand the rest of the thesis. It outlines the basics of atom-light interactions, as well as the Zeeman effect. It discusses the relevant properties of caesium and ytterbium. Furthermore we outline the origin of Feshbach resonances and how they can be used to form molecules.

Chapter 3 describes both vacuum systems that were used in this project. We begin by describing the vacuum system constructed at Imperial College London and subsequently outline the vacuum system built at Durham University. For both systems we describe the oven, Zeeman slower and MOT chamber, as well as the measurements taken from the atomic beams. Furthermore we discuss the pumping systems and bake-out procedures.

Chapter 4 discusses the lasers and the optics that were used in this project. Two 852 nm lasers are used, one for the cooling and one for the repump laser. They are locked through modulation transfer spectroscopy and frequency modulation spectroscopy respectively. Both locking techniques are explained in detail. We also outline the optics required for the magneto-optical trap and the absorption imaging. For ytterbium the 399 nm laser and 556 nm laser are discussed separately. The 399 nm laser is based on a homebuilt diode system which uses injection seeding. It is locked via a Transfer Cavity Lock (TCL). The 556 nm light is produced from a commercial fiber laser. Several different locking techniques were attempted until it was finally locked using fluorescence spectroscopy from an ytterbium beam. The MOT, Zeeman slowing and absorption imaging optics are outlined.

Chapter 5 explains the theory of the Zeeman slower and presents the experimental results. We have developed a numerical simulation for the Zeeman slower, that follows the basic theory and can predict different behaviours of the slower. The Zeeman slower was optimised for caesium and ytterbium by changing the detuning and power of the laser as well as the magnetic field. For ytterbium the results were compared to the predictions of the numerical simulations.

Chapter 6 outlines the theory of the MOT and presents the results for Cs and Yb. It derives the forces involved and the Doppler cooling limit of the MOT. For both caesium and ytterbium the MOT parameters are optimised. The temperature and atom number is measured using absorption imaging. We also demonstrate that the experiment can trap ytterbium and caesium at the same time.

In the conclusion the main results of this work are outlined. Lastly some future directions of this experiment are discussed.

Chapter 2

Theory

The theory of ultracold atoms and molecules has been discussed and researched in great detail. There are numerous review papers [25, 48, 70, 71, 72, 73] that explore the field thoroughly. This chapter will therefore focus primarily on the theory needed to explain the physics in this work. Section 2.1 outlines the basic atomic physics that is required to understand the experiment and section 2.2 explores the properties of the atomic species used. As we propose to associate the CsYb molecule using a Feshbach resonance, section 2.3 explores the basic theory of Feshbach resonances and how to use them to form molecules.

2.1 Atomic Physics

Some basic physics principles will be applied repeatedly in several chapters of this thesis. It is therefore useful to include a detailed description of the principles. To laser cool both species we use a Zeeman slower and a MOT, both of which use the interaction of the atoms with laser beams (section 2.1.1) and the Zeeman shift induced by a magnetic field (section 2.1.2). A more detailed description of these subjects can be found in most atomic physics textbooks [74]. The specific theory of each piece of equipment is discussed in the relevant chapter.

2.1.1 Atom-Light Interactions

For this discussion we imagine a simplified two level atom with state ground $|g\rangle$ with energy E_g and excited $|e\rangle$ with energy E_e. The energy gap between the two states is

$\hbar\omega_t$ and the spontaneous emission rate is given by Γ. The wavefunction of the atom can therefore be given as:

$$\Psi = c_e e^{-i\omega_e t}|e\rangle + c_g e^{-i\omega_g t}|g\rangle\,, \tag{2.1}$$

where c_e and c_g are normalised coefficients and $\omega_{e,g} = E_{e,g}/\hbar$. We are interested in the interactions of this atom with light. The electric field of such a light wave with angular frequency ω can be expressed as:

$$\mathbf{E} = \frac{1}{2}\mathbf{E}_0\left(e^{i\omega t} + e^{-i\omega t}\right)\,, \tag{2.2}$$

where $\mathbf{E}_0$ is the amplitude of the electric field. The energy of an atom with a dipole $-e\mathbf{r}$ in this electric field is given by the Hamiltonian:

$$H_{\mathrm{I}}(t) = e\mathbf{r}\cdot\mathbf{E}_0\frac{1}{2}\left(e^{i\omega t} + e^{-i\omega t}\right)\,. \tag{2.3}$$

The strength of the interaction between the atom and the light is expressed by the Rabi frequency Ω:

$$\Omega = -\frac{e\langle e|\mathbf{r}\cdot\mathbf{E}_0|g\rangle}{\hbar}\,. \tag{2.4}$$

The dynamics of the two level system are governed by the Schrödinger equation, which after making the rotating-wave approximation reduces to the optical Bloch equations [74]. The steady solution of these equations yields a population in the excited state:

$$|c_e|^2 = \frac{2\Omega^2/\Gamma^2}{2(1 + 2\Omega^2/\Gamma^2 + 4\delta^2/\Gamma^2)}\,, \tag{2.5}$$

where δ is the detuning of the light angular frequency from the atomic angular frequency, $\delta = \omega - \omega_t$. We define the parameter s and the saturation intensity I_s through the relations

$$s = \frac{I}{I_{\mathrm{s}}} = \frac{2|\Omega|^2}{\Gamma^2}\,, \tag{2.6}$$

where I is the intensity of the light field. The saturation intensity provides an estimate for the maximum power that can be absorbed by an area of the atomic cloud. Each absorption event will need to followed by a spontaneous emission event, which occur on a timescale $1/\Gamma$. Assuming that on average 0.5 scattering events occur during this timescale per scattering cross-section σ, the saturation intensity can be written as [74]:

$$I_{\mathrm{s}} = \frac{\Gamma}{2\sigma}\frac{h\,c}{\lambda} = \frac{\pi\Gamma hc}{3\lambda^3}\,, \tag{2.7}$$

where λ is the wavelength of the transition and the cross-section is given by [74]:

$$\sigma = \frac{3\lambda^2}{2\pi}\,. \tag{2.8}$$

The steady state population $|c_e|^2$ multiplied by the decay rate Γ will give the scattering rate of atom-light interactions:

$$R = \Gamma|c_e|^2 = \frac{\Gamma}{2}\frac{s}{(1+s+4\delta^2/\Gamma^2)}\,. \tag{2.9}$$

This scattering rate gives the number of photons scattered from a laser beam incident on an atom. It is used for the theory of the MOT and the Zeeman slower.

2.1.2 Zeeman Shift

Both the MOT and Zeeman slower rely on a magnetic field to manipulate the atom light interactions. The energy levels of an atom in a magnetic field are Zeeman shifted. We assume a magnetic field in the $\hat{z}$ direction, which interacts with the magnetic moment of the atom $\boldsymbol{\mu}$:

$$H_{\mathrm{ZE}} = -\boldsymbol{\mu}\cdot\mathbf{B}\,, \tag{2.10}$$

where $\mathbf{B}$ is the external magnetic field. Using the LS-coupling scheme the magnetic moment can be expressed in terms of the orbital angular momentum $\mathbf{L}$ and spin $\mathbf{S}$ operators:

$$\boldsymbol{\mu} = -\mu_{\mathrm{B}}\mathbf{L} - g_s\mu_{\mathrm{B}}\mathbf{S}\,, \tag{2.11}$$

where μ_{B} is the Bohr magneton and g_s is the spin Lande-g factor. By introducing $\mathbf{J} = \mathbf{L}+\mathbf{S}$, and applying first order perturbation theory the energy shift can be written as [74]:

$$\Delta E_{\mathrm{ZE}} = \frac{\langle JM_J|\mathbf{L}\cdot\mathbf{J}|JM_J\rangle + g_s\langle JM_J|\mathbf{S}\cdot\mathbf{J}|JM_J\rangle}{J(J+1)}\mu_{\mathrm{B}}B\langle JM_J|J_z|JM_J\rangle\,, \tag{2.12}$$

where J_z is the projection of the total angular momentum onto the z-axis. This evaluates to:

$$E_{\mathrm{ZE}} = g_J\mu_{\mathrm{B}}BM_J\,. \tag{2.13}$$

where

$$g_J = \frac{3J(J+1) - L(L+1) + S(S+1)}{2J(J+1)}\,. \tag{2.14}$$

Hence the energy gap between two states will be shifted by:

$$\Delta E = \Delta\mu B \tag{2.15}$$

where $\Delta\mu = ((g_J M_J)_e - (g_J M_J)_g)\mu_\mathrm{B}$ where g and e stand for the ground and excited state of the atom.

2.2 Atomic Species

This thesis describes two experimental setups; one for ytterbium and caesium and one for ytterbium and lithium. For laser cooling a good understanding of the energy levels is required, which therefore makes it important to investigate all species in detail. As however the ytterbium lithium experiment was discontinued and lithium was never used in the experiment, we will not discuss lithium here. A discussion of the relevant lithium properties can be found in [75].

2.2.1 Caesium

Caesium (Cs) has atomic number 55 and belongs to the group of alkali metals, with the only stable isotope being ^{133}Cs. The relevant level structure is shown in Figure 2.1 (a). We use the $6\,^2S_{1/2}\,F = 4 \rightarrow 6\,^2P_{3/2}\,F' = 5$ transition as the cooling cycle. Due to off resonant excitation to the $F' = 4$ level, a repump laser is needed on the $6\,^2S_{1/2}\,F = 3 \rightarrow 6\,^2P_{3/2}\,F' = 4$ transition. The repump laser ensures that any atom that spontaneously decays to the $F = 3$ level is pushed back to the cooling cycle. The wavelength of the transition is 852.3 nm with a natural linewidth of $\Gamma_\mathrm{Cs} = 2\pi \times 5.234\,\mathrm{MHz}$ and a saturation intensity of $I_\mathrm{s} = 1.1049\,\mathrm{mW\,cm^{-2}}$. The Doppler temperature, which will be explained in detail in chapter 6, sets a limit to the minimum temperature that can be achieved by laser cooling without any other cooling effects. It is given by the equation:

$$T_\mathrm{D} = \frac{\hbar\Gamma}{2k_\mathrm{B}}, \tag{2.16}$$

where k_B is the Boltzmann constant. For the relevant transition this temperature is $T_\mathrm{D} = 126\,\mu\mathrm{K}$. However colder temperatures can be reached in a MOT due to sub-

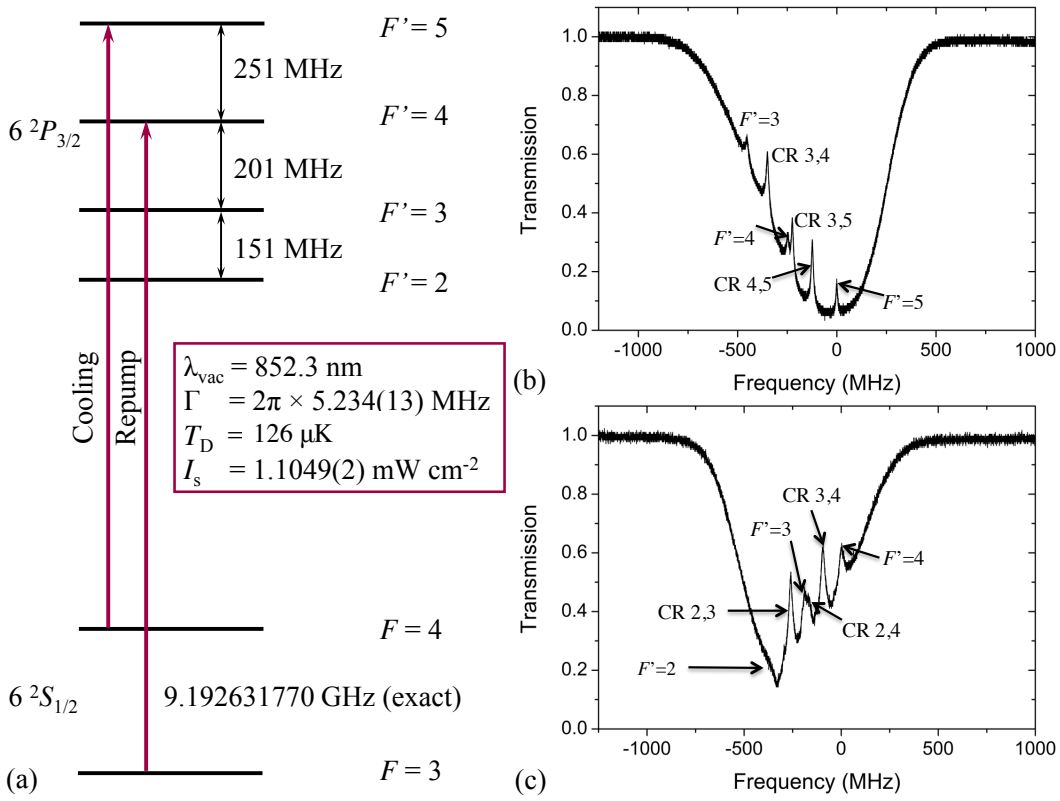

Figure 2.1: (a) The relevant level structure for caesium. Two transitions are addressed by lasers. The $F = 4 \rightarrow F' = 5$ transition is used as the cooling transition. The $F = 3 \rightarrow F' = 4$ transition is also addressed to repump the atoms back to the cooling cycle. The box outlines the wavelength λ_{vac} then natural linewidth Γ, the Doppler temperature T_D and the saturation intensity I_s of the transition. (b) Spectrum of the $F = 4 \rightarrow F'$ transitions. The transitions and crossovers (CR) are labelled.(c) Spectrum of the $F = 3 \rightarrow F'$ transitions. The transitions and crossovers (CR) are labelled. [1]

Isotope	Mass [u]	Abundance [%]	Nuclear Spin	Mag. Moment [μ_n]
168	167.93	0.13	0	
170	169.93	3.05	0	
171	170.94	14.3	1/2	+0.4919
172	171.94	21.9	0	
173	172.94	16.12	5/2	-0.6776
174	173.94	31.8	0	
176	175.94	12.7	0	

Table 2.1: The stable isotopes of Yb and their masses and abundances, nuclear spins and magnetic moments in units of the nuclear magnetic moment μ_n [76].

Doppler cooling. Figures 2.1 (b) and (c) show a spectrum of the hyperfine levels for the transitions originating from $F = 4$ and $F = 3$ respectively.

2.2.2 Ytterbium

Ytterbium (Yb) has atomic number 70 and is a rare-earth metal belonging to the lanthanide series. There are seven isotopes of ytterbium; 5 Bosons and 2 Fermions. All have been successfully trapped in a magneto-optical trap [77, 78]. The isotopes and their properties are outlined in Table 2.1. Figure 2.2 shows the relevant energy levels for laser cooling Yb. The ${}^1S_0 \rightarrow {}^1P_1$ transition is used for slowing the beam in the Zeeman slower. The transition has a wavelength $\lambda_{\text{vac}} = 398.9\,\text{nm}$, which can be obtained from a laser diode. It has a large natural linewidth $\Gamma_{399} = 2\pi \times 29\,\text{MHz}$, which will lead to high scattering rate. This makes it ideal for Zeeman slowing, but also leads to a large Doppler temperature $T_D = 673\,\mu\text{K}$. There is also a 10^{-7} chance that an atom in the ${}^1P_1$ state decays to one of the ${}^3D$ states, instead of the ground state. This would result in losing the atom from the cooling cycle, which severely limits the lifetime of a 399 nm MOT. The MOT is therefore loaded directly on the intercombination ${}^1S_0 \rightarrow {}^3P_1$ transition. This transition has a wavelength of $\lambda_{\text{vac}} = 555.8\,\text{nm}$ and a natural linewidth of $\Gamma_{556} = 2\pi \times 182\,\text{kHz}$. Compared to the ${}^1S_0 \rightarrow {}^1P_1$ transition, this transition is more narrow by a factor of 160. This occurs since the optical field mainly interacts with the angular moment of the dipole. The spin change only arises due to the fine structure of the atom. The Doppler limited temperature is therefore $4.4\,\mu\text{K}$. Figure 2.2 (b) and (c) show the isotope shifts for the 399 nm and 556 nm transition respectively. The spatial lines of the various isotopes are shifted due to their different masses and volumes. A detailed explanation can be found in [74].

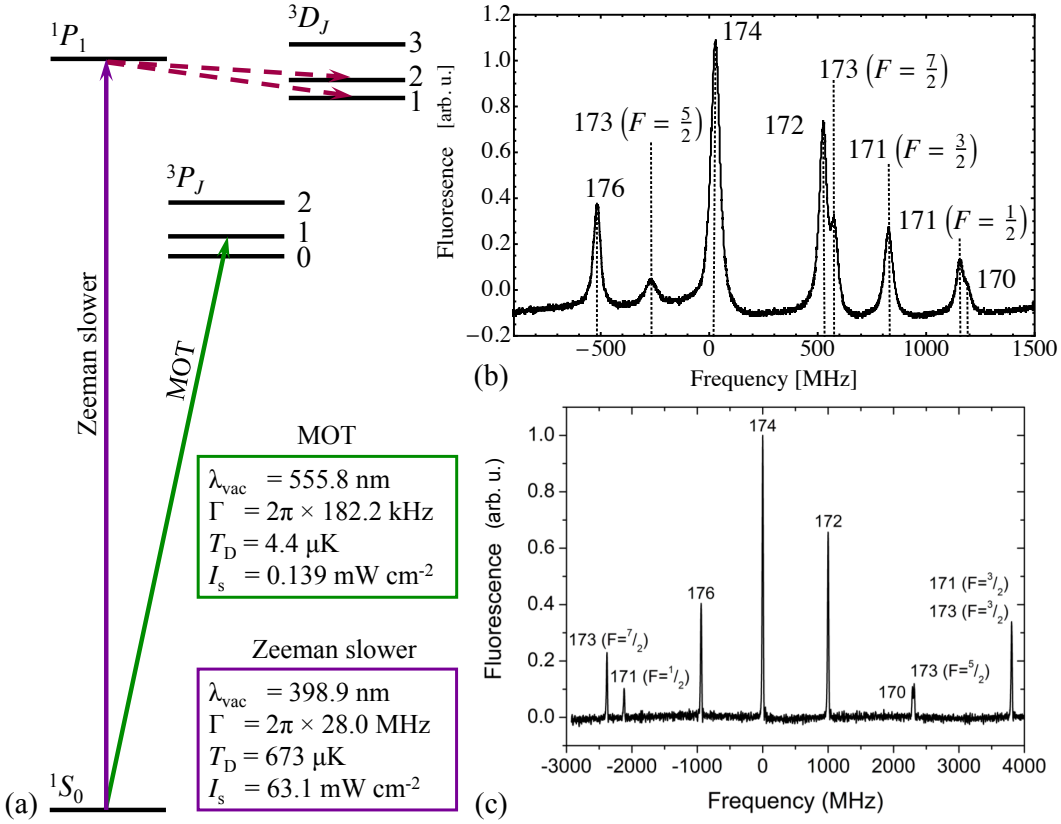

Figure 2.2: (a) The relevant energy levels for laser cooling ytterbium. The $^1S_0 \rightarrow {}^1P_1$ transition is used in the Zeeman slower and the $^1S_0 \rightarrow {}^3P_1$ transition is used for the MOT. The wavelength λ_{vac}, the natural linewidth Γ, the Doppler temperature T_D and the saturation intensity I_s are listed for the two relevant transitions. Decay from the $^1P_1$ level to the ^3D states is possible. (b) Spectrum of the 398.9 nm transition of Yb. The visible isotopes are labelled. (c) Spectrum of the 555.8 nm transition of Yb. The visible isotopes are labelled. [1]

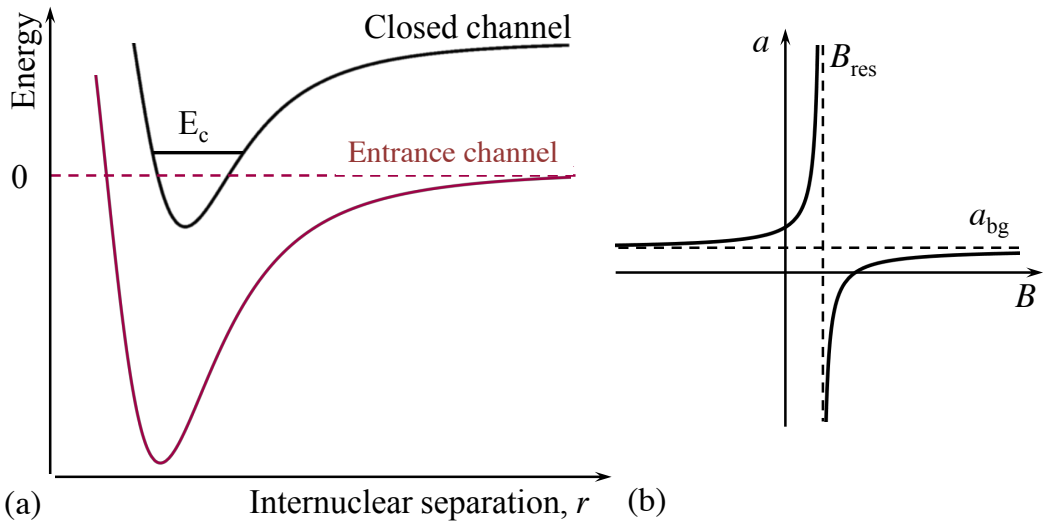

Figure 2.3: (a) Schematic diagram of the molecular energy level varying with internuclear distance. The entrance and closed channel are labelled. (b) Schematic drawing of the scattering around the Feshbach resonance. The scattering length varies between $-\infty$ and ∞ [1].

2.3 Feshbach Resonances

There are several methods to associate cold atoms to molecules (see section 1.1). For this experiment we propose associating the atoms over a Feshbach resonance. Therefore the following section will discuss the basic physics of Feshbach resonances and how they can be used to form molecules.

2.3.1 Origin of Feshbach Resonances

Feshbach resonances were discovered by Herman Feshbach in 1958 [79] and occur when the "the energy of a diatomic vibrational bound state becomes degenerate with the threshold of the dissociation into an atom pair at rest" [80]. Figure 2.3 (a) illustrates the molecular energy levels involved. The molecular potential curve for which the atoms are free is called the entrance channel and the potential binding the atoms at the same energy is the closed channel. A magnetic field can influence the energy level E_c of the closed channel and thereby tune the level into resonance.

The interaction at a resonance is often characterised by the scattering length a.

The scattering length is normally used for low energy 2-body collisions where s-wave scattering dominates. As a slow particle will have a long de-Broglie wavelength, it will not resolve the precise structure of the potential it is scattered off. The scattering length a gives a scale at which the scatterer can feel the influence of the potential. For a scattering channel that is just bound the scattering length will be large and positive. While a channel that is just unbound will have a large and negative scattering length. The scattering rate tends to infinity when a bound state is at the dissociation limit. Due to the coupling of entrance and closed channel (see section 2.3.2) this is the case at a Feshbach resonance and hence the scattering length a is given by [81]:

$$a(B) = a_{\mathrm{bg}} \left(1 - \frac{\Delta}{B - B_{\mathrm{res}}} \right) , \tag{2.17}$$

where a_{bg} is the background scattering length, B_{res} is the magnetic field resonance and Δ is the resonance width. Figure 2.3 (b) shows how the scattering length varies between $-\infty$ and $+\infty$ around a Feshbach resonance, which allows for widely tuneable atomic interactions. For positive values of a there exists a dressed molecular state with an energy level that depends on the reduced mass of the atomic pair μ:

$$E_{\mathrm{res}} = \frac{\hbar^2}{2\,\mu\,a^2} . \tag{2.18}$$

This energy can be tuned so that free atoms are adiabatically transferred to a molecular bound state, as outlined in the next section.

2.3.2 Molecule Association via a Feshbach Resonance

In 1999 Timmermans *et al.* [82] and van Abeelen and Verhaar [83] discussed the possibility of creating molecules through a Feshbach resonance tuned by an external magnetic field. If the entrance and closed channel are strongly coupled an avoided crossing will occur at the Feshbach resonance. By ramping an external magnetic field over the Feshbach resonances the atoms will adiabatically transfer from the entrance to the closed channel. Mies calculated that this transfer occurs when the magnetic field is ramped linearly and sufficiently slowly [84]. The resulting molecules will be in an excited state and are commonly called Feshbach molecules.

As discussed in section 1.1 a number of bi-alkali molecules have been created using this method [53, 54, 56, 57, 58, 59, 60, 85]. The reason many bi-alkali molecules were

created is the strong coupling between the entrance and closed channels. As each alkali atom has a spin of $s = 1/2$ due to its single valence electron, a pair of alkali atoms can form either a singlet ($S = 0$) or triplet ($S = 1$) molecular bound state. These states will be strongly coupled due to the spin-orbit coupling, which will lead to many Feshbach resonances that can be used.

For alkaline rare-earth mixtures however this coupling does not exist. The two valence electrons of the rare-earth atom will lead to a $s = 0$ spin in the ground state. Hence pairing a rare-earth with an alkali metal will lead to doublet states ($S = 1/2$). Crossing of energy levels will still occur, but they are not coupled through spin-orbit interaction. However it has been predicted [86] that the hyperfine coupling of such an atom pair will depend on the internuclear distance. This will effectively create a coupling if the alkali is in proximity of a rare-earth atom. This coupling will create Feshbach resonances for Yb and Cs.

The lifetime of Feshbach molecules will be severely limited by inelastic collisions. To improve this the molecule can be transferred to its rotational and vibrational ground state through stimulated Raman adiabatic passage (STIRAP). The process transfers molecules to a lower energy state through a sequence of laser pulses [87]. This has been achieved for some Feshbach molecules [60, 88]. This ground state molecule is what this experiment aims for, as it can be used in a number of interesting setups.

2.3.3 The CsYb Molecule

The caesium-ytterbium molecule is of interest due to a number of favourable aspects. The hyperfine coupling in caesium is predicted to be large when another atom is brought close [86]. This should lead to sufficiently wide resonances that will make magnetic association easier. Ytterbium has seven stable isotopes that can be used. As different isotopes have different masses, the reduced mass μ can be manipulated. This is important as it is hard to predict the external magnetic field needed to find a Feshbach resonance. For such predictions it is important to have an accurate measure of the background scattering length. With seven different Yb isotopes the likelihood of finding a Feshbach resonance that is accessible for our experiment increases.

As discussed in the Introduction the ground-state molecule will have a magnetic dipole moment due to the unpaired valence electron. Additionally to that CsYb is also expected to have an electric dipole moment. In diatomic molecules such a dipole moment exists as the centres of the positive and negative charges do not overlap.

However a preferred orientation of the dipole will need to be induced by an external electric field. The electric dipole moment is predicted to be 0.24 Debye at a critical electric field $3.5\,\mathrm{kV\,cm^{-1}}$ [89]. The molecule can therefore be controlled by magnetic and electric field, which is important for spin dependent dipole-dipole interactions as proposed in different experiments. The CsYb molecules is also unstable as 2 CsYb molecules will decay to $2\,\mathrm{CsYb} \rightarrow \mathrm{Cs_2} + \mathrm{Yb_2}$. Therefore it is necessary to associate the molecule on a lattice.

Chapter 3

Vacuum System

Dual trapping and cooling experiments require large and complex vacuum chambers. During this project two vacuum chambers were built one for lithium and ytterbium at Imperial College London (section 3.1) and a second for ytterbium and caesium at Durham University (section 3.2). The Imperial vacuum system was designed and constructed by Michael Petersen and myself. While I contributed to the design of the Durham vacuum system, it was mainly designed and constructed by Steve Hopkins and Kirsteen Butler. Both systems are discussed in detail here as they are important for the remainder of the work. Even though there are many similarities between these vacuum systems I will describe each in turn to avoid confusion.

3.1 Imperial Vacuum System

Figure 3.1 shows an overview of the vacuum chamber constructed at Imperial College London. It consists of several parts; an oven (section 3.1.1), a transverse cooling stage, a Zeeman slower (section 3.1.2), a MOT chamber (section 3.1.2) and two pumping stations (section 3.1.3). The oven emits ytterbium and lithium atoms through a narrow aperture. This atomic beam passes through the first pumping station, which is separated from the remaining vacuum chamber by a gate valve and a differential pumping tube of inner diameter 4 mm and length 70 mm. From there the atomic beam is passed through two cubes that can provide the optical access for transverse cooling. This however was never implemented and the cubes only served for spectroscopy of the atomic beam. The atoms are decelerated by the Zeeman slower and finally trapped inside the MOT chamber. Behind the MOT chamber there is a second pumping station

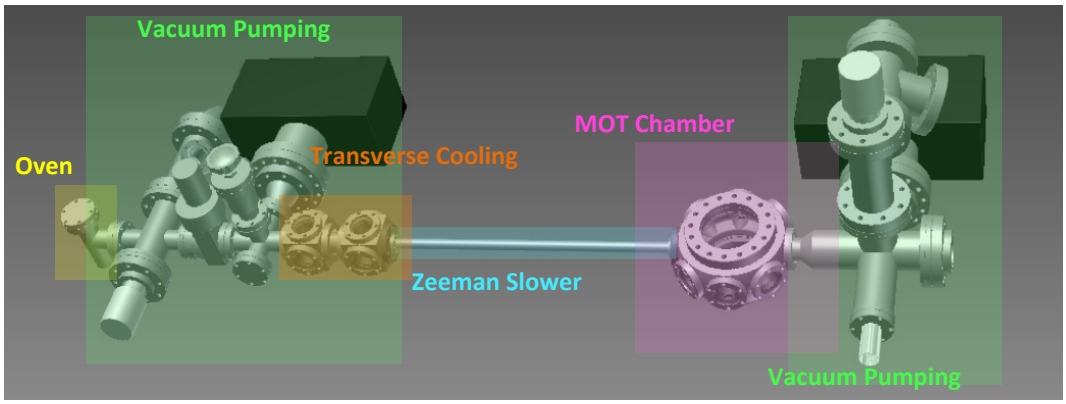

Figure 3.1: Overview of the Imperial Vacuum System. The oven is shaded yellow. All vacuum pumping is shaded green. The Zeeman slower is shaded blue. And the MOT chamber is shaded in pink.

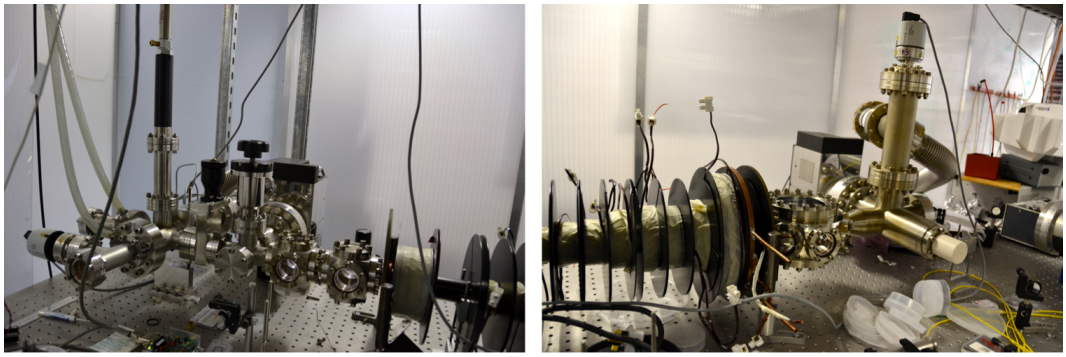

Figure 3.2: Two pictures of the Imperial Vacuum chamber. The first picture shows the oven, the first pumping station, the transverse cooling section and the beginning of the Zeeman slower. The second picture shows the end of the Zeeman slower, the MOT chamber, and the second pumping station.

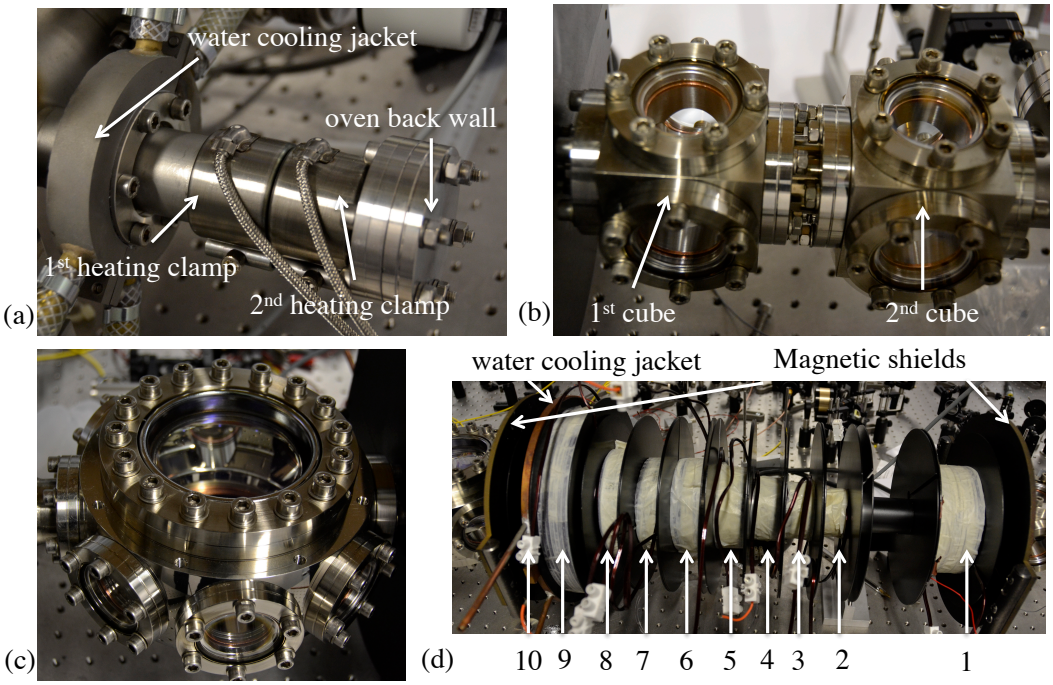

Figure 3.3: Pictures of the different parts of the Imperial Vacuum system. (a) The oven including the heating clamps. The aperture is located under the 1st heating clamp. (b) The transverse cooling stage. (c) The MOT chamber. Atoms enter from the right. (d) The Zeeman slower. Atoms are travelling from right to left. The magnetic coils are numbered according to the description in section 5.2

that creates the ultrahigh vacuum (UHV) inside the MOT chamber. Pictures of the system are shown in Figures 3.2 and 3.3.

Section 3.1.3 describes the bake-out process of the system. Finally section 3.1.4 explores some problems of the chamber and the reason no MOT was observed.

3.1.1 Oven and Spectroscopy

Figure 3.3 (a) shows a picture of the oven connected to the vacuum chamber. While it was designed to operate with lithium and ytterbium at the same temperature, the oven was never tested for lithium. It consists simply of a blocked off stainless steel tube. The side facing the Zeeman slower has a small aperture in the centre with 1 mm diameter. Two heater clamps are attached around the tube to provide the heating. To prevent blocking the aperture with Yb, it needs to remain the warmest part throughout

the heating process. The first heating clamp is therefore positioned directly over the aperture. The second clamp is positioned next to it. We monitor the temperature of the oven underneath the first heater clamp and the back wall of the oven. We can raise the temperature of the oven up to 600 °C, which is more than sufficient to create an ytterbium beam. The entire oven is wrapped in layers of "fibrefrax" insulation so that it can reach the required temperature. As we want the rest of the vacuum chamber to remain at lower temperatures, a water cooling jacket was attached to the flange of the oven (see Figure 3.3 (a)).

To investigate the performance of the oven we are interested in the flux. The expected flux after the differential pumping tube from can be calculated. It is given by [90]:

$$Q_{\text{theory}} = \int_0^{2\pi} d\phi \int_0^{\theta_t} \frac{n_{\text{o}} v_{\text{g}} A}{4\pi} \sin\theta \ \cos\theta \ d\theta \,, \tag{3.1}$$

where n_{o} is the number density of atoms inside the oven, v_{g} is the most probable velocity of the atoms, A is the area of the oven aperture and θ and ϕ span the solid angle through which the beam can be emitted. The angle θ_t is therefore given by the maximum angle an atom can have with respect to the vacuum axis so it still pass through the differential pumping tube. The number density inside the oven is given by:

$$n_{\text{o}} = \frac{P}{k_{\text{B}} T} \,, \tag{3.2}$$

where P is the pressure inside the oven, k_{B} is the Boltzmann constant and T is the temperature inside the oven. The oven pressure for ytterbium in Pascal is given by [91]:

$$\log P = 5.006 + 9.111 - \frac{8111}{T} - 1.0849 \log T \,. \tag{3.3}$$

The most probable velocity inside the oven is given by [92]:

$$v_{\text{g}} = \sqrt{\frac{2 k_{\text{B}} T}{M}} \,, \tag{3.4}$$

where M is the mass of an ytterbium atom. The red line in Figure 3.4 shows the calculated atomic flux after the differential pumping tube.

To test these calculations, the absorption of a laser beam on resonance with the ${}^1S_0 \rightarrow {}^1P_1$ transition is measured. The laser beam is passed through the first transverse cooling cube at right angles with the atomic beam. The flux through a cross section

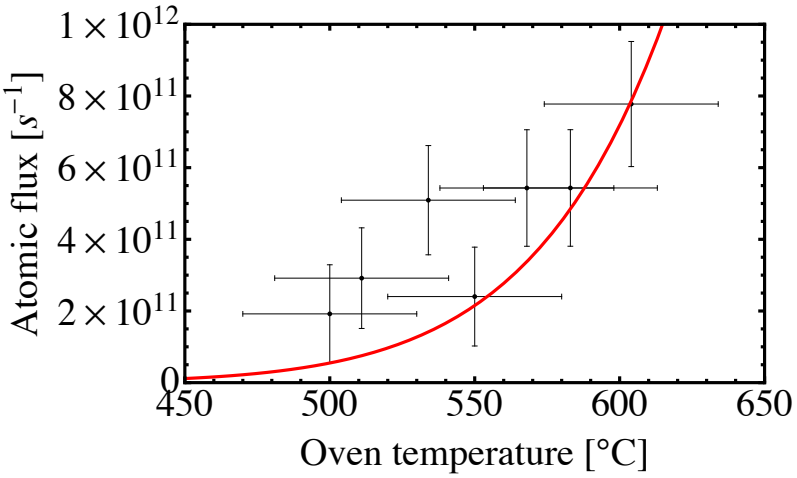

Figure 3.4: Graph showing the atomic flux with varying oven temperature after the differential pumping tube. Red curve is calculated from the theoretical equation (3.1). The measurements are deduced from absorption with a 399 nm beam. The uncertainty in the measurements is large, because the exact temperature of the Yb cannot be measured. Furthermore only a few percent were absorbed from the laser beam.

of the beam is given by:

$$Q_{\mathrm{Abs}} = \pi \left(\frac{d_{\mathrm{B}}}{2}\right)^2 n_{\mathrm{B}} v_{\mathrm{B}} \,, \tag{3.5}$$

where d_{B} is the diameter of the beam, n_{B} is the number density of the beam and v_{B} is the most probable velocity inside the beam. The beam diameter d_{B} can be determined by considering the constraints of the differential pumping tube. It is therefore approximated as:

$$d_{\mathrm{B}} = \frac{d_{\mathrm{diff}}}{z_{\mathrm{diff}}} z_{\mathrm{meas}} \,, \tag{3.6}$$

where d_{diff} is the diameter of the differential pumping tube, z_{diff} is the distance between the oven nozzle and the end of the differential pumping tube and z_{meas} is the distance between the point the beam is measured at and the oven nozzle. v_{B} is given by [92]:

$$v_{\mathrm{B}} = \sqrt{\frac{3k_{\mathrm{B}}T}{M}} \,. \tag{3.7}$$

The number density can be calculated from the fractional absorption α and the scat-

tering cross-section of the atoms σ [90]:

$$n_{\mathrm{B}} = \frac{-\ln(1-\alpha)}{\sigma\, d_{\mathrm{B}}}\,. \tag{3.8}$$

If the Doppler broadening is small compared to the natural linewidth, σ just depends on the laser wavelength λ and is given as [93]:

$$\sigma = \frac{3\lambda^2}{2\pi}\,. \tag{3.9}$$

The Doppler broadening is given by $v\, d_{\mathrm{diff}}/(\lambda\, z_{\mathrm{diff}})$, which is 15 MHz. This is smaller then the natural linewidth $\Gamma_{399}/(2\pi) = 28\,\mathrm{MHz}$ and hence the calculations should be approximately correct. Figure 3.4 shows the flux we measure for different oven temperatures T. The theoretical curve shows reasonable agreement with the measured points. There are several errors that need to be considered. The measurements were taken while the oven was cooling down. The temperature was measured directly under the heater clamp, but the ytterbium inside is not necessarily at the same temperature. The error bars were obtained by repeating the measurements three times. The results can be significantly improved by setting up a differential photodiode. The temperature errors were estimated from measured temperature gradient across the oven. The above calculations also assume a uniform laser beam perfectly on resonance with the transition. This is hard to realise in practice. The experiment confirms that we get a strong flux of atoms through the differential pumping tube, which is vital for the Zeeman slower and MOT.

3.1.2 Zeeman Slower and MOT Chamber

The Zeeman slower is there to slow down the atoms from the oven, so they can be trapped in the MOT. It consists of a tube and several coils and is described in detail in chapter 5. The tube is 530 mm long and has a 16 mm inner diameter. A heater tape is wrapped around the tube, which is needed for the bake-out process (see section 3.1.3). We placed round spacers with 38 mm outer diameter over the heater tape so the Zeeman coils are not directly heated and can be moved over the tube. The Zeeman slower is attached with DN16 flanges. As they are more fragile then the DN40 flanges used for most of the system, the Zeeman slower was attached last to reduce the strain on the connections. The coils for the Zeeman slower were wound over separate formers

and slid in the right position before the entire assembled slower was attached.

The MOT chamber is the main part of the experiment in which the atoms are trapped and investigated. The MOT is discussed in detail in chapter 6. The vacuum part has an octagonal shape with 8 DN40 ports at the side and DN100 ports at the top and bottom. Windows are attached to six of the side ports as well as to the top and bottom. The windows are anti-reflection coated for 556 nm for the ytterbium MOT and 671 nm for the lithium MOT. Four of the side viewports and the top and bottom viewport are used for optical access for the MOT beams. The two remaining windows can be used to investigate the MOT or for implementing a dipole trap. The other two ports on the side of the chamber are used to connect the Zeeman slower and the second pumping station.

3.1.3 Vacuum Pumping and Bake-Out Process

The vacuum chamber is separated into two parts by a differential pumping tube and gate valve. We will refer to them as the oven chamber and main chamber throughout. The oven chamber is pumped by a turbo-pump (TMP151, *Oerlikon Leybold*). It is backed by a scroll pump (IDP3A01, *Varian*) with $0.83\,\mathrm{l\,s^{-1}}$ pumping speed. In normal operation these pumps continuously pump the oven section, which is separated from the remaining vacuum chamber by the differential pumping tube. Furthermore a gate valve can separate the two chambers completely. An ion pump (919-1410, *VacIon Plus 75*) is used after the the differential pumping tube to pump the transverse cooling stage and the Zeeman slower. It has a pumping speed of $75\,\mathrm{l\,s^{-1}}$ and is mainly useful for H_2 and H_2O. A tube connected to a second valve connects the two parts of the chamber and can be opened for initial pumping purposes. A pressure gauge (PKR261, *Pfeiffer*) monitors the pressure of the oven chamber. The pumping for the main chamber is located after the MOT chamber (see Figure 3.1). It is permanently pumped by an ion pump (919-1410, *Vaclon Plus 75*) and a getter pump. The pressure is monitored by a cold cathode pressure gauge (IKR 270, *Pfeiffer*).

To achieve good vacuum pressure all vacuum parts were cleaned thoroughly. Each part was bathed in an ultrasound bath filled with water and detergent (Decon 90). Subsequently they were rinsed with distilled water and wiped with acetone and isopropanol.

The entire chamber was covered with heater tapes and aluminium foil in order to bake-out the vacuum chamber. This process is necessary to remove water and

other unwanted molecules from the walls of the chamber. While a high bake-out temperature is desirable the viewports can break at temperatures higher than 200 °C. The entire system was baked out at the same time over the course of 10 days. The Zeeman slower was built with a permanent heater tape underneath the coils, as it was easier to attach the coils before assembling the vacuum chamber. After the bake-out process was completed, we activated the getter pump. The final vacuum pressures were 5×10^{-9} mbar in the oven chamber and $< 5 \times 10^{-11}$ mbar in the main chamber. The exact pressure of the main chamber could not be determined as the cold cathode pressure gauge cannot measure smaller pressures.

3.1.4 Fundamental Problems

When trying to trap atoms inside the MOT we discovered that the atomic beam was not travelling through the centre of the MOT chamber. By shining a probe of blue light through the MOT chamber the beam was observed about 2 cm away from the centre of the MOT chamber. This occurred due to a misalignment of the differential pumping tube. While this is not a fundamental problem, it is important that the slow atoms emerging from the Zeeman slower travel through the MOT region so they can be trapped.

While this problem is mendable, we also need to ensure that the MOT is sitting at a magnetic field zero. This is especially hard to accomplish in this system as no direct measurement of the magnetic field in the closed vacuum system could be taken. For the formation of a trap it is critical that the magnetic field zero is within the MOT beams. As this was also the main challenge when looking for a Yb MOT in the Durham vacuum system (see section 6.4.1), we believe this was the main reason no MOT was found at Imperial. As the plan to create a lithium-ytterbium trap was already abandoned there was little to be gained from continuing with the vacuum system.

3.2 Durham Vacuum System

The Durham vacuum system was designed to slow and trap caesium and ytterbium simultaneously. Figure 3.5 shows a picture of the assembled vacuum chamber and two schematic drawings.. It consists of a dual species oven (section 3.2.1), a dual species Zeeman slower, the Science Chamber for trapping the atoms (section 3.2.2) and a pumping station (see section 3.2.3).

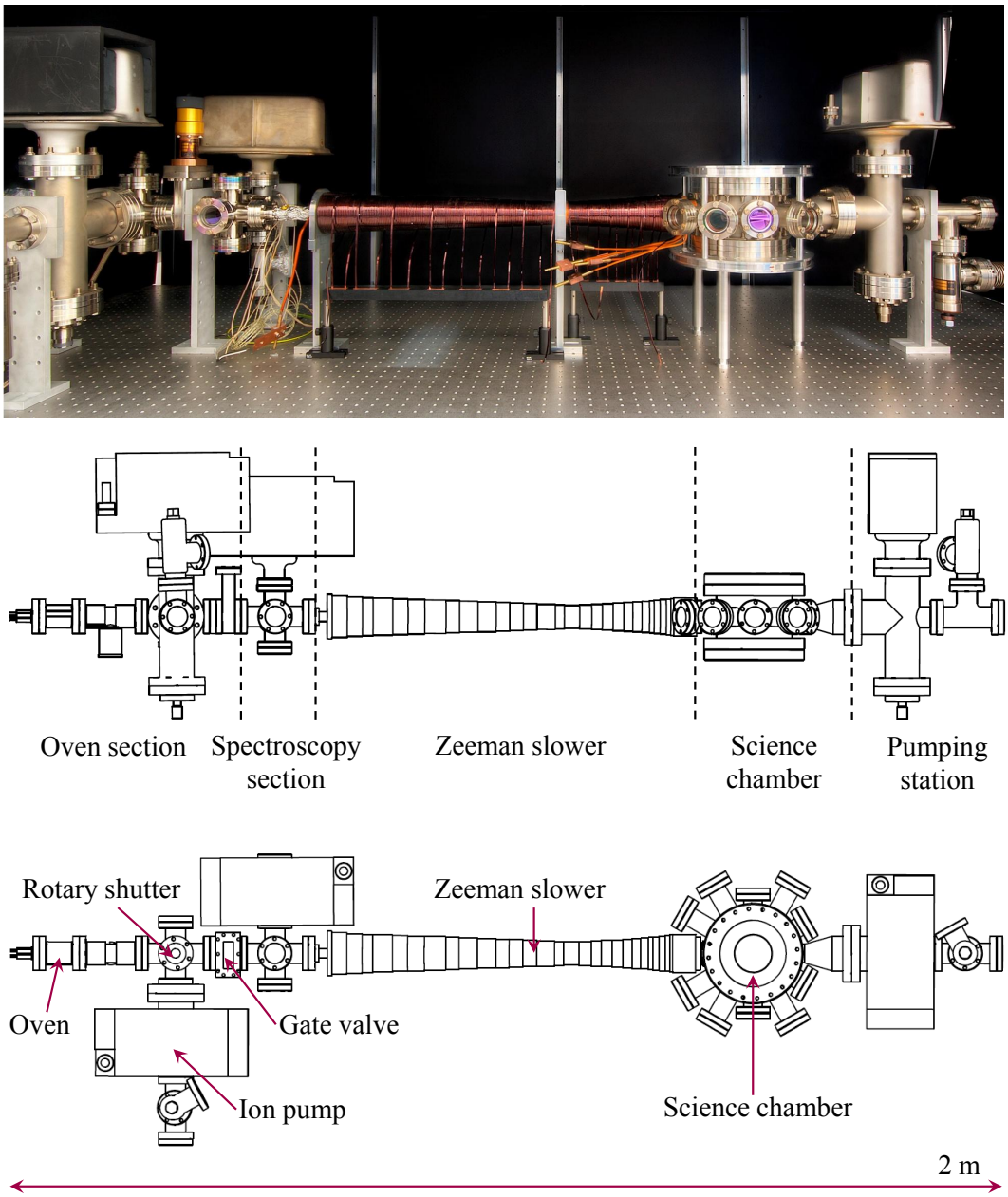

Figure 3.5: Picture and schematic drawings of the Durham vacuum system. The top picture is a picture of the assembled vacuum chamber. The middle figure shows a schematic of the full vacuum system from the side. The different sections are labelled. The bottom schematic shows the vacuum chamber from the top [1].

3.2.1 Oven

In contrast to lithium and ytterbium, caesium and ytterbium have very different vapour pressures. Therefore we need an oven that is separated into two parts that can be kept at different temperatures. However we do require the two atomic beams to travel through the same Zeeman slower. Therefore the caesium and ytterbium beams need to be combined. Figure 3.6 (a) shows a schematic drawing of the oven. The caesium was emitted from dispensers (AS-3-Cs-250-S, *Alvatec*) mounted at the back of the oven. The large spray of caesium from the dispensers was meant to coat the vacuum walls, which could be reheated to 100 °C through a nozzle heater. The oven however was depleted of caesium quickly and was therefore replaced by a caesium ampule. Furthermore a valve was included to close off the caesium oven when required. A water cooling clamp over the flange reduces the heat transfer from the ytterbium part of the oven which is significantly hotter. The Yb oven is loaded with three ytterbium ingots (261300-5G, *Sigma-Aldrich*) and heated to around 400 °C by nozzle heaters (MB1J2AN1-X56, *Watlow*). We initially chose a nickel gasket to seal the vacuum in the Yb oven to avoid the ytterbium corroding an ordinary copper gasket [94]. However, similar to the group in Washington [95], we found the nickel also reacted with ytterbium, so it was eventually replaced with a silver-plated copper gasket.

Both the ytterbium and caesium are guided from their ovens through hemispherical channels towards the capillaries. The oven was wire eroded by the mechanical workshop at Imperial College London and the two channels were separated by 0.4 mm (see Figure 3.6 (c)). The two atomic beams exit the oven through 55 capillaries (*Coopers Needleworks* 20 mm long, 0.58 mm inner diameter and 0.89 mm outer diameter). The capillaries are mounted in a triangular shape in front of the two hemispherical channels. A final nozzle heater (MB1J1N4-X36, *Watlow*) is attached above the capillaries to raise their temperature to around 500 °C. This is done so that the capillaries are not clogged with ytterbium. When the oven is turned on and off care is taken to ensure that the capillaries are always the hottest part of the oven.

There are several thermistors attached to the outside of the oven chamber to monitor the heating process. This is done so the caesium and ytterbium ovens do not get too hot. During normal operation we measure the caesium oven at 83 °C, the middle section close to the water cooling flange at 238 °C, the Yb oven at 434 °C and the capillaries at 478 °C. All the values are outlined in Table 3.1. The design temperatures and operating temperatures vary by large amounts as the cooling clamps did not work as efficiently

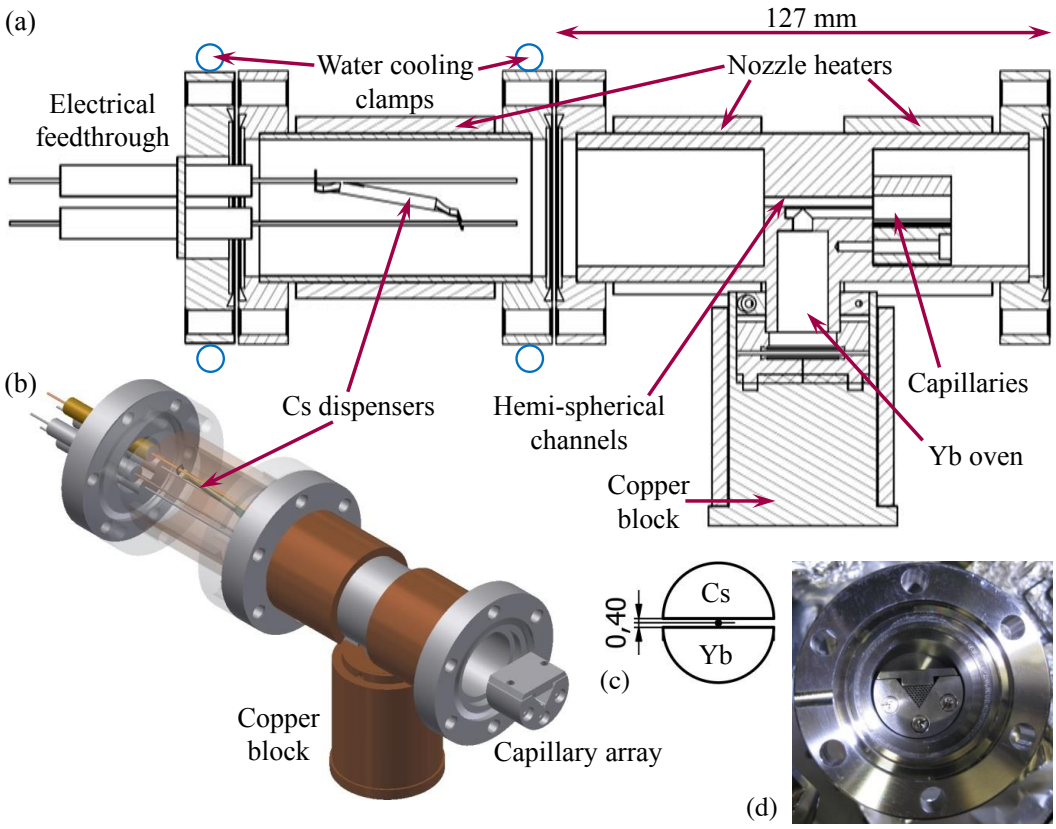

Figure 3.6: Diagrams and pictures of the dual species ytterbium and caesium oven. (a) Schematic drawing of the dual species oven. The Cs is emitted from the Cs dispensers at the back (left). Later the caesium was replaced by an ampule and a valve was included to close of the Cs oven. The Yb oven is sitting below the main vacuum axis. The two atomic species are combined through hemispherical channels through an array of capillary tubes. (b) The Yb oven and the capillaries are heated by four nozzle heaters. The heat transfer between the different sections of the oven is controlled with water cooling clamps shown in (a). The capillary array is mounted to the front of the hemispherical channels. (c) The two hemispherical channels for the ytterbium and caesium beam. The small separation of 0.4 mm allows them to overlap when exiting the capillaries. (d) The capillary array forming the opening to the oven. It contains 55 tubes. [1].

Location	Design Temperature [°C]	Operating Temperature [°C]
Cs Oven	100	83
Middle Section	390	238
Yb oven	400	434
Capillaries	570	478

Table 3.1: The design and operating temperatures of different parts of the oven.

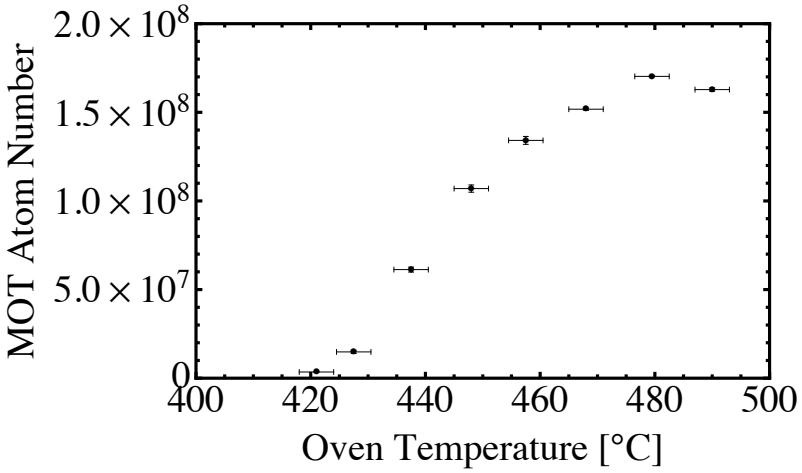

Figure 3.7: Ytterbium atom numbers in the MOT after loading for three seconds, versus the temperature of the oven. Horizontal error bars are estimated from the temperature gradient over the oven. The MOT disappears at temperatures below 420 °C. The graph also shows that the captured MOT atom number plateaus at a temperature around 480 °C.

as predicted. The final temperatures are chosen so that the Yb oven is not heated too much as this would lead to a rapid depletion of ytterbium. This however meant that the remaining oven sections could not be raised to the design temperatures. These temperatures however are sufficient for a good flux of both Yb and Cs.

As interference between atoms from different tubes can be neglected, the forward intensity of the beam should scale linearly with the number of capillaries. However the theoretical considerations in section 3.1.1 do not apply for this oven as it has multiple capillaries instead of one aperture.

Figure 3.7 investigates the MOT load with varying oven temperatures for ytterbium. A MOT is observable at temperatures above 420 °C. Until 480 °C the trapped atom number rises continuously. After that however the atom number plateaus with rising temperature. This seems counter intuitive as the exponentially rising vapour pressure

(a) 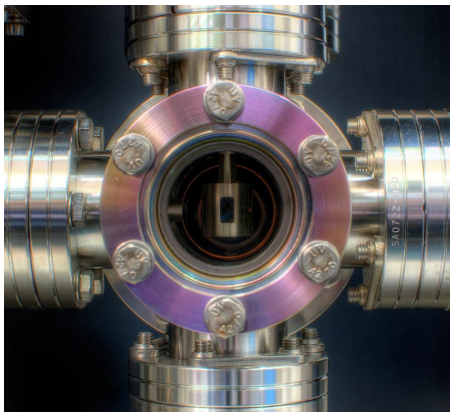 (b) 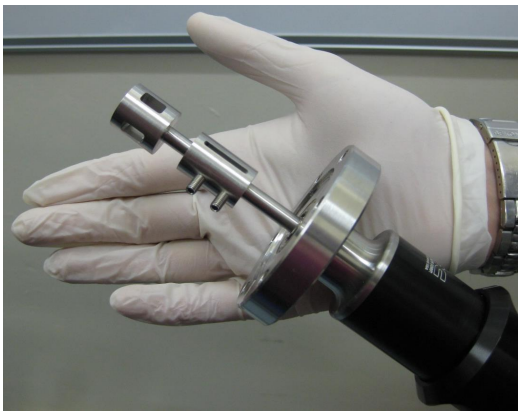

Figure 3.8: The rotary shutter outside the oven. (a) Picture of the mounter rotary shutter in the open position. The atomic beam is travelling from right to left. (b) Picture of the unmounted rotary shutters. Two of the apertures can be seen at 90° to each other [1].

should lead to an exponential increase in the atomic flux. Even though the fraction captured by the Zeeman slower is getting smaller (see chapter 5), this effect should not stop the increase in atom number. The most likely cause is the atomic beam switching from molecular to hydrodynamic flow. Molecular flow occurs when the mean free path Λ of an atom is longer than either the the length or the diameter of the relevant aperture [90]. With higher pressure the mean free path of the atoms will decrease and the flow is no longer molecular, which leads to a loss in the collimation of the beam. For ytterbium the flow changes from molecular to hydrodynamic between $396 \leq T \leq 594\,^{\circ}\mathrm{C}$ [1]. The Beam Machine (see section 4.2.3.1), which uses a very similar oven design, showed a large spread of ytterbium in the chamber behind the capillaries. Therefore we believe that the atomic beam switches from molecular to hydrodynamic flow, which leads to a smaller MOT load.

The oven section also includes a motorised rotary shutter (BRM-275-03, *MDC Vacuum*) to block the atomic beams when required. Figure 3.8 displays two pictures of the shutter. Two 5 mm notches are cut through it at 90° to each other. This setup allows a spectroscopy beam to interact with the atomic beam through the shutter. Furthermore for ytterbium the blue Zeeman beam can be observed and aligned using the fluorescence of the beam.

The oven section is separated from the rest of the vacuum chamber by a gate valve (E-GV-1500M-11, *MDC Vacuum*) and a differential pumping tube (5 mm inner

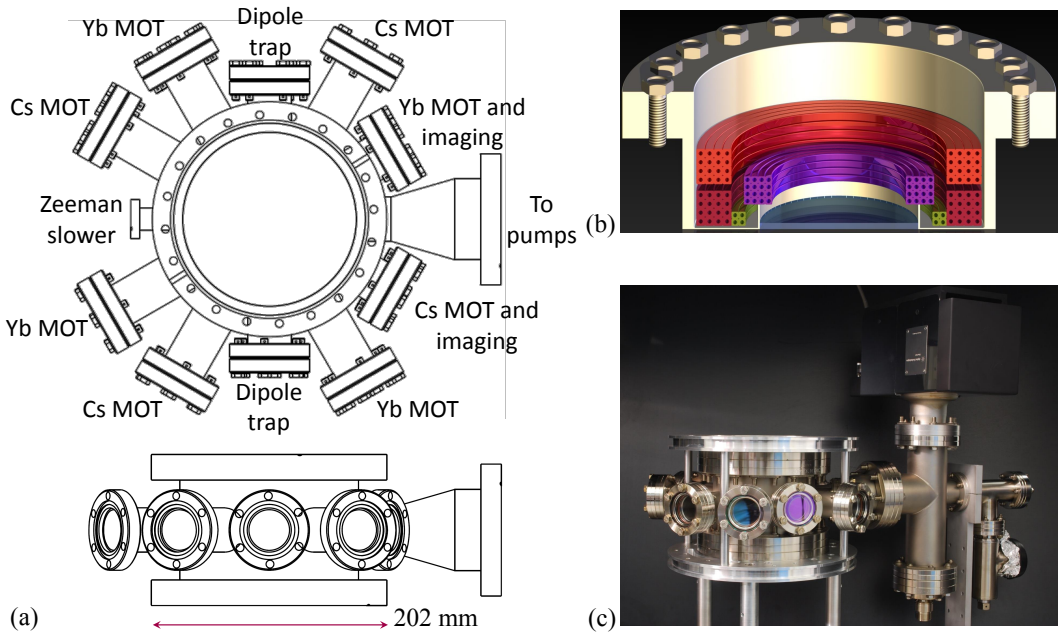

Figure 3.9: The Science chamber. (a) Drawing of the top and side view of the Science Chamber. The viewports are labelled with their designed purposes. (b) The re-entrant viewports mounted to the top and bottom of the Science chamber. There is space for multiple sets of coils. (c) Photograph of the Science chamber mounted to the Pumping Station [1].

diameter, 60 mm long). This requires the oven section to have its own vacuum pumping. It is pumped by a $55\,\mathrm{l\,s^{-1}}$ ion pump and a Non-Evaporable Getter (NEG) pump.

3.2.2 Zeeman slower & Science Chamber

The Zeeman slower is made of a DN16 pipe with 16 mm inner diameter and 770 mm length (075-X, *MDC Vacuum*). Similarly to the Imperial Vacuum system the magnetic coils for the Zeeman slower were wound separately and placed over the tube before it was connected to the vacuum chamber. As the DN16 is the smallest connection of the Vacuum chamber it was again connected last, so stress on the connections would be kept to a minimum. In addition bellows were used at the end of the slower to relieve the stress. As the Zeeman slowing tube is very long it is pumped from both sides (see section 3.2.3).

The main experimental region of the vacuum chamber is the science chamber, pic-

tured in Figure 3.9 (a). The vacuum part was custom built to meet the various requirements on optical access and other connections. It has a DN16 connection for the Zeeman slower, which is kept as short as possible to bring the end of the Zeeman slower close to the centre of the chamber. A DN40 flange connects the Science chamber to the pumping station (see Figure 3.9 (c)). The remaining ports are mounted with viewports. Eight viewports are used for the Cs and Yb MOT and are anti-reflection coated between 730-1064 nm and 370-580 nm respectively. Two viewports are reserved for the dipole trap and anti-reflection coated at 532 nm, 852 nm and 1064 nm. The top and bottom of the Science Chamber are fitted with re-entrant viewports custom made by the UK Atomic Energy Authority (UKAEA). Figure 3.9 (b) shows the design, which provides the space to mount several coils close to the experimental region. They are anti-reflection coated at 399 nm, 556 nm and 852 nm. The re-entrant viewports allow for a greater control of the magnetic field inside the science chamber which will be useful when investigating Feshbach resonances. A viewport at the end of the vacuum system allows the optical access required for the Zeeman slowing beam.

3.2.3 Vacuum Pumping

Like the Imperial College vacuum system, this system is also separated into two parts by a differential pumping tube. Under continuous operation is maintained by two Non-Evaporable (NEG) pumps (Capacitorr C400-2 DSK, *SAES Getters*), two $55\,\mathrm{l\,s^{-1}}$ ion pumps (VacIon 55, *Agilent*) and one $40\,\mathrm{l\,s^{-1}}$ ion pump (VacIon 40, *Agilent*). The oven section is pumped by one NEG and one $55\,\mathrm{l\,s^{-1}}$ ion pump. The spectroscopy section is pumped by the $40\,\mathrm{l\,s^{-1}}$ and the Science Chamber is pumped by a $55\,\mathrm{l\,s^{-1}}$ and a NEG pump. These pumps keep the Science Chamber at a pressure of around 5×10^{-9} mbar, the spectroscopy section at around 10×10^{-9} mbar and the oven at around 10×10^{-8} mbar. All vacuum measurements were deduced from the ion pump currents, as no pressure gauges were included.

For initial pumping extra valves can be used to connect additional pumps. To reach the final pressures the vacuum chamber was baked-out in several stages. Each part was baked separately before assembling. Finally after the vacuum chamber was assembled the entire system was baked-out with heater tapes and aluminium foil. Turbo pumps were connected to both sections to assist the pump-out process. The final bake out was conducted at 140 °C for 4 days and an additional 19 days at 110 °C.

Chapter 4

Laser Systems

As in many cold atom experiments this experiment relies on laser cooling for the initial cooling stage. For this it is necessary to develop several stable laser systems that can address the relevant cooling cycle for each atomic species. When the cooling cycle is not fully closed, a re-pump laser is required to optically pump the atoms back into the cooling cycle.

The Caesium laser system was constructed by Kirsteen Butler and Stefan Kemp at Durham University. As it was used to obtain the data in this thesis, I include a full description of the system and its frequency locks. All the Ytterbium laser systems were designed and constructed by myself.

We have outlined the relevant atomic transitions for this experiment in section 2.2. For laser cooling we will need laser light at all the relevant frequencies and detunings. This chapter describes the design of all the laser and optical systems used in this experiment.

4.1 Laser System for Caesium

For caesium we will have to address two hyperfine components of 6s $^2S_{1/2}$ - 6p $^2P_{3/2}$ atomic transition. The $F = 4 \rightarrow F' = 5$ transition is used for cooling and $F = 3 \rightarrow F' = 4$ transition is addressed for re-pumping back into the cooling cycle (see Figure 2.1). Two laser systems are required for the transitions. The Cs laser systems is also discussed in [1].

4.1.1 Lasers and Optical Layout

The cooling light is produced by a *Toptica* DL 100 Pro extended cavity diode laser, which is amplified through a *Toptica* BoosTA tapered amplifier (see section 4.1.1.1). This arrangement produces 600 mW of cooling light which is enough for the MOT, the Zeeman slower and potentially for Degenerate Raman Sideband Cooling (DRSC) [96]. The different detunings that are required for laser cooling are produced by various AOMs, which are outlined in Table 4.1.

The optical layout of the laser system is displayed in Figure 4.1. The light from the DL 100 Pro is initially split into three separate arms using polarising beamsplitters. The light double passed through AOM_1 is coupled into a fiber and subsequently injected into the BoosTA tapered amplifier. This amplified light is used to prepare the various detunings needed for the experiment. Light passing through AOM_4 is used for the Zeeman slower. AOM_5 prepares light for the DRSC and light through AOM_6 is used for the MOT. The second arm out of the DL 100 Pro is double passed through AOM_2 and used for laser locking (see section 4.1.2.1). The third arm through AOM_3 is used for imaging atoms in the MOT (see section 4.1.3). Figure 4.2 shows how the light frequency is shifted by each AOM to create the detunings required for the experiment.

The repump light is generated from a *Toptica* DL Pro. The light is split into 4 arms using polarising beamsplitters. The light passing through AOM_7 is used for locking as outlined in section 4.1.2.2, light passing through AOM_8 is used for repumping atoms in the Zeeman slower, light through AOM_9 is used for repumping atoms captured in the MOT and light passing through AOM_{10} can be used as a polariser for DRSC.

4.1.1.1 Tapered Amplifier

The DL Pro 100 does not provide enough power alone for all the required laser cooling tasks. Hence, in addition, some of the light from the DL Pro 100 is amplified by the BoosTA tapered amplifier. A semiconductor chip inside the amplifier creates a gain region that amplifies the incoming light. The output light will therefore be of the same frequency and spatial mode structure as the seeding light.

The best alignment of the tapered amplifier is achieved when matching the input beam to the weak output from the input facet of the BoosTA in the absence of any seeding. We use anamorphic prisms and two steering mirrors to match the shape and direction of the output beam as closely as possible, which maximises the amplification. The output power of the amplification depends mainly on the seeding power and the

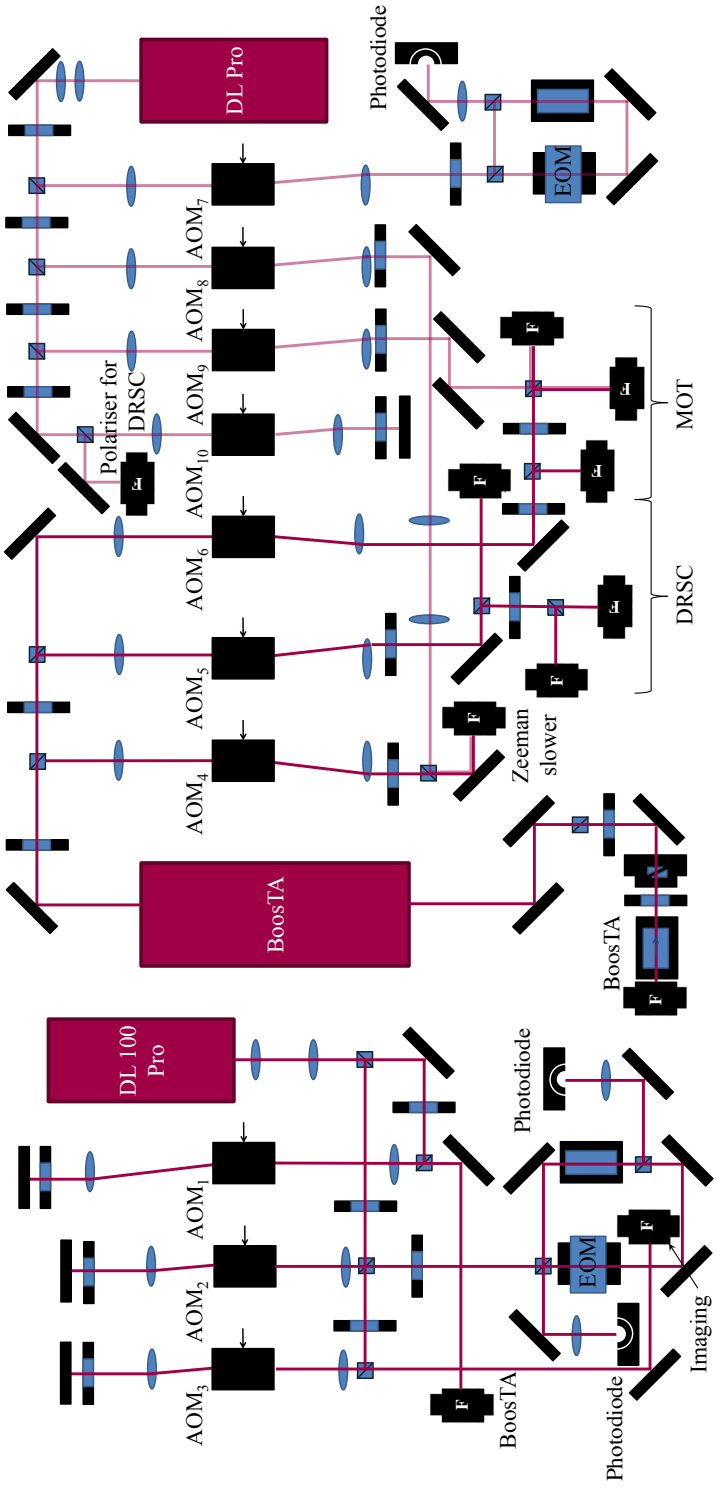

Figure 4.1: Schematic outline of the optical table for the caesium laser system.The DL 100 Pro provides the cooling light and the DL Pro the repump light. [1]

AOM	Model	Purpose	Frequency [MHz]	Detuning [MHz]	Transition
1	Crystal Technology 3110-120	BoosTA	125		
2	Crystal Technology 3200-124	Locking	192	0	$F = 4 \rightarrow F' = 5$
3	Crystal Technology 3200-124	Imaging	192	0	$F = 4 \rightarrow F' = 5$
4	Crystal Technology 3080-122	Zeeman Slower	80	-55	$F = 4 \rightarrow F' = 5$
5	Crystal Technology 3110-120	DRSC	116	1	$F = 4 \rightarrow F' = 4$
6	Crystal Technology 3110-120	MOT	125	-9	$F = 4 \rightarrow F' = 5$
7	Crystal Technology 3080-122	Repump Locking	80	0	$F = 3 \rightarrow F' = 4$
8	Crystal Technology 3110-120	ZS repump	130	-50	$F = 3 \rightarrow F' = 4$
9	Crystal Technology 3080-122	MOT repump	85	-5	$F = 3 \rightarrow F' = 4$
10	Crystal Technology 3200-124	DRSC polariser	216	0	$F = 3 \rightarrow F' = 2$

Table 4.1: The AOMs and their frequencies used in the optical setup for the caesium laser system. AOM 1-6 are used for the cooling laser and 7-10 for the repump transition.

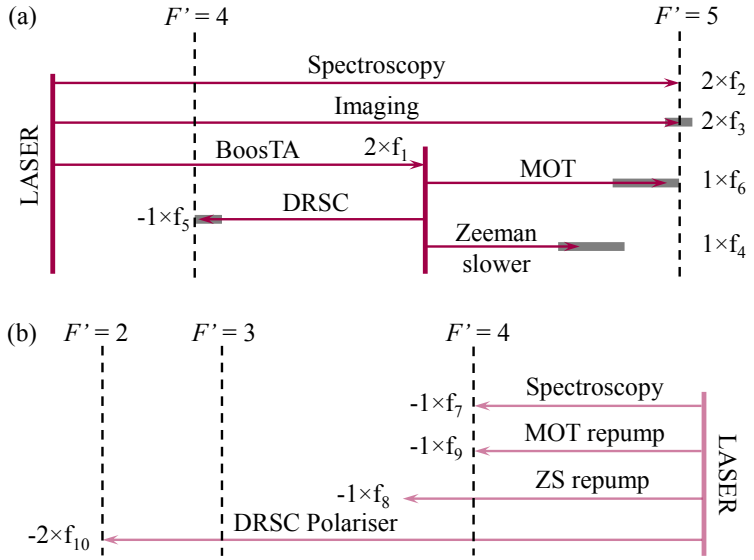

Figure 4.2: Schematic illustration of the frequency shifts provided by the AOMs in the Cs laser system. The frequencies f_1 to f_{10} correspond to AOMs 1 to 10. a) Frequency shifts for the cooling light. b) Frequency shifts for the repump light. The grey rectangles indicate the relevant tuning range of each AOM [1].

supplied current. In order to increase the lifetime of the amplifier we are running it below its maximum current (2150 mA) at 1450 mA. At this current we can expect an output power of roughly 600 mW with 25 to 30 mW seeding power. This is enough power for all applications desired in this experiment.

4.1.2 Frequency Stabilisation

To ensure the lasers remain on resonance with the relevant atomic transition it is essential to frequency stabilise them. For this we use a spectroscopy signal obtained from small caesium vapour cells. There are various techniques that can be employed for laser locking, with each having advantages and disadvantages. The best techniques often depends on the exact level structure of the atomic species in question. For caesium we have chosen to employ a Modulation Transfer Lock [97, 98]. for the cooling laser and a Frequency Modulation Lock [99] for the repump laser. Both techniques, as well as their advantages and disadvantages, are described in detail below.

4.1.2.1 Modulation Transfer Lock

Modulation Transfer is a spectroscopy technique that yields sub-Doppler lineshapes. Bertinetto *et al.* showed that for the $F = 4 \rightarrow F' = 5$ Cs transition, this technique produces good error signals suitable for locking [97]. This technique requires two intense counter propagating beams, which we will call pump and probe beam even though they carry about equal power. In our setup the light from the DL 100 Pro that is passed through AOM_2 is subsequently split by a polarising beam splitter to create the pump and probe beam as outlined in Figure 4.3 (a). The pump beam is passed through an electro-optic modulator (EOM) that will generate sideband frequencies ω_m separated by 5.907 ± 0.008 MHz from the main carrier frequency ω_c. This EOM is made from a lithium niobate crystal (*DÖHRER Elektrooptik*) incorporated into an LCR circuit [98]. This modulated pump beam is passed through a caesium vapour cell, where it collinearly counterpropagates with the probe beam that was split off before. The two frequency components of the pump beam can be transferred to the probe beam due to the nonlinearity of the atomic medium [100]. The probe beam is then detected by a photodiode (*Hamamatsu* S5972), which can detect the beat between the sidebands and the main carrier, if sidebands were transferred to the probe beam. Four wave mixing can be observed at four different frequencies, $\omega_c \pm \omega_m$ and $\omega_c \pm \omega_m/2$. The phase of the generated sideband depends on the pump sideband that formed it. The signal is passed to a frequency mixer (*Mini-Circuits* ZFDC-15-6+) where it is mixed with the initial signal modulating the EOM. The output of the mixer is amplified and filtered by a low pass gain filter, which leaves the relevant DC component that can be used as the error signal.

Figure 4.3 (b) shows a very strong signal for the $F = 4 \rightarrow F' = 5$ transition. The other transitions that can be observed are crossover transitions that will not be discussed further [97]. The signal immediately reveals the advantages of using this spectroscopy technique for this particular transition. As the relevant transition is closed the modulation transfer signal is strongly enhanced and therefore much bigger than for any other transition as the atoms cannot relax into other ground states [100]. Furthermore it produces sharp sub-Doppler features on a zero background as the modulation of the probe beam only occurs with both beams on resonance within the natural linewidth of the transition. This also produces the flat zero background which is a major advantage of this technique. As the effect however is only strong in closed transitions it is not a suitable method for locking the repump laser.

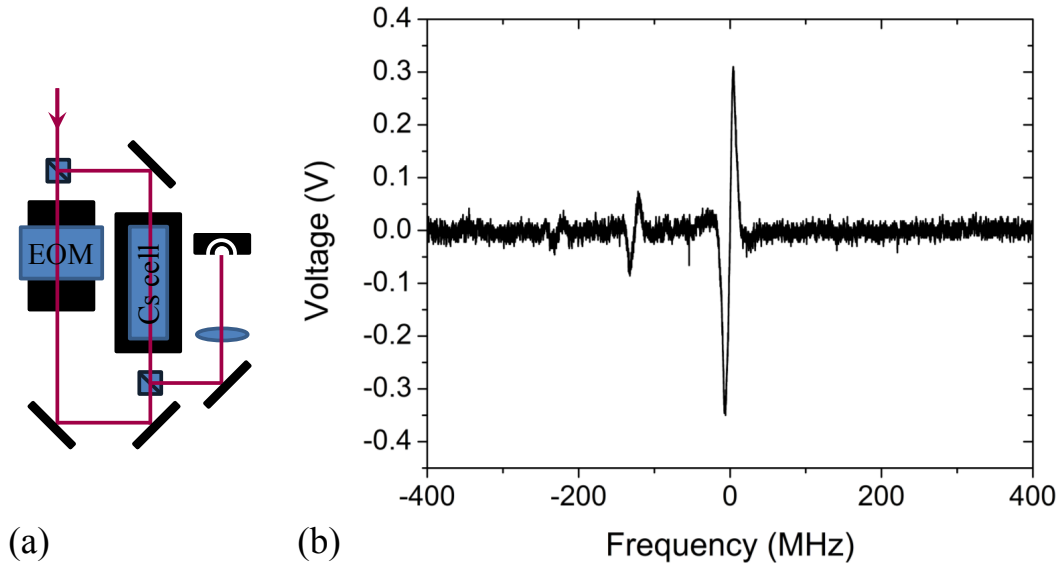

Figure 4.3: (a) Shows the relevant optical layout for the Modulation Transfer Spectroscopy. (b) Shows the transitions from $F = 4$ in Caesium. The largest signal corresponds to the $F = 4 \rightarrow F' = 5$ transition [1].

4.1.2.2 Frequency Modulation Lock

The repump laser is locked using Frequency Modulation (FM) spectroscopy. Similar to the Modulation Transfer it is based on two beams collinearly counter-propagating through a caesium vapour cell. In this case however the two beams do not have equal power, but we have a strongly saturating pump beam and a weak probe beam. In our setup, light from the DL Pro passing through AOM_7 is split on another polarising beam splitter to create the pump and probe beams (see Figure 4.4 (a)). The probe beam (around $55\,\mu W$) is passed through an EOM that produces sideband frequencies ω_m at 8.6437 MHz from the main carrier ω_c. The pump beam (around $135\,\mu W$) is passed through the caesium vapour, where it is overlapped with the counter-propagating probe beam. This pump beam strongly saturates the caesium transition. The probe beam is detected on a fast photodiode (*Hamamatsu* avalanche photodiode, C5460) that can detect a beat signal between the carrier frequency and the sidebands. If the laser is perfectly on resonance, the transition is strongly saturated by the pump and the absorption from the probe beam is small. Hence both sidebands will create a beat with the carrier. However, as the two beat frequencies are the same, but π out of phase, no overall beat will be observed. If the laser is tuned out of resonance two things will

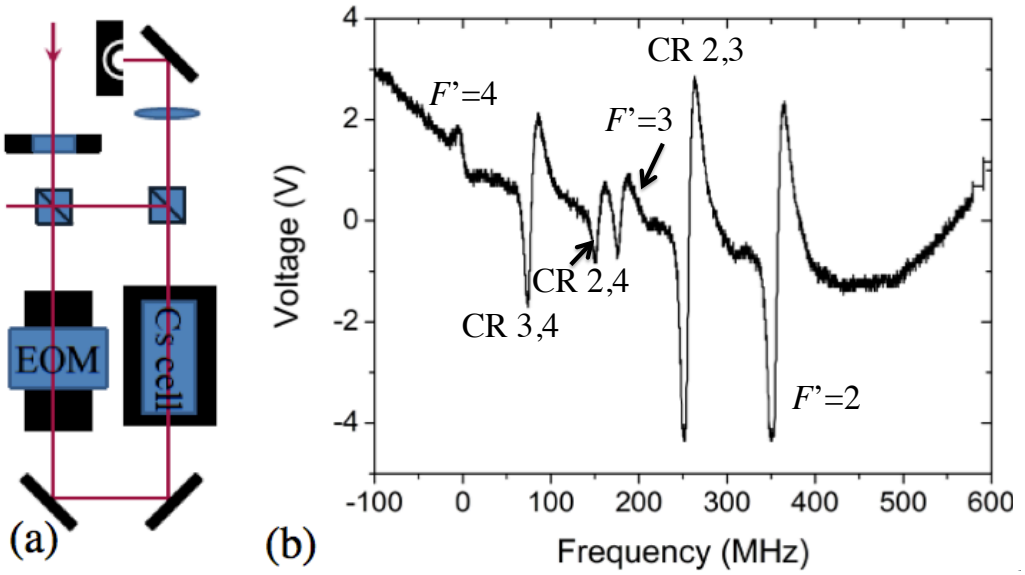

Figure 4.4: (a) The optical layout for the Frequency Modulation spectroscopy. The probe beam passes through the EOM. (b) Frequency Modulation Signal obtained for several transitions from $F = 3$ [1].

happen. The pump laser will not be strongly saturating the transition, but one of the sidebands will be closer to resonance and therefore is absorbed more strongly. This means the beats from the two sidebands will not cancel on the photodiode and a beat signal is observed. As before this beat signal is mixed with the original signal modulating the EOM using a frequency mixer (*Mini-Circuits*, ZAD-3+) and subsequently filtered and amplified.

The signals obtained with this technique are shown in Figure 4.4 (b). All the transitions and cross-overs from $F = 3$ can be observed. We lock the laser to this peak corresponding to the $F = 3 \rightarrow F' = 4$ transition. However, compared to Modulation Transfer spectroscopy the signal is imposed on a non-zero varying Doppler broadened background, which has to be compensated. In practice this means that FM spectroscopy is more vulnerable to power fluctuations of the laser, which can be induced by temperature change. These fluctuations can influence the signal strength of the Doppler broadened background and the saturation peaks.

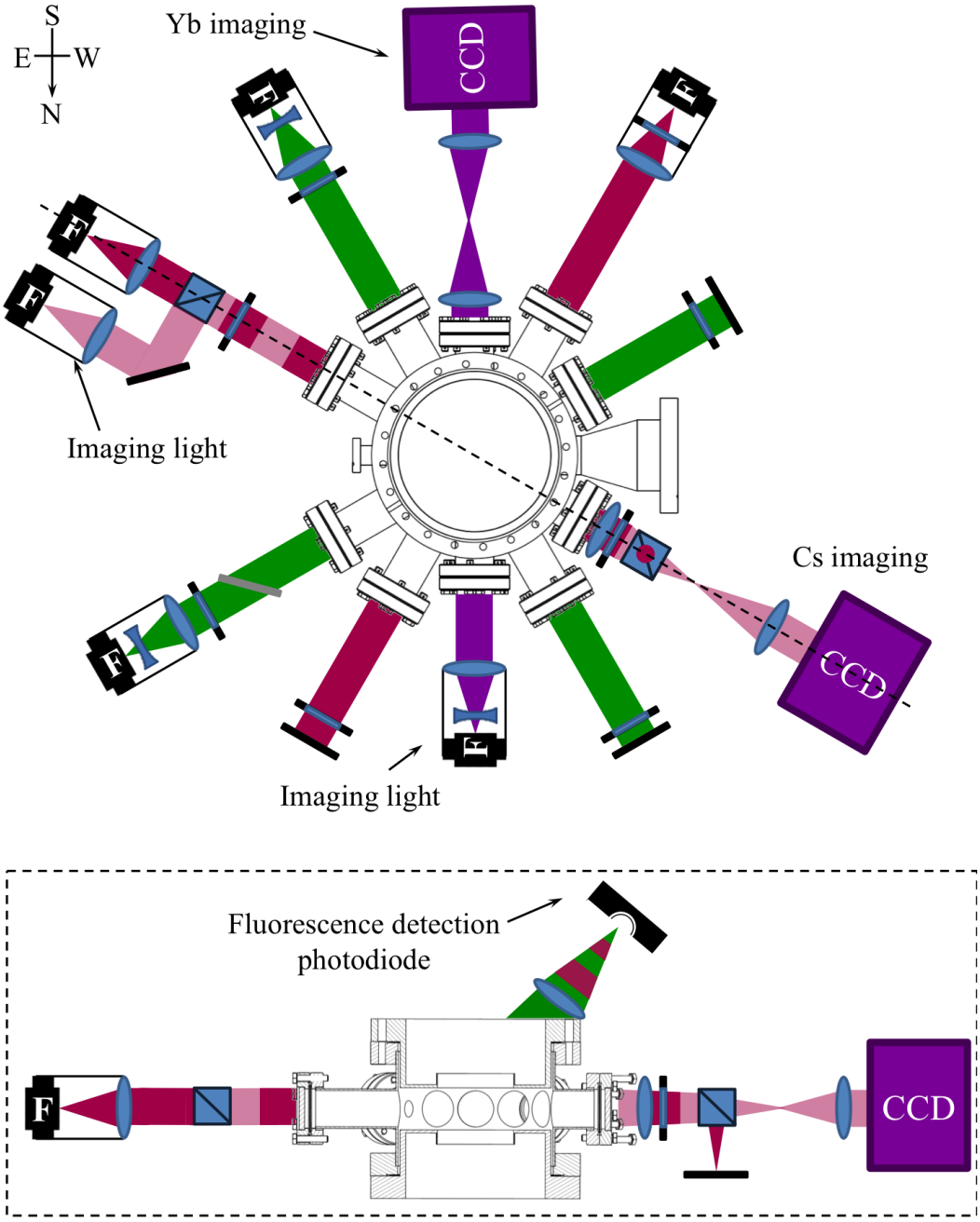

Figure 4.5: Schematic overview of optical setup around the Science Chamber. Caesium beams are illustrated in red, ytterbium beams are green for the MOT beams and purple for the Imaging light. The dashed line indicates the cross-section that is displayed below [1].

4.1.3 MOT, Zeeman Slower and Imaging Optics

All light is transferred to the MOT through optical fibers. Each MOT beam is expanded to a collimated beam of roughly 18.0 mm $1/e^2$ diameter with typically 30 mW power. As shown in Figure 4.1 the repump laser is already combined with the cooling light before the fiber and 13.5 mW is delivered to the MOT. The imaging light is transferred to the MOT through a separate fiber. It is combined with one of the MOT beams via a polarising beam splitter, and then separated again from the MOT beam using a second beam splitter after the MOT chamber (see Figure 4.5). This makes efficient use of the optical access into the Science Chamber. The MOT beams are passed through quarter wave plates to create the appropriate circular polarisation (see section 6.1). They are retro-reflected and double passed through another quarter-waveplate to create the six MOT beams required for trapping. The imaging beams are passed through the MOT chamber and focussed by achromatic lenses to record absorption images on a CCD camera. A photodiode for fluorescence detection is mounted at an angle above the Science Chamber, to take continuous measurements of the MOT. This fluorescence detector was used for most of the optimisation of the MOT and the Zeeman slower. From the voltage measured on the photodiode we can obtain an approximate atom number. The power scattered by N atoms is given by [1]:

$$P = \frac{N\,hc}{\lambda} \frac{C_1^2 I/I_s}{1 + 4\delta^2/\Gamma^2 + C_2^2 I/I_s}\,, \tag{4.1}$$

where C_1 and C_2 are the Clebsch-Gordan co-efficients, which are given as $C_1 = C_2 = 0.73 \pm 0.1$ by Townsend *et al.* [101]. The percentage that will hit the photodiode will depend on the diameter of the iris in front of the diode d and the distance between the MOT and focussing lens L:

$$P_{\mathrm{PD}} = \frac{d^2}{16L^2} P\,. \tag{4.2}$$

This power can be related to the voltage measured over the photodiode:

$$V_{\mathrm{PD}} = \mathcal{R}(\lambda)\, P_{\mathrm{PD}} R\,, \tag{4.3}$$

where R is the load resistance over the photodiode and $\mathcal{R}(\lambda)$ is the responsivity of the photodiode to light at frequency λ. Combining the above equations the atom number

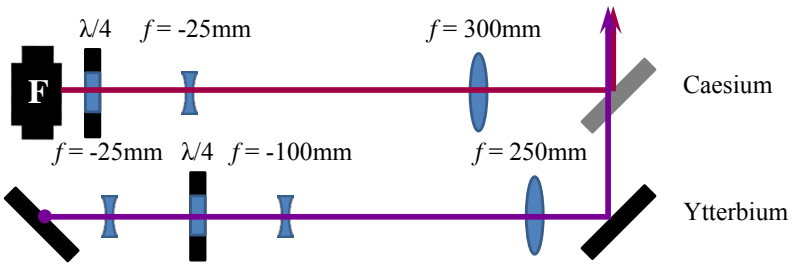

Figure 4.6: Optics setup to create both the ytterbium and caesium Zeeman slower beams. The caesium Zeeman beam is shown in red and the ytterbium Zeeman beam is shown in purple [1].

is given by:

$$N = \frac{16L^2}{d^2}\,\frac{V_{\mathrm{PD}}}{\mathcal{R}(\lambda)R}\,\frac{\lambda}{hc}\,\frac{2}{\Gamma}\,\frac{1+4\delta^2/\Gamma^2+C_2^2 I/I_s}{C_1^2 I/I_s}\,. \tag{4.4}$$

Unless otherwise indicated this equation was used to determine the atom number in all Cs experiments.

The Zeeman slowing light has 6.0 ± 0.1 mW cooling light and 2.76 ± 0.1 mW repump light, that are combined before the fiber. The light is shaped by a $f = -25$ mm lens and $f = 300$ mm lens as displayed in Figure 4.6. This gives a beam that is focussed down to a $89\pm1\,\mu$m waist, 2.09 ± 0.01 m away from the Zeeman slower viewport. The focussing of the Zeeman beam is discussed in section 5.3. A dichroic mirror is used to combine the two beams for Yb and Cs, and align them down the Zeeman slower.

4.2 Laser system for Ytterbium

For ytterbium we need light on resonance with the $^1S_0 \rightarrow {}^1P_0$ transition for the Zeeman slower and with the $^1S_0 \rightarrow {}^3P_1$ transition for the MOT. The 399 nm light needed for the $^1S_0 \rightarrow {}^1P_0$ transition is often produced using a frequency doubled laser system [102, 103]. However the development of cheap 405 nm semiconductor diodes has made it possible to build a more affordable laser system at 399 nm [104, 105, 106]. We therefore have chosen to build a diode based 399 nm laser system which is described in detail below.

The $^1S_0 \rightarrow {}^3P_1$ transition is often produced using either a frequency doubled diode [107] or fiber laser [108]. Such lasers are now available commercially and the *Menlo Systems* fiber laser used in this work is described in section 4.2.3.

4.2.1 Overview and Optical Layout

The 399 nm laser system is outlined in Figure 4.7. I will refer to it as the blue laser throughout this thesis. It is based on two NDV4313 diode lasers from *NICHIA*. One is in an external cavity diode laser (ECDL) (see section 4.2.2.1). The second diode (Slave) is seeded by the first (see section 4.2.2.2). The light from the Slave is spatially filtered through a 50 μm pinhole and used for Zeeman slowing (see section 4.2.5). Some light is passed through a fiber to a transfer cavity lock and a wavemeter (621 Series, *Bristol Instruments*) (shown in Figure 4.8). The transfer cavity lock is explained in section 4.2.2.3 and the wavemeter is required to determine the frequency of the laser. Both the Slave and ECDL are injected into a Fabry-Perot spectrum analyser (SA200, *Thorlabs*) so the mode structure can be investigated throughout running the experiment. Furthermore some light from the ECDL is also passed to the oven for spectroscopy.

The 556 nm light is generated from a Orange One fiber laser from *Menlo Systems* (see section 4.2.3). Figure 4.8 shows the optical layout used to lock the laser frequency and generate the MOT beams. The laser output is split in two, and each part is passed through an AOM (46200-0.3-LTD, *Gooch and Housego*) with most of the power passing through AOM_{11}. This light is used to form the MOT beams and is therefore split equally onto three fibers. The remainder of the light is passed through AOM_{12}, which is used for locking. The lock for the green laser is based on spectroscopy from an ytterbium beam. Several different methods have been explored which are outlined in section 4.2.3. Some light is also combined with the 399 nm ECDL light and coupled into a Fabry-Perot spectrum analyser (SA200, *Thorlabs*) for the transfer cavity lock.

4.2.2 399 nm Laser system

4.2.2.1 Extended Cavity Diode Laser

Extended cavity diode lasers have become a standard tool for many laser applications [109]. They are based on a laser with a grating, which is normally placed in the Littrow configuration (see Figure 4.9). The 1st-order diffraction from the grating is aligned back into the diode so that the grating and the back facet of the diode form an extended cavity. There are several factors influencing the frequency of the ECDL, which are illustrated in Figure 4.10. The optical gain medium of the laser can typically lase with a wide spread of frequencies. The laser must lase on a mode of the cavity,

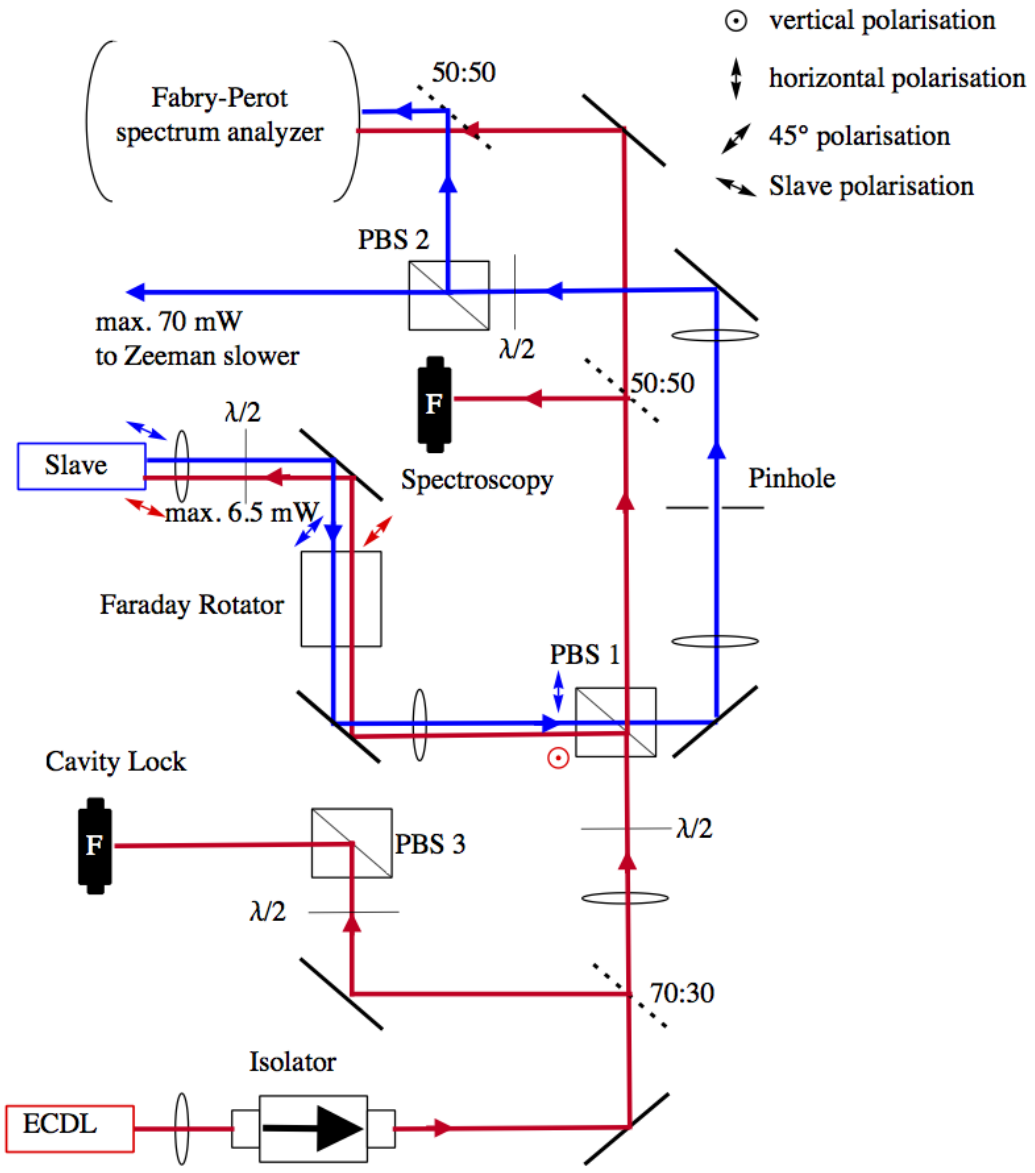

Figure 4.7: Layout of the 399 nm Laser system creating the Zeeman slowing light. The polarisation in front of the slave laser is illustrated with little arrows. For clarity, overlapping laser beams are drawn parallel to each other. PBS 3 cleans up the polarisation of the beam before it is coupled into the polarisation maintaining fiber. Not to scale.

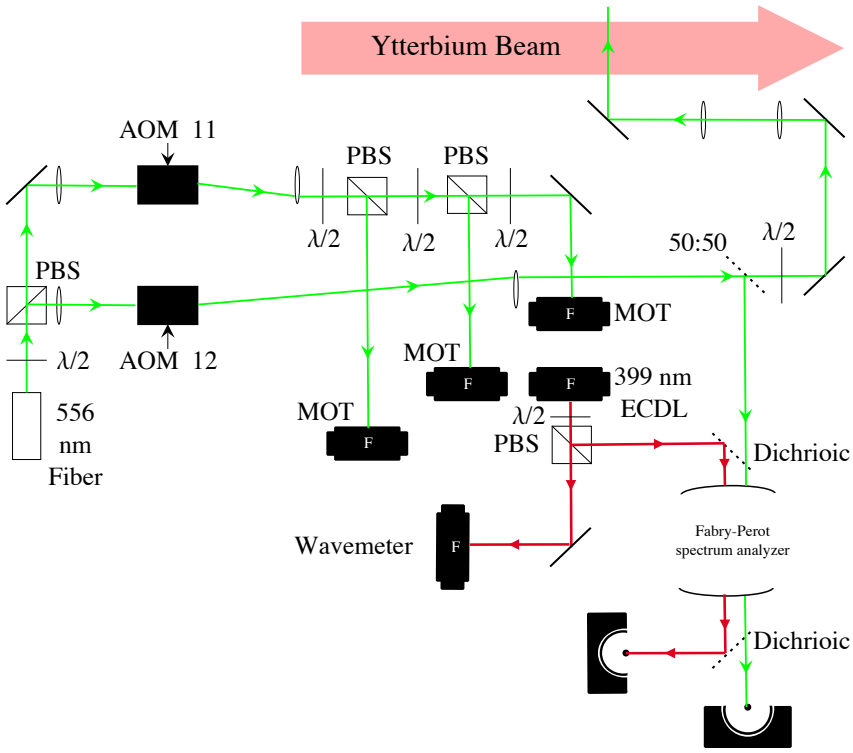

Figure 4.8: Layout of the 556 nm Laser system for the MOT light and the Transfer Cavity Lock. The atomic beam is generated from a beam machine. The 399 nm ECDL light is shown in red. For clarity overlapping laser beams are drawn parallel to each other. Not to scale.

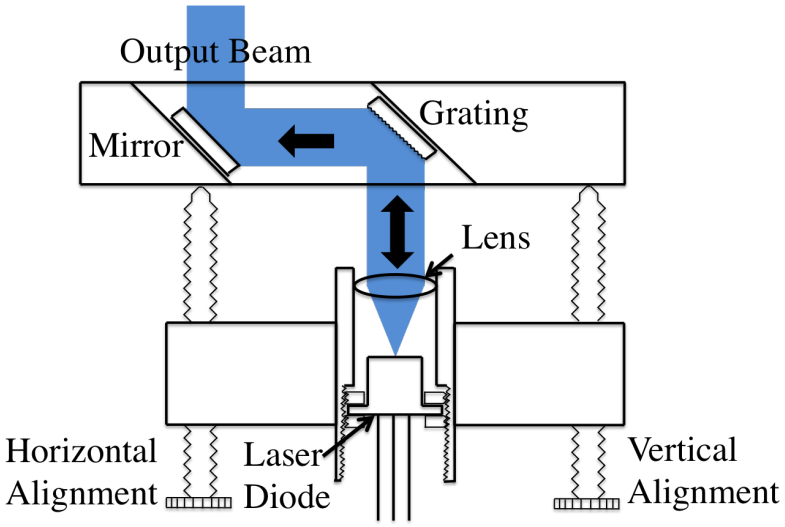

Figure 4.9: Illustration of Extended Cavity Diode Laser (ECDL). The grating is in the Littrow configuration so that the first order is reflected back. The mirror is there so changes in the grating do not affect the pointing of the output beam. Not to scale.

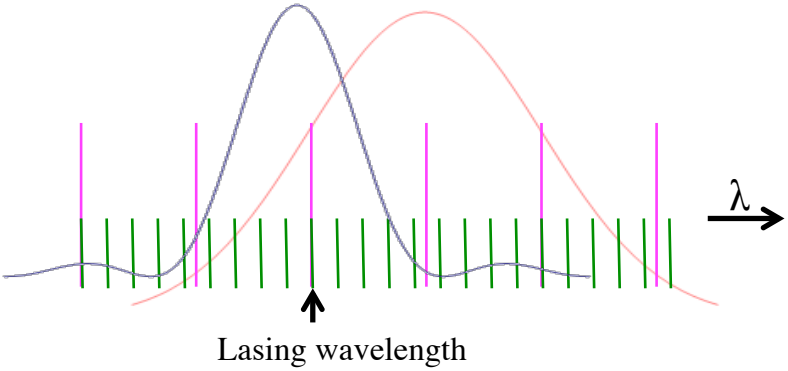

Figure 4.10: Illustration of the modes supported by the extended cavity diode laser. The light red curve shows the gain curve of the optical gain medium inside the laser. The purple curve shows the frequency distribution of light reflected back into the cavity from the grating forming the extended cavity. The green lines show the lasing modes supported by the cavity of the diode. The pink lines show the modes supported by the external cavity. The laser can only lase on a mode supported by all four curves.

whose mode wavelength, λ_n, satisfy:

$$L_c = \frac{n\,\lambda_n}{2}, \tag{4.5}$$

where L_c is the length of the cavity and n can be any integer. The grating limits the range of the possible lasing wavelengths. The first order reflection of the grating is directed back into the laser, so that there are now two cavities, the short cavity of the diode itself, and the much longer cavity formed with the grating. A strong lasing mode only exists if the lasing wavelength is supported by both cavities.

There are several ways to tune the frequency of an ECDL. The angle of the grating with respect to the laser directly controls the frequency of the light that is reflected back into the diode laser. Only if there is enough light coupled back can the external cavity have an impact. The modes supported by this cavity can be easily influenced by moving the grating thereby extending or contracting the cavity length. The optical length of the internal cavity can be tuned via the operating temperature, and the refractive index of the gain medium can be tuned via the current of the laser. With all these controls it is possible to tune the diode laser to a single lasing frequency that is supported by the optical gain medium.

The *NICHIA* diode laser for the ECDL laser diode is used with a grating having 1800 grooves/mm (GR13-1850, *THORLABS*). The grating is placed on an adjustable mirror mount to roughly tune the angle of the grating and retro-reflect the light from the laser. There is a piezo-element in the horizontal alignment of the mirror mount, which allows for fine tuning of both the cavity length and the reflected frequency. Furthermore we place a small mirror on the same mount to ensure that changing the grating angle does not change the pointing of the output beam as outlined by Hawthron *et al.* [110].

We investigated the single mode behaviour of the ECDL laser using a scanning Fabry-Perot Cavity with free spectral range of 1.5 GHz and a finesse of 250. For a perfectly aligned beam the cavity therefore has a resolution of 7.5 MHz. The three peaks seen in Figure 4.11 are separated by the free spectral range and represent the same lasing mode. Fitting a Lorentzian to the peak gives a fullwidth at half maximum of 22 $\pm$1 MHz. As we have not fully optimised the mode matching into the the Fabry-Perot cavity, it is likely that this linewidth is broadened by excitations into transverse cavity modes. As the measured linewidth is smaller than the natural linewidth of the relevant transition the laser linewidth was not investigated further. An investigation

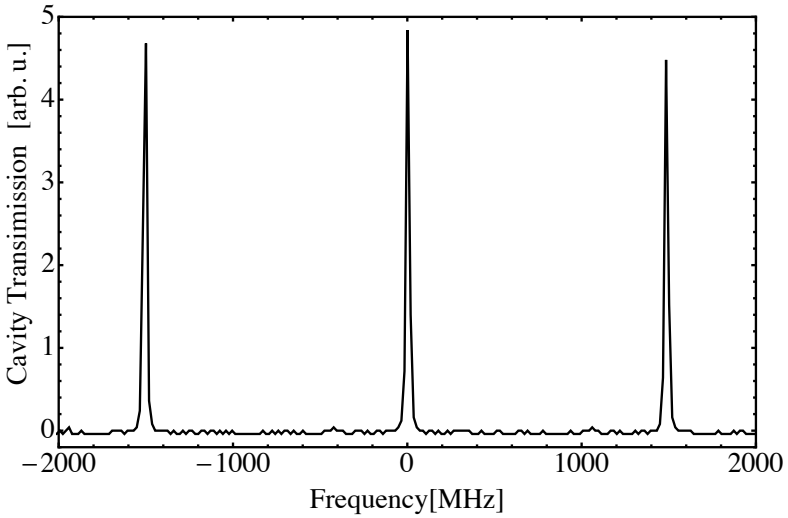

Figure 4.11: Transmission peaks of ECDL laser light through a scanning Fabry-Perot Cavity. The laser shows good single mode behaviour.

of linewidth narrowing for ECDL lasers can be found in [111] and [112]. Using the piezo controlling the grating and the driving current of the diode, it is possible to scan the frequency of the laser for several GHz without mode hop. This is most easily demonstrated by scanning over several ytterbium isotopes and measuring the fluorescence from the atoms. Figure 4.12 shows that the entire ytterbium spectrum can be obtained in a single scan.

Since some of the laser power is reflected back in the ECDL configuration the total laser power is reduced. At a typical current of 70 mA we can obtain about 50 mW. Considering losses in the isolator and other optical components this is not enough for both frequency locking and for the Zeeman slower. Therefore the light from the ECDL is used to inject a slave diode.

4.2.2.2 Injection Seeding

Injection seeding is a technique commonly employed to force the output mode of a laser, usually called the slave, to match that of a second laser, called the seed. This is done by sending some light from the seed into the slave. This has previously been achieved with 399 nm diodes with a similar setup to the one described here[104, 105, 106].

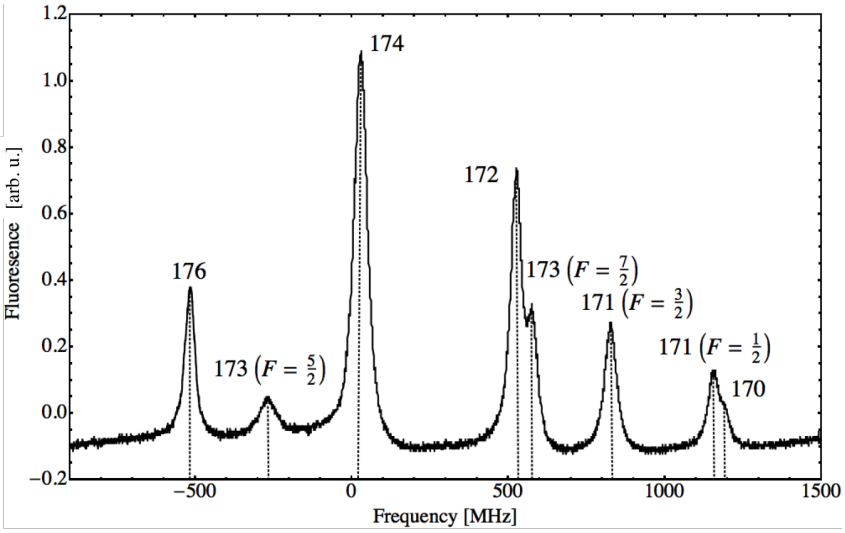

Figure 4.12: Fluorescence spectrum of ytterbium isotopes obtained with a single scam of the ECDL laser in the Beam Machine.

Overview To inject the slave laser we need to counter-propagate the seed light with the slave laser output. If injection works the slave will copy the exact mode from the seed beam. Since the polarisation will also be copied it is not trivial to separate the slave light from the seed light. We use two wave plates, a polarising beam splitter and Faraday rotator to achieve this. The scheme is shown in Figure 4.7, in which little arrows indicate the polarisation of the seed and slave laser beams. A $\lambda/2$ waveplate rotates the polarisation of the seed light so that it is reflected by the polarising beam splitter. The seed light is then vertically polarised. The seed beam passes through a Faraday rotator which rotates the polarisation clockwise by 45°. Subsequently a second $\lambda/2$ rotates the polarisation to the angle which optimises the injection of the slave laser. The slave output passes through the same waveplate and is therefore rotated back to the same 45° polarisation. The polarisation is turned 45° counter-clockwise by the Faraday rotator as the beam is travelling in the opposite direction. Hence the slave laser beam will be horizontally polarised after the Faraday rotator, which means it is passed through the polarising beam splitter (PBS1). This forms the output beam for the Zeeman slower.

The full theory of injection seeding diode lasers is highly complex and goes beyond the scope of what can be discussed here [113, 114]. In principle if the light that is injecting the slave is supported by its cavity, the photon count of the injected light

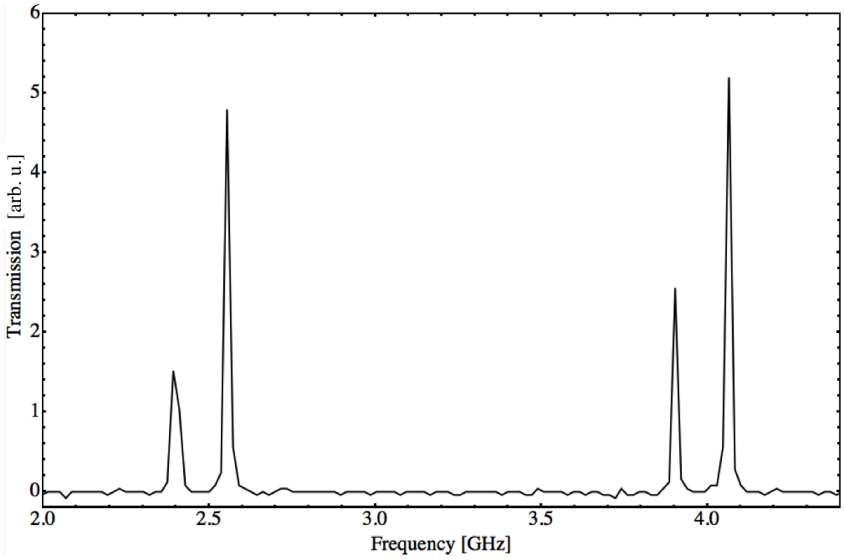

Figure 4.13: Scanning Fabry-Perot cavity spectrum of injected BALD laser. The small peak corresponds to the injected mode.

should build up in the slave cavity. The effective cavity length of the slave can be controlled by changing the operating current of the slave laser and therefore can always be matched to the incoming mode. With enough injected light in the slave cavity the preferred stimulated emission of the optical gain medium will be on the same mode. However too much light can lead to relaxation oscillations inside the slave laser, which will lead to a modulated output [115].

Injection seeding of two different diodes was attempted in this project. A Broad Area Diode Laser (HL40023MG, *opnext*) was used in the first attempts. The advantage of this diode was that up to 400 mW of power could be obtained. In a second attempt we injected a second NDV4313 *NICHIA* diode. This allowed for the simple setup shown in Figure 4.7. The results for both setups are presented below.

Broad Area Laser Diode The Broad Area Laser Diode (BALD) uses a larger area optical cavity and gain medium, which allows it to lase simultaneously on several cavity modes. It is therefore harder to bring to lase on a single mode. The BALD was injected using the same scheme outlined above, however extensive reshaping of the seed beam was required as the spatial modes of the two lasers was very different. This made it complicated to achieve good injection. Hence single mode injection was

only achieved at operating currents below 160 mA giving a maximum output power of 75 mW. At higher slave operating currents it wasn't possible to suppress all other modes (see Figure 4.13), and therefore less than 30% of the light was emitted in the injected mode. As this setup is also very fragile to vibrations and laser fluctuations, the BALD was abandoned for a second *NICHIA* diode that was easier to inject.

Single-mode Diode Injecting a second *NICHIA* diode is less complicated as the spatial output beam is the same as the ECDL diode. Therefore no reshaping of the ECDL beam is required to achieve optimal injection. However the injection is still very critical on the right operating current of the slave laser and the power of the seeding light. Good injection can only be found at a few operating currents. These points of good injection typically only span about 0.2 mA current deviation. This occurs as the slave current influences the refractive index of the gain medium and therefore the cavity optical length, which has to be matched to the incoming mode. Furthermore, relaxation oscillations modulating the output frequency can be observed with too much injection power. These can be eliminated by tuning the input power and the slave driving current. With this arrangement we obtain 100 mW single mode light using an injection power between 3 - 6.5 mW. The injection can be stable for several hours, but typically requires fine tuning after 30 minutes. The parameter that needs to be tuned depends on the mode structure observed from the slave by the spectrum analyser. In case the seed has drifted small regular additional modes are observed. They can be corrected by tuning the piezo grating of the ECDL. A drift in the slave laser usually results in stronger irregular modes. They can be corrected by either reducing the injection power or tuning the current of the slave laser. While this is not ideal, it is sufficient for loading a magneto-optical trap and obtaining consistent data.

4.2.2.3 Transfer Cavity Lock

Locking the blue laser at the right frequency could be achieved similarly to the caesium setup, by using the fluorescence or absorption from an ytterbium vapour. This would then require a subsequent shift of the frequency by several hundred MHz for the Zeeman slower (see section 5), which can be achieved with an AOM setup. However such a setup would require several double passed AOMs and allows for less control of the Zeeman frequency. This makes it beneficial to lock the laser directly at the frequency that is required for Zeeman slowing. We achieve this with help of the 556 nm laser, which

is locked to a fluorescence signal (see section 4.2.3.4), and a Fabry-Perot spectrum analyser. Such a lock is normally called a Transfer Cavity Lock (TCL) [116].

Overview The optical setup is shown in Figure 4.8. The 399 nm light and the 556 nm light are combined on a dichroic mirror and coupled into a scanning Fabry-Perot cavity. The light transmitted through the cavity is split on a second dichroic mirror and detected by two separate photodiodes. The signal of both photodiodes is sent to a computer that analyses the signal and controls the lock. It sends a voltage feedback to the piezo and the operating currents of the slave and ECDL lasers. Some light from the 399 nm ECDL is also passed to a wavemeter, which is required to have a rough frequency reading.

Theory For this discussion we will assume that both lasers are single mode and that the green laser can be used as an absolute frequency reference as it is locked separately. As the length of the cavity is being scanned by applying a voltage ramp $V_\mathrm{r}(t)$ to the cavity piezo, the photodiodes will register transmission peaks for each laser. We will assume for now that there is just one cavity transmission peak for each laser. Each peak will occur at a distinct time during the ramp, t_b and t_g for the blue and green laser respectively. Those times can therefore be matched to a cavity voltage $V_\mathrm{b} = V(t_\mathrm{b})$ and $V_\mathrm{g} = V(t_\mathrm{g})$. The transfer cavity lock software takes the difference $\Delta V = V_\mathrm{b} - V_\mathrm{g}$ and sends a feedback signal to the blue laser to keep this difference constant. It is easy to see why this is equivalent to stabilising the frequency of the blue laser. The cavity length at the green peak and blue peak can be given as $L_0 + L_\mathrm{g,b}$. The length of the cavity changes proportionally with the supply voltage to its piezo, hence:

$$L_\mathrm{b} = \alpha V_\mathrm{b}\,, \tag{4.6}$$

$$L_\mathrm{g} = \alpha V_\mathrm{g}\,, \tag{4.7}$$

where α is some constant factor. Also for a transmission peak to occur the length of the cavity needs to be an integer of half the wavelength of the laser:

$$L_0 + L_\mathrm{b} = m\frac{\lambda_\mathrm{b}}{2}\,, \tag{4.8}$$

$$L_0 + L_\mathrm{g} = n\frac{\lambda_\mathrm{g}}{2}\,. \tag{4.9}$$

By subtracting the first from the second equation and converting to voltages:

$$\Delta V = V_\mathrm{b} - V_\mathrm{g} = \frac{1}{2\alpha}(m\lambda_\mathrm{b} - n\lambda_\mathrm{g}). \tag{4.10}$$

In this equation λ_g and n are fixed due to the green laser being locked and the cavity length never drifting so far that n changes. m can be determined by using the wavemeter, which can determine the frequency of the laser to a few hundred MHz, which is much smaller than the 1.5 GHz free spectral range of the cavity. Hence the above equation gives a direct relation between ΔV and λ_b, therefore if ΔV is kept constant by the TCL, λ_b will be fixed.

The above considerations all assumed L_0 to be a constant, however the intrinsic length of the cavity can vary with temperature. Ideally we want the start and end length ($L_0 + L_\mathrm{s}$ & $L_0 + L_\mathrm{e}$) of the voltage ramp to remain constant. However small temperature variations can lead to small variations in the length δL. Hence if a length change like this occurs the transmission peak for the green laser will now occur at $V_\mathrm{g} + \delta V = \frac{1}{\alpha}(L_\mathrm{g} + \delta L)$. But δV can be measured as a deviation from where the green peak was measured in the previous iteration. Therefore by adding $-\delta V$ as an offset to the voltage ramp V_r, the temperature drift can be corrected for.

Programming and Hardware The program was written in C#. The voltage inputs and outputs are controlled through a PCI-MIO-16XE-10 from *National Instruments*. The program reads in the voltages from the two photodiodes and the voltage ramp supplied to the cavity. It outputs a voltage to lock the blue laser frequency and a second voltage to stabilise the cavity from temperature drifts.

The first stage of the program reads in the voltage ramp and the signals from the photodiodes simultaneously. This is important so that the ramp voltage can be associated with the signals from the photodiode. The cavity transmission peaks can then be plotted against the cavity voltage as shown in Figure 4.14. The program will then attempt to find the peaks in the data for both the green and blue lasers. It will do a preliminary analysis, by simply checking if there is any data above a certain set

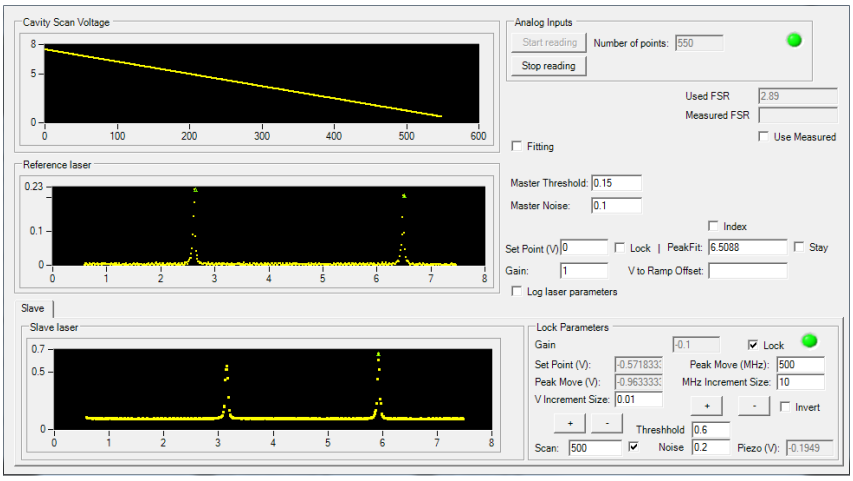

Figure 4.14: User Interface of the TCL program. The three panels show the inputs of the cavity ramp, the photodiode for the green laser and the photodiode for the blue laser in order. The controls for the program are on the right.

threshold. It also counts how many peaks are identified. If the requirement is fulfilled it can fit the peaks using two different methods. The more accurate approach will fit Lorentz distributions to all the observed peaks. This is time consuming, but does give an accurate fit of the peaks. The second method will take all the points above a certain noise level and use them to calculate an average position for each peak. This method is less precise, but since the evaluation is quicker the repetition rate of the lock can be improved. The program will record the voltages corresponding to all observed peaks in two arrays. When the lock is engaged it will take the first entry of each array and calculate the voltage difference.

While the lock is engaged the program will continuously calculate this voltage difference and output a voltage to keep it constant. The voltage V_i after iteration i of the lock is simply given as:

$$V_i = V_{i-1} + G \times (\Delta V_{\text{set}} - \Delta V_{\text{meas}}) \,, \tag{4.11}$$

where G is a gain that can be set in the program, ΔV_{set} is the set point voltage difference that needs to be controlled and ΔV_{meas} is the measured voltage difference after that iteration. This voltage output is supplied to a simple voltage divider that produces three voltages proportional to each other. These three voltages are passed to the piezo control of the ECDL grating, the ECDL laser current control and the slave current

control. By setting the ratios of these three voltages correctly the single mode laser peak can be moved for several GHz without a mode hop and can be stabilised for several hours.

When a mode hop occurs the previously set threshold becomes important. The transmission peaks after a mode hop are typically significantly smaller than during single mode operation. By setting the threshold carefully the laser lock stops when a mode hop occurs. This is desirable as it makes it easier to regain the previous mode.

As discussed in chapter 5 the laser frequency will need to be controlled according to the magnetic field offset. Even though the detuning can be calculated it is unlikely that a MOT can be found without scanning the frequency of the Zeeman laser. The frequency of the Zeeman laser can be controlled by simply changing the set voltage difference ΔV_{set}. For taking measurements however it is quite important to translate this voltage difference into an actual frequency scale. We can use the free spectral range of the cavity, which can be measured out in terms of a voltage difference, to get a frequency calibration. This can be used to to vary the frequency in absolute steps. Alternatively it is possible to calibrate the cavity by observing fluorescence from the different ytterbium isotopes. For each isotope the movement of the cavity transmission peak can be recorded, which can be related to the known spectrum of Yb.

4.2.3 556 nm Laser System

The *Menlo Systems* Orange One is a fiber laser, that uses a Yb^{3+}-doped silica *NKT Photonics BASIK Module* laser between 1020 and 1120 nm. It is frequency doubled in this setup to generate the 556.8 nm needed to address the Yb transition. The generated 1113 nm light is amplified in three stages and can generate up to 300 mW of power at 556 nm. We have not performed detailed measurements on the laser as it was thoroughly tested by the manufacturer. It produces < 50 kHz linewidth and can be tuned in frequency by changing the temperature of the fiber and the voltage applied to a piezo, which applies strain to the fiber. The piezo can scan the laser over roughly 1 GHz. Below we discuss the techniques used to frequency stabilise the laser.

4.2.3.1 Spectroscopy Chambers

Several different spectroscopy sources were explored through this work. These include an ytterbium dispenser cell, a vapour cell and a beam machine. The dispenser cell

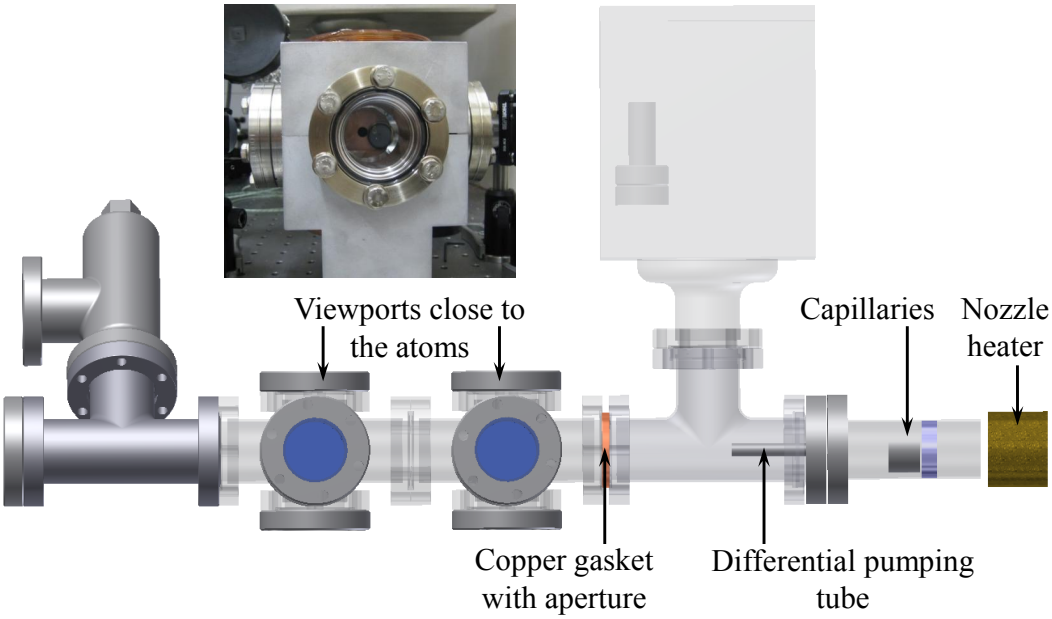

Figure 4.15: The Beam Machine used for ytterbium spectroscopy and locking. The photo shows the ytterbium deposit on the back window [1].

uses a small source of ytterbium that is heated by supplying a large current to a thin metal housing. As the ytterbium gets hot, it will spray out in a large cone. This source releases a large amount of ytterbium and can therefore give a strong absorption and saturated absorption signals. The drawback is that the ytterbium is quickly depleted and has to be replenished frequently.

An ytterbium vapour cell was attempted briefly. It provides a good signal initially, however needs to be kept at a high temperature. When the ytterbium cools down it settles on the windows and blocks all optical access. This might be prevented by using different window material, but was not further pursued.

The spectroscopy source that was used in the final setup was a beam machine. It relies on a simple ytterbium oven with the exit aperture formed by 55 capillaries that create a collimated ytterbium beam. The setup is very similar to the main oven described in section 3.2.1. The final vacuum system is illustrated in Figure 4.15. The oven is heated by a nozzle heater up to around 480 °C. The beam passes through a narrow differential pumping tube and a copper gasket with an 8 mm hole drilled to reduce the beam spread. Subsequently two 6 way crosses with viewports can be used for optical access. The chamber is permanently pumped by a $55\,\mathrm{l\,s^{-1}}$ ion pump (Vac

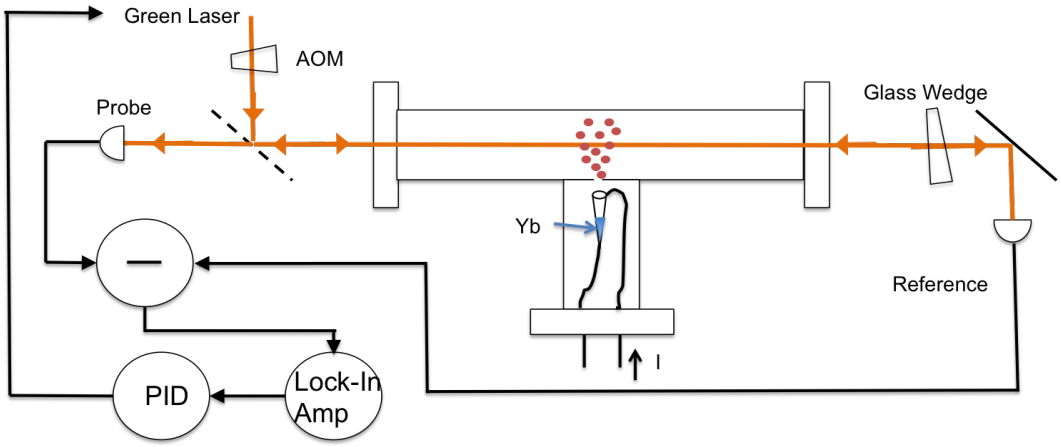

Figure 4.16: Locking setup for saturated absorption spectroscopy with a dispenser cell. The frequency is modulated by an AOM. The intense pump is retroreflected by a glass wedge to create the weak probe beam. Absorption signals from both pump and probe are recorded and subtracted from each other. A Lock-In Amplifier generates an error signal, which is then fed to a PID loop to lock the laser.

Ion Plus 55, *Varian*). This ion pump is surrounded by a mu-metal shield to minimise stray magnetic fields in the spectroscopy section. A valve is included to connect a roughing and turbo pump for initial pumping. This setup produces a significantly less intense ytterbium source compared with the dispenser, but it lasts a lot longer.

4.2.3.2 Saturated Absorption Spectroscopy

The saturated absorption spectroscopy was mainly attempted using the dispenser cell. As it releases ytterbium in a large cone, the obtained spectrum will be strongly Doppler broadened. We therefore need to obtain a Doppler-free feature to lock the laser with enough precision. Saturated absorption occurs when an intense pump beam is counter-propagated with a weak probe from the same laser. The setup is shown in Figure 4.16. If the laser is on resonance the atoms travelling perpendicular to the beam are strongly saturated. The counter-propagating beam can therefore not interact with these atoms and very little light is absorbed. This dip in absorption occurs only for those atoms with zero velocity component in the direction of the lasers. For atoms with non-zero velocity the pump and probe are oppositely Doppler shifted. When scanning the laser over the transition this can therefore be observed as a peak inside the Doppler broadened absorption feature (see Figure 4.17).

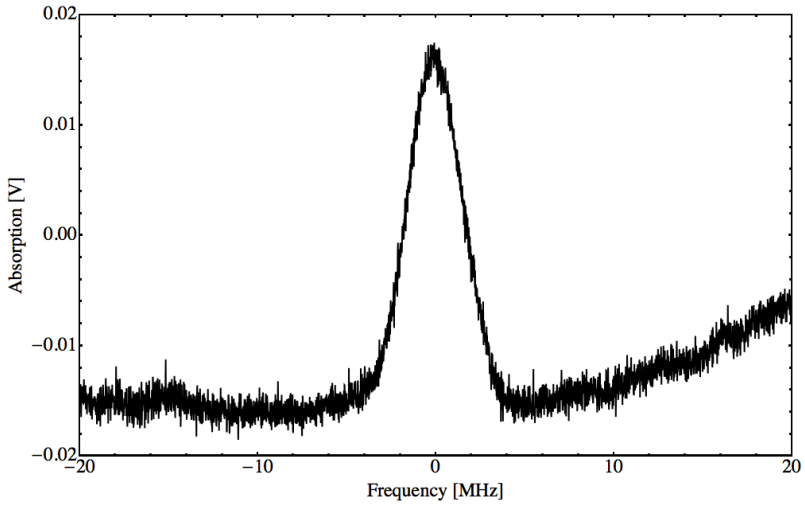

Figure 4.17: Saturated absorption feature obtained from the dispenser cell. The peak has a FWHM of 3.6 MHz.

The saturated absorption peak shown in Figure 4.17 has a linewidth of 3.6 MHz, which is narrow enough to achieve good locking. To eliminate the Doppler broadened background we measure the absorption of the pump beam, which does not have a saturated feature and subtract this from the absorption of the probe beam. To lock to this signal we are modulating the frequency of the AOM at around 3 kHz. The saturated absorption signal is modulated at the same frequency and the amplitude of this modulated output signal is proportional to the gradient of the saturated absorption peak. This is zero on resonance, large at the sides of the peak and small again in the wings. The output therefore has the typical dispersion shape, with a zero crossing at resonance. This error signal can be used to lock the laser.

Even though the locking achieved this way was satisfactory, it was not chosen for the final design as the dispenser depleted of ytterbium too quickly. It needed to be refilled about every second week, which involved a lot of work and was therefore too impractical.

4.2.3.3 Frequency Modulation Spectroscopy

Frequency Modulation spectroscopy was attempted using the Beam Machine. The setup with an EOM closely resembled the caesium setup shown in Figure 4.4 (a). We used an EOM with a resonance frequency of around 9 MHz. The electronic components

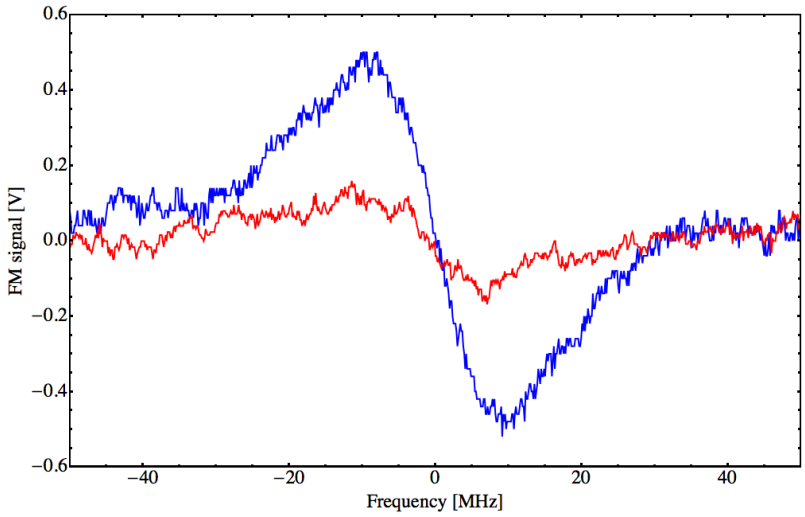

Figure 4.18: Frequency Modulation signal of the 556 nm laser in the Beam Machine. Signal obtained with a single pass through the Yb is shown in red, and with 5 passes in blue.

used to extract the dispersion signal were the same as in the caesium setup (see section 4.1.2.2). However only a weak FM signal was observed. To enhance the signal we attempted to pass it through the atomic beam 5 times. This lead to moderate success and a dispersion signal with a peak to peak width of roughly 20 MHz (see Figure 4.18). This is sufficient for locking, however even after 5 passes the signal remains very noisy. This led to the lock being unstable.

4.2.3.4 Fluorescence Spectroscopy

For the final setup the laser was locked simply to a Doppler broadened fluorescence signal. The main challenge in this is detecting a strong fluorescence peak due to the transition's narrow linewidth. We therefore use a large gain photodiode in a special housing to maximally amplify the signal. We also use lenses and mirrors to direct most of the fluorescence onto the photodiode (see Figure 4.19).

A lens and mirror is placed so that 13% of the fluorescence is collected by the lens and focussed onto the photodiode. The concave mirror is placed at the bottom viewport to reflect fluorescence back onto the photodiode. The photodiode (OSD50-E, *Centronics*) was used with a large gain amplifier. This requires it to be shielded from its surroundings so noise is reduced. It is therefore encased in a copper housing and

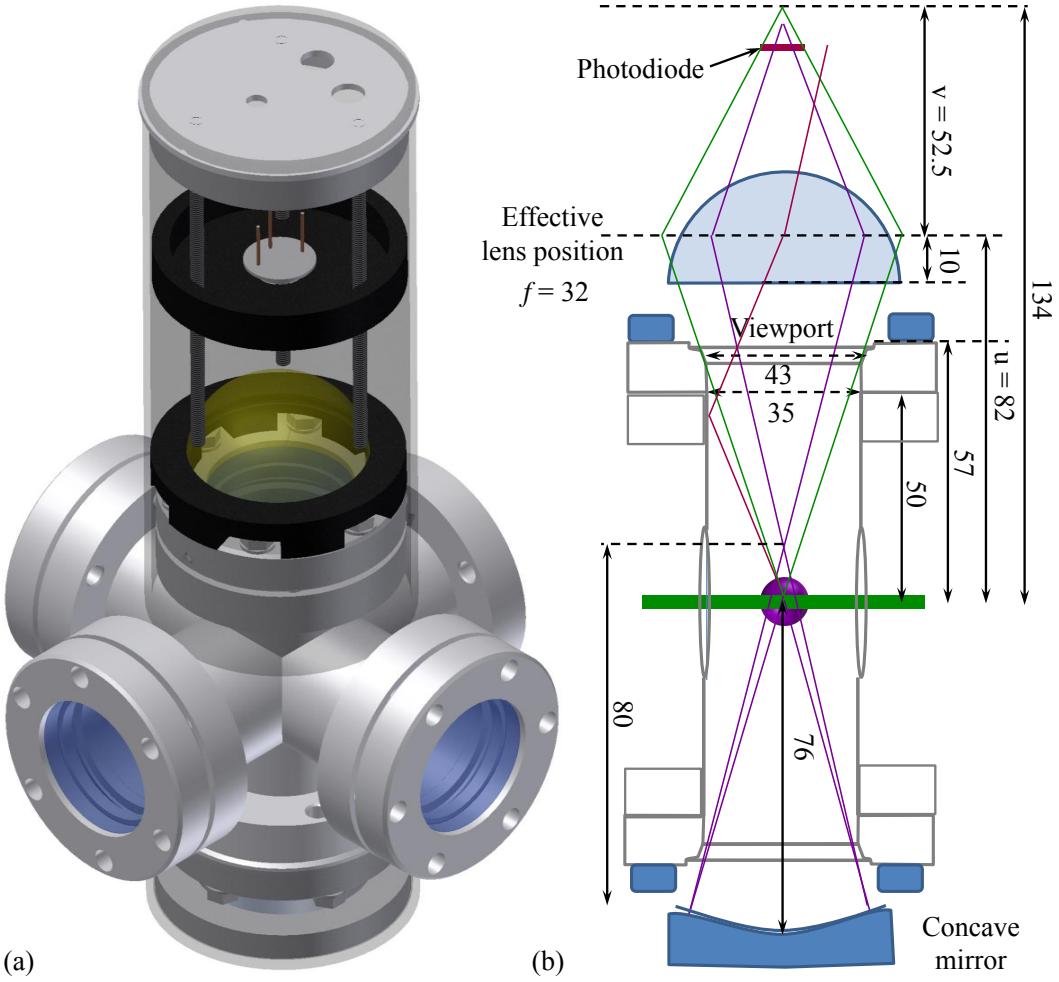

Figure 4.19: Setup for fluorescence spectroscopy (a) The housing of lens and photodiode is designed to fit directly over the viewport to avoid stray light on the photodiode. A mirror is fitted on the bottom viewport to reflect the fluorescence back to the photodiode. (b) The lens and mirror setup captures the light from the largest possible solid angle. The light emitted upwards (green lines) and downward (purple lines) is collected onto the photodiode. Light that will reflect inside the beam machine will miss the photodiode (red line). Dimensions are in mm [1].

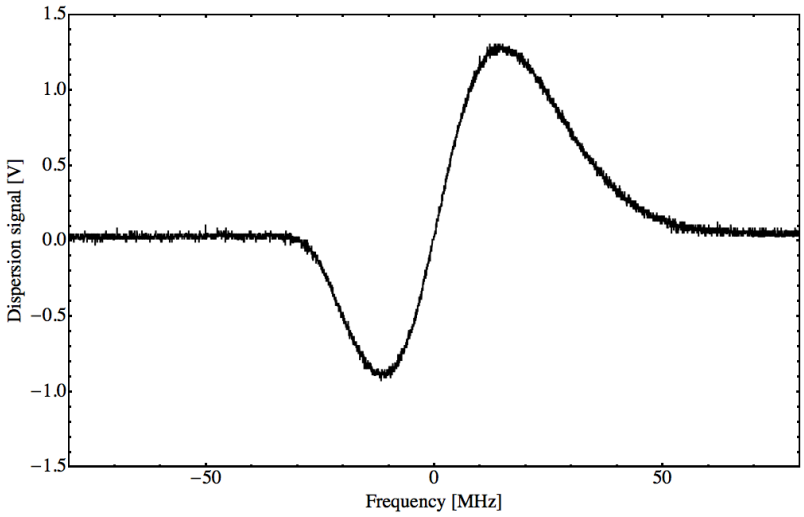

Figure 4.20: The dispersion signal obtained from the Doppler broadened fluorescence peak. The feature has a 25MHz peak-to-peak width.

powered by batteries to avoid the 50 Hz noise from the mains circuit.

We can detect a strong fluorescence spectrum with this setup and can therefore use this to derive an error signal. This is done very similarly to the saturated absorption lock. The fluorescence is modulated at the modulation frequency by the AOM and we extract a dispersion signal in the same way as in the saturated absorption case using a Lock-In amplifier.

We obtain a dispersion signal with 25 MHz peak to peak width as shown in Figure 4.20. The signal is less noisy compared with the FM signal and therefore provides a much more stable error signal. We can find an upper limit for the stability of the laser by locking it and monitoring the noise of the dispersion signal. As we know the gradient of the dispersion signal we can relate this voltage to a frequency. This method can only give an estimate of the performance of the lock as it measures noise in the electronics that does not need to be related to frequency drifts. On the other hand this method might not pick up electronic drifts in the locking equipment. Figure 4.21 shows that the noise of the laser initially decreases with increasing the modulation frequency. As the laser noise plateaus at 3 kHz with about 1 MHz noise, the lock is operated with 3 kHz modulation. Considering we will widen the laser linewidth as described in section 4.2.4 this should be sufficient for the purposes of getting a stable MOT.

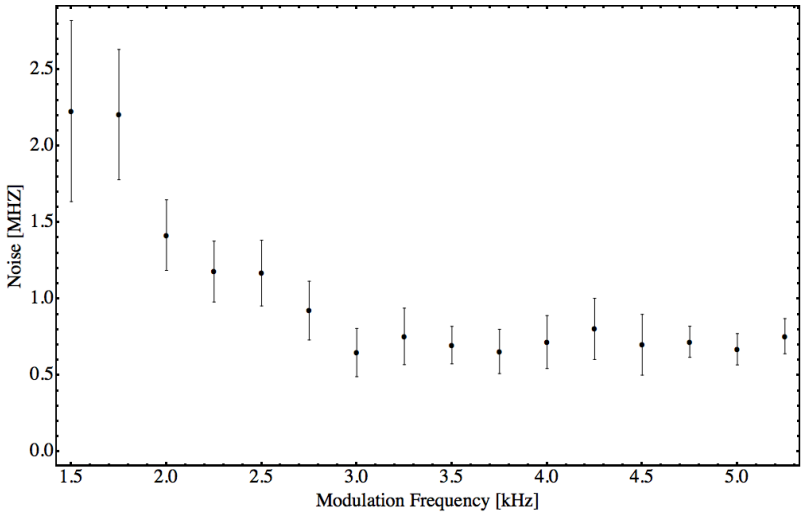

Figure 4.21: Modulation frequency of the AOM against the noise of the dispersion signal. The noise in the dispersion signal was converted into an upper limit of the frequency noise of the laser. The graph plateaus at 3 kHz as the noise on the laser is below that frequency. We can expect less than 1 MHz noise at hight enough modulation frequency.

4.2.4 Frequency Broadening

Sidebands were added to the MOT light by modulating AOM_{12}. This is done to broaden the linewidth of the light, which should improve the capture velocity of the MOT. It will however also lead to a higher Doppler limited temperature in the MOT.

We add a 25 kHz frequency modulation to the Yb MOT AOM using a signal generator (E4421B ESG, *Agilent*). We chose the lowest modulation frequency available by the equipment. This was done to keep the sidebands added close to the carrier frequency, thereby effectively broadening the linewidth. This can be observed in Figure 4.22 (a). The amplitude of the signal determines the number of sidebands added and thereby how much the line is broadened. Figure 4.22 (b) shows that the effective width can be tuned linearly with the modulation amplitude. We can broaden the modulation up to 12 MHz.

4.2.5 MOT, Zeeman Slower and Imaging Optics

The MOT light is transferred via polarisation maintaining fibers to the Science Chamber. The light polarisation is matched to the fast axis of the fiber. The fiber polarisation

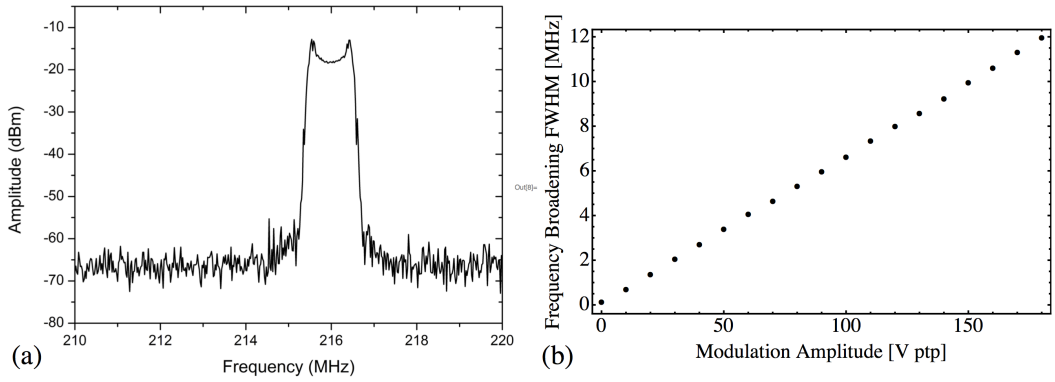

Figure 4.22: Frequency broadening of 556 nm light (a) Frequency spectrum of laser with 60 sidebands separated by 25 kHz. (b) Effective full width half maximum of the broadened laser against the modulation amplitude with 25 kHz sidebands.

can be matched by heating the fiber and monitoring the output polarisation through a polariser. When the fiber is heated the internal birefringence will change if the light is not polarisation matched to the axis. This will cause oscillations in the polarisation when heat is applied to the fiber. We can rotate the fiber and monitor these oscillations until a minimum is found.

The horizontal beams are shown in Figure 4.5. They are retro-reflected and a retro-reflected vertical beam is added to make up the six laser beams that are needed for MOT confinement. The beams are expanded to $1/e^2$ diameter of 24.4 ± 0.2 mm with each beam supplying up to 14.0 ± 0.1 mW power.

The Zeeman slowing beam first needs to be spatially filtered by a 50 μm pinhole to achieve a roughly Gaussian beam profile. This is important as interference fringes will otherwise lead to areas where the atoms will not be slowed by the Zeeman beam. 28% of the power is lost by this spatial filtering. It is then passed through $f = -25$ mm, $f = -100$ mm and $f = 250$ mm lenses (LD2297-A, LD1613-A, LA1301-A, *Thorlabs*) as shown in Figure 4.6. This creates a large beam that is focussed down to $307 \pm 8\,\mu$m at 1.93 ± 0.01 m away from the entrance viewport.

Absorption imaging was attempted with a third *Nichia* diode, which however had to be cooled to a temperature of 3 °C. This led to severe instabilities and frequent mode-hops, which made it challenging to obtain a signal. As no further diodes could be acquired, the imaging light was finally derived from the ECDL laser by shifting the frequency back to resonance with the use of AOMs. As not much light is required for the absorption imaging this was an acceptable solution. For the absorption images in

this work the absorption light was not merged with a MOT beam, but passed through the viewports dedicated for the optical dipole trap. The light was focussed onto a camera (Luca S-856M, *Andor Technology*) using an achromatic lens. A shutter was mounted in front of the camera to avoid exposure from other sources. The absorption beam was switched using one of the AOMs.

We use fluorescence detection to measure the number of atoms in the MOT for both ytterbium and caesium. For this, a lens collects the fluorescence above the main chamber and focusses it onto a photodiode as shown in Figure 4.5. These measurements can be calibrated by using absorption images to obtain an accurate total atom number.

The equation (4.4) needs to be slightly amended to be valid in the case of ytterbium. As bosonic Yb does not have a structure in the ground state the Clebsch-Gordan coefficients $C_1 = C_2 = 1$. The experiment however adds sidebands to the MOT beams to widen them. This significantly affects the detuning δ. As it is difficult to account for the sidebands directly, we simply assume the transition has been widened by some FWHM $\Delta\delta$ around a centre detuning δ. We can integrate over the relevant detunings to adjust for the broadened linewidth. The atom number is therefore given by:

$$N = \frac{16L^2}{d^2}\frac{V_{\mathrm{PD}}}{\mathcal{R}(\lambda)R}\frac{\lambda}{hc}\frac{2}{\Gamma}\frac{4\sqrt{I_s}\sqrt{I+I_s}\Delta\delta}{I\,\Gamma^2\left(-\mathrm{ArcTan}\left[\frac{2\sqrt{I_s}\left(\delta-\frac{\Delta\delta}{2}\right)}{\sqrt{I+I_s}\Gamma}\right]+\mathrm{ArcTan}\left[\frac{2\sqrt{I_s}\left(\delta+\frac{\Delta\delta}{2}\right)}{\sqrt{I+I_s}\Gamma}\right]\right)}. \tag{4.12}$$

This equation was used for all Yb atom number calculations unless otherwise indicated.

Chapter 5

Zeeman Slower

We aim to capture ytterbium atoms directly into a "green MOT" operating on the narrow $^1S_0 \rightarrow {}^3P_1$ transition. As will be discussed in chapter 6 the capture velocity of this MOT is very small and so it is crucial to use a carefully designed Zeeman slower that can deliver a large number of Yb atoms with low enough speed to be captured. The Zeeman slower for Yb operates on the broad $^1S_0 \rightarrow {}^1P_1$ transition at 399 nm. It must also be capable of delivering caesium atoms to the Cs MOT. For Cs, the slower uses the $6\,S_{1/2} \rightarrow 6\,P_{3/2}$ D_2 transition with both hyperfine components present in the light (main cooling and repump).

The first successful Zeeman slowing was done by Phillips and Metcalf in 1981, who slowed Na atoms by 40 % [117]. They exploited the Zeeman shift induced by a magnetic field to compensate the changing Doppler shift as the atoms slowed down so that they remained always in resonance with the counter-propagating laser beam. By refining these methods Prodan *et al.* demonstrated in 1985 that an atomic beam could be brought completely to rest with help of a Zeeman slower [118]. These early Zeeman slowers were usually constructed out of a single coil with the number of layers at each position chosen to give the desired field profile. Since then, various other options to construct a Zeeman slower have emerged. Bell *et al.* have constructed a Zeeman slower using just a single layer of coil [119]. The field profile is created by varying the winding pitch of the coil. The required magnetic field can also be created using a number of permanent magnets [120]. The advantage is that no current sources are needed and the magnets can easily be moved to alter the field profile. However the permanent magnet Zeeman slower cannot easily be turned off, which is desirable in trapping applications. Furthermore there have been a number of dual species Zeeman slowers designed to slow

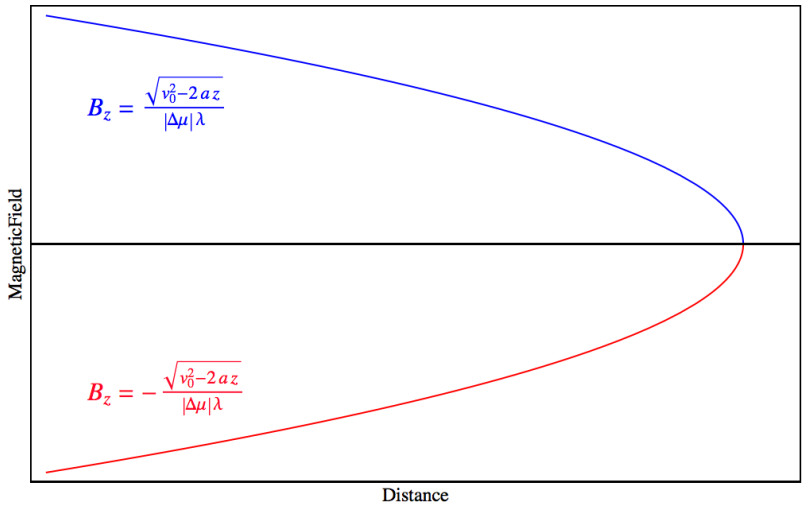

Figure 5.1: The ideal field profile for a Zeeman slower without any offset field. The red curve is used with σ^- light and the blue curve is used with σ^+ light.

two atomic species simultaneously. Okano *et al.* showed that lithium and ytterbium can be slowed simultaneously using the same magnetic field profile [121]. This is due the atomic constants involved leading to similar optimal fields. For most pairs of atoms such a slower is not possible or is very inefficient for one of the two species [122]. A slower built by Marti *et al.* for rubidium and lithium uses a magnetic field split into different stages to decelerate both species [123]. Recently a versatile Zeeman slower was built that can slow different species by switching the magnetic field from one profile to another [124].

In the present work two Zeeman slowers were constructed. One is a slower for ytterbium and lithium using the same magnetic field. It was designed and constructed by Michael Petersen and me at Imperial College London. The second slower uses a switching field to decelerate ytterbium and caesium sequentially. It was designed by Steve Hopkins, Kirsteen Butler, Stefan Kemp and me, and was constructed at Durham University by Stefan Kemp and Kirsteen Butler.

5.1 Basic Physics

A Zeeman slower is a commonly used device to decelerate an atomic beam. This

deceleration is achieved by the atoms scattering photons from a counter-propagating laser beam. Every absorption of a resonant photon will lead to a momentum change of h/λ in the direction of the laser beam, where λ is the wavelength of the photon and h is Planck's constant. The subsequent spontaneous emission will lead to a momentum kick in a random direction. Over many scattering events the random kicks will have no net effect on the mean velocity. The temperature however will rise due to the random momentum kicks [92]. We will discuss the deceleration of a single atom travelling in direction $\hat{z}$ due to the counter-propagating laser beam. The force on the atoms due to the laser is given by Rh/λ, where R is the scattering rate. This scattering rate depends on the intensity I of the laser beam, the linewidth Γ, the saturation intensity I_{sat} of the atomic transition and the detuning δ of the laser beam from the transition. It is given as [92]:

$$R = \frac{I/I_{\text{sat}}}{(2(\omega - \omega_t)/\Gamma)^2 + 1 + I/I_{\text{sat}}} \frac{\Gamma}{2} = \frac{s}{(2\delta/\Gamma)^2 + 1 + s} \frac{\Gamma}{2}\,, \tag{5.1}$$

where ω is the laser light angular frequency and ω_t is the angular frequency of the transition. The remaining symbols are therefore defined as:

$$s = \frac{I}{I_{\text{sat}}}\ ,\ \delta = \omega - \omega_t\,. \tag{5.2}$$

The largest scattering rate is therefore achieved when the laser light is on resonance with the transition $\omega = \omega_t$. However the atom moving towards the beam will see its frequency Doppler shifted by v/λ, where v is the velocity of the atom. The deceleration process will change v and therefore influence the Doppler shift, which will detune the atoms from the light. To counter this detuning a Zeeman slower employs the Zeeman shift produced by a magnetic field to keep the atoms on resonance. The energy shift of the transition between the stretched states due to a magnetic field is given by $\Delta\mu\, B_z = [(g_J M_J)_e - (g_J M_J)_g]\mu_B B_z$. It hence depends on the Lande-g factor g_J and magnetic quantum numbers M_J of the ground state g and excited state e, the Bohr magneton μ_B and the applied external magnetic field B_z. To ensure a closed optical transition we need $(M_J)_e - (M_J)_g = \pm 1$. This means that the transition can be driven with σ^+ or σ^- polarised light, depending on the sign of $\Delta\mu$. If the Zeeman shift varies along the length of the slower in such a way as to compensate for the variation of the Doppler shift as the atom is decelerated, then the atom will be on resonance throughout

the slower, leading to the resonance condition:

$$\frac{\Delta\mu B_z}{h} = \frac{v}{\lambda}\,. \tag{5.3}$$

We can use this equation to calculate the magnetic field, if we know the velocity v of the atom through the Zeeman slower. From equation (5.1) we know that the maximum force is obtained when $\delta = 0$ and $s >> 1$. Hence the maximum acceleration is:

$$a_{\max} = \frac{\Gamma\hbar k}{2M}\,, \tag{5.4}$$

where M is the mass of the atom. However due to the random nature of the emission process and the fact that the laser will never be exactly on resonance or have infinite power, this maximum acceleration cannot be assumed. Hence we assume that the atom experiences a constant deceleration of:

$$a = \eta a_{\max}\,, \tag{5.5}$$

where η is a factor between 0 and 1. This η factor hence determines the acceleration the atoms should experience through the Zeeman slower. We want to design a magnetic field that decelerates the atom almost to rest from an initial velocity v_0 at a constant acceleration. Hence the length of the Zeeman slower is easy to calculate:

$$L_0 = \frac{v_0^2}{2\eta a_{\max}}\,. \tag{5.6}$$

From this equation it becomes apparent that a large η will lead to a short Zeeman slower, but then the atom is required to be always almost perfectly in resonance with an intense laser beam. Any small imperfection in the field would mean it is lost from the slower. When η gets smaller imperfections in the B-field become less critical and the laser beam can be less intense. The length of the Zeeman slower however will increase, which can lead to practical space constraints. Assuming an atom enters the Zeeman slower at the velocity v_0, its velocity through the slower is given by:

$$v(z) = v_0\sqrt{1 - \frac{2az}{v_0^2}}\,. \tag{5.7}$$

By substitution into equation (5.3) a magnetic field profile as a function of the position

along the Zeeman slower is obtained:

$$B_z = \frac{h\sqrt{v_0^2 - 2az}}{\Delta\mu\,\lambda} + B_{\text{offset}}\,. \tag{5.8}$$

B_{offset} is introduced as an offset in the magnetic field to ensure that the Zeeman slower light is not on resonance in the MOT (see Section 5.2). This leads to a magnetic field profile as pictured in Figure 5.1, which will slow all atoms that are travelling slower than the speed v_0 at the start of the slower. This speed is called the capture velocity and should be chosen so that most atoms emerging from the oven can be slowed by the apparatus. In Figure 5.1, B_{offset} is set to zero.

Equation (5.4) illustrates that the ideal Zeeman field is heavily dependent on the properties of the atomic species that is meant to be slowed. In section 5.2 we investigate the relevant species for this thesis and how the required magnetic fields are produced.

5.2 Design

Two different Zeeman slowers were constructed. One was designed to slow lithium and ytterbium simultaneously and the other was designed to slow caesium and ytterbium sequentially. The relevant atomic properties are described in section 2.2. We will explore the differences in design of the two slowers throughout this section.

5.2.1 Length, η and v_0

The most fundamental restriction on our Zeeman slowers was in both cases lab space. We therefore had to design a Zeeman slower with an acceleration a and capture velocity v_0 that would slow a maximum number of atoms and physically fit in the available space. To choose a sensible capture velocity we have to investigate the average speed of an atom emerging from the oven. The velocity distribution along the axis is given by [92]:

$$f(v) = \left(\frac{M}{\sqrt{2}\pi\,k_{\text{B}}\,T}\right)^2 v_z^3 e^{-\frac{Mv_z^2}{2k_{\text{B}}T}}\,, \tag{5.9}$$

where k_{B} is the Boltzmann constant and T the temperature of the oven. The distributions are plotted in Figure 5.2 for Li at 434 °C, Yb at 434 °C and Cs at 83 °C. The temperatures chosen in each case are based on the normal operating oven temperature

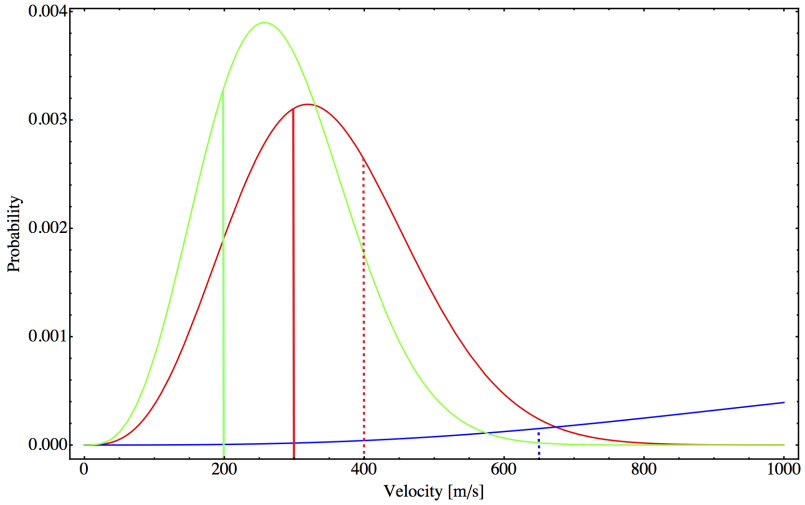

Figure 5.2: Graph shows the speed distribution of atoms in an atomic beam. Green corresponds to caesium at 83 °C, red to ytterbium at 434 °C and blue to lithium at 434 °C. The dotted lines indicate the capture velocities in the lithium/ytterbium slower, while the solid lines indicate the capture velocities in the caesium/ytterbium slower.

of the Durham oven, as they provide an appropriate vapour pressure for operation (see section 3.2.1). We want to pick a capture velocity so a majority of the distribution is slowed, but we are limited by the space and the maximum magnetic field we would need to produce (see equation 5.8). Furthermore for all the above species it is necessary to consider the laser power available on the relevant transition to determine a reasonable η factor.

For the Li-Yb Zeeman slower constructed at Imperial, the length was constrained to roughly 50 cm. For ytterbium we will choose a capture velocity of $v_0 = 400\,\mathrm{m/s}$ decelerated with $\eta = 0.35$. This results in $L_0 = 43.4\,\mathrm{cm}$. The ideal magnetic field for a σ^- slower is shown as the black dotted trace in Figure 5.3. The magnetic field offset will be discussed in detail in section 5.2.2. The same ideal magnetic field is obtained for a lithium slower with $\eta = 0.31$ and $v_0 = 650\,\mathrm{m/s}$. Producing this field profile with magnetic field coils should therefore enable us to slow both atomic species simultaneously. That a slower like this can work was demonstrated by Okano *et al.* [121].

The optimal magnetic field profile depends on the mass, wavelength and linewidth of the species involved [122]. For Cs and Yb the ideal magnetic field profiles are too different to efficiently slow both. We therefore want to construct a slower that can pro-

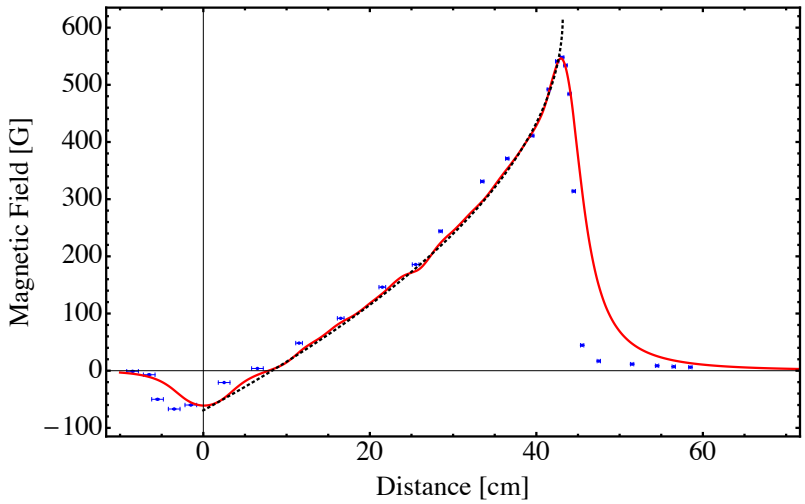

Figure 5.3: Magnetic field profile of the lithium/ytterbium Zeeman slower. The atoms originate at $z = -10\,\text{cm}$. The Zeeman slower starts at $z = 0\,\text{cm}$ and the MOT is located at $z = 60\,\text{cm}$. The black dotted line shows the ideal magnetic field according to equation (5.8) and the values outlined in Table 5.1. The red line shows the simulated magnetic field according to the windings and currents outlined in Table 5.3. The blue data points show the measured field of the Zeeman slower. The discrepancies between simulated and measured field are explained in the text.

	η	v_0 (m/s)	L_0 (cm)	B_{offset} (G)	B_{end} (G)	$\delta/2\pi$ (MHz)
Yb	0.35	400	43.4	620.4	546.6	869
Li	0.31	650	43.4	620.4	546.6	869

Table 5.1: Design parameters for Li-Yb Zeeman slower.

	η	v_0 (m/s)	L_0 (cm)	B_{offset} (G)	B_{end} (G)	$\delta/2\pi$ (MHz)
Yb	0.128	300	70	435	378	609
Cs	0.5	200	70	41.8	13.1	378

Table 5.2: Design parameters for Cs-Yb Zeeman slower.

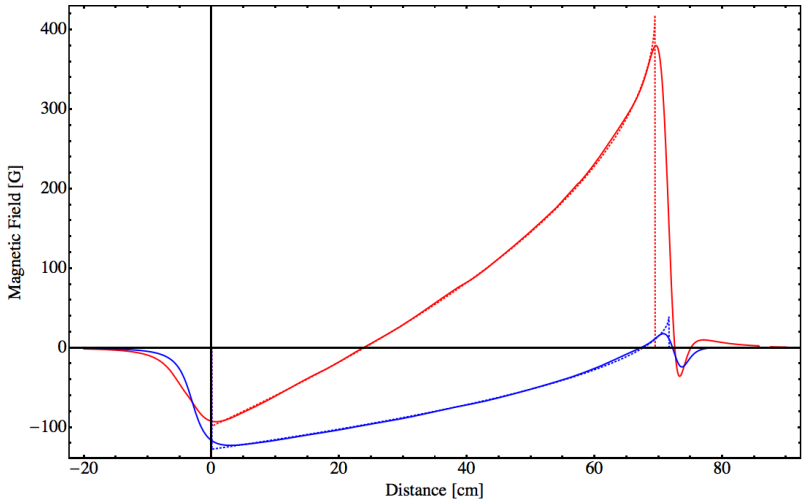

Figure 5.4: Magnetic field profiles of the Cs-Yb Zeeman slower. The atoms originate at $z = -20\,\text{cm}$. The Zeeman slower starts at $z = 0\,\text{cm}$ and the MOT is located at $z = 75\,\text{cm}$. The red dotted line shows the ideal magnetic field for ytterbium and the red solid line show the measured profile. The blue dotted line shows the ideal field for caesium and the blue solid line corresponds to the measured field.

duce two different profiles with the same coils but different currents. Caesium requires a longer slower than ytterbium as smaller line width leads to a smaller maximum acceleration. Considering the lab space in Durham we built a 70 cm long slower. The space constraint requires a high efficiency Zeeman slower with $\eta = 0.5$ and $v_0 = 200\,\text{m/s}$ for Cs. As can be seen in Figure 5.2 this capture velocity should allow us to slow a significant portion of the beam. Due to the higher scattering rate of ytterbium we can choose a low $\eta = 0.128$ for the ytterbium Zeeman slower. This should lead to a high efficiency as a smaller scattering rate is required. Choosing this value gives a capture velocity of 300 m/s, which again slows a significant portion of the beam. We obtain two ideal magnetic field curves that are shown in Figure 5.4.

5.2.2 Magnetic Field Offset

As can be seen in Figures 5.3 and 5.4 the magnetic field at the end of each Zeeman slower is not zero, but has an offset B_{offset} as introduced in equation (5.8). There are several reasons why this offset is necessary.

We discussed in section 2.2.2 that the Yb $^1S_0 \rightarrow {}^1P_1$ transition used for the Zeeman slower is not completely closed, but can decay to the ^3D states with a branching ratio B_{D}. We therefore want to ensure that the laser beam for the Zeeman slower, which has to intersect with the trapping region, does not excite trapped atoms. The rate at which atoms will escape the cooling cycle due to this loss is given by $R \times B_{\text{D}}$, where R is the scattering rate in the MOT from the Zeeman slower beam. Just considering this loss mechanism the trap lifetime τ will be limited to $R\,B_{\text{D}} = 1/\tau$. Using equation (5.1), we can rearrange for the detuning of the laser:

$$\sqrt{B_{\text{D}}\,\tau\,s\left(\frac{\Gamma}{2}\right)^3 - \left(\frac{\Gamma}{2}\right)^2 - s\left(\frac{\Gamma}{2}\right)^2} < |\omega - \omega_t| = |\delta|\,. \tag{5.10}$$

If we assume $s = 4$ for an upper limit of the Zeeman laser beam, we would obtain a lifetime $\tau = 0.13\,\text{s}$ if the Zeeman light is on resonance in the MOT. We can however detune the Zeeman light and compensate by offsetting the magnetic field. We want to choose a large detuning for ytterbium to ensure that the lifetime of our MOT is not limited to loss to the ^3D states. For the Li-Yb Zeeman slower we have chosen a detuning of $\omega - \omega_t = -2\pi \times 875\,\text{MHz}$, which gives us the limit $\tau = 100\,\text{s}$. At this detuning we therefore expect the lifetime to be limited by background gas collisions rather than by loss to the ^3D states. The magnetic field needed to cancel out the detuning is given by:

$$\omega - \omega_t = -\frac{\mu_B B_{\text{offset}}}{\hbar}\,. \tag{5.11}$$

Therefore an offset field $B_{\text{offset}} = 620.4\,\text{G}$ is needed.

We have the same problem in the Cs-Yb Zeeman slower. However due to some geometric constraints of the slower (see section 5.2.3) we are limited by the maximum current we can pass through the last coils. We can apply an offset field of 378 G, which will mean the laser can be $2\pi \times 609\,\text{MHz}$ detuned. Considering the limit $s = 4$ we obtain the limit $\tau < 48\,\text{s}$, which is enough for any application of this apparatus. The offset of the Cs profile is set to 13.1 G. Cs does not require such a large offset as repump lasers are used to keep the atoms in the cooling cycle.

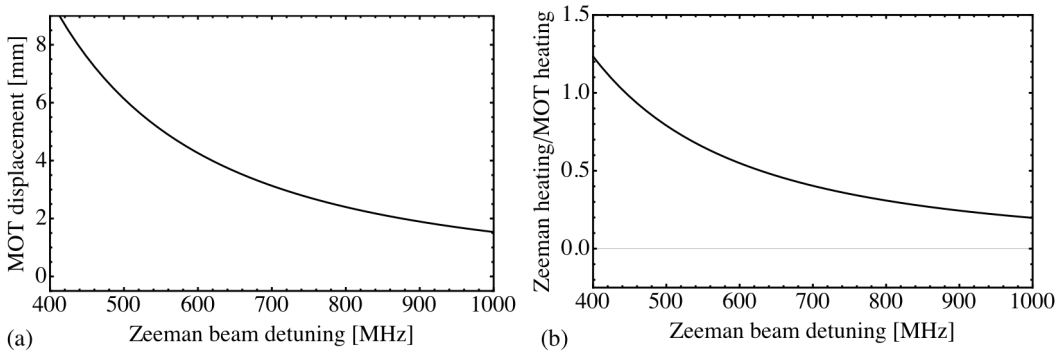

Figure 5.5: Influence of the Zeeman slowing beam on the ytterbium MOT. The typical parameters for MOT and Zeeman operation were estimated: $s_{\mathrm{Z}} = 0.2$, $s_{\mathrm{M}} = 30$, $\delta_{\mathrm{M}} = 2\pi \times 5\,\mathrm{MHz}$ (a) The displacement of the MOT due to the Zeeman slowing beam against the detuning of the Zeeman slowing beam. (b) The ratio of the Zeeman heating rate over the MOT heating rate against the detuning of the Zeeman beam.

The second reason why a magnetic field offset is necessary becomes apparent when considering what happens at the end of a Zeeman slower. If we used a Zeeman slower with no magnetic offset, the atoms would be slowed to 0 m/s as outlined in section 5.1. However the atoms will still be in the path of the laser beam and on resonance with the beam. Therefore all the atoms will be turned around inside the slower. We need the atoms to leave the Zeeman slower with a small, but positive velocity, and so we need to make sure that when the atoms reach their target velocity they are quickly detuned from the laser beam. This is achieved most easily by rapidly changing the magnetic field. As shown in Figures 5.3 and 5.4 the measured field does not follow the ideal field to the end. Furthermore in both slowers the field is terminated over the shortest distance possible (see section 5.2.3). This distance can be kept short if the magnetic field at the end of the slower B_{end} is high. As the Cs MOT has a high capture velocity the final velocity of Cs atoms from the Zeeman slower is less critical. For ytterbium however the low capture velocity requires a very sharp magnetic field cut-off. We choose B_{end} to be 378 G for the Durham slower and 546 G for the Imperial slower. The exact point where the field needs to be terminated was determined by using the numerical simulation outlined in section 5.3.

Additionally, as the Zeeman beam passes through the MOT region, it will affect the MOT. Especially for ytterbium the Zeeman slowing beam can exert a significant pushing force on the atoms in the MOT, which will effectively displace the MOT. We

will derive the position dependent force (equation (6.8)) of the MOT in section 6.1.2. By equating this to the pushing of the Zeeman beam an equilibrium position of the MOT can be computed:

$$z_{\mathrm{MOT}} = \frac{h\, s_{\mathrm{Z}}\, \Gamma_{\mathrm{Z}}\, \Gamma_{\mathrm{M}}\, \lambda_{\mathrm{M}}\, (1 + s_{\mathrm{M}} + 4\, \delta_{\mathrm{M}}^2/\Gamma_{\mathrm{M}}^2)^2}{32\, \mu_{\mathrm{B}}\, B'\, \pi\, s_{\mathrm{M}}\, \delta_{\mathrm{M}}\, \lambda_{\mathrm{Z}}\, (1 + s_{\mathrm{Z}} + 4\, \delta_{\mathrm{Z}}^2/\Gamma_{\mathrm{Z}}^2)}\,. \tag{5.12}$$

The subscripts M and Z denote the MOT beams and the Zeeman slower beam respectively and B' is the magnetic field gradient of the MOT. Using the Zeeman and MOT beam parameters that were used in the experiment, outlined in section 4.2.5, Figure 5.5 (a) is obtained. It shows that the push of the Zeeman slower decreases when increasing the Zeeman beam detuning. It predicts a displacement of roughly 4 mm at a detuning of 600 MHz. We therefore expect to see visible push from the Zeeman beam in the Durham MOT. We can also compare the heating rate of the MOT and the Zeeman slower by forming a ratio:

$$\frac{\text{Zeeman slower heating rate}}{\text{MOT heating rate}} = \frac{(h/\lambda_{\mathrm{Z}})^2\, R_{\mathrm{Z}}}{(h/\lambda_{\mathrm{M}})^2 R_{\mathrm{M}}}\,. \tag{5.13}$$

Figure 5.5 (b) shows this ratio as function of the Zeeman beam detuning. Similarly to the pushing the heating of the Zeeman slower is more significant at lower detunings. At 600 MHz we expect a ratio of 0.55. The temperature of the MOT should therefore be affected by the Zeeman slowing beam. Both of these effects show that it will be important to block the Zeeman slowing beam after enough atoms have been loaded.

5.2.3 Magnetic Field

In both Zeeman slowers the magnetic field is produced by coils wrapped around a small diameter tube. We wrap multiple coils so that we can use different currents and use them to tune the required magnetic field profile. To calculate the entire magnetic field we have to consider the magnetic field of a single coil at position z_c and radius r_c carrying a current I. The longitudinal field B_z and the transverse field B_r are given by the formulas:

Coil	Position (cm)	Length (cm)	Turns	Layers	Simulated Currents (A)	Measured Currents (A)
1	-3	6.3	15	15	-2.22	-2.2
Gap 1	3.3	7.4				
2	10.4	3.4	8	2	7.00	6.96
3	14.1	3.4	8	4	7.00	6.96
4	17.8	3.4	8	5	7.00	6.96
5	21.5	3.4	8	9	7.00	6.96
Gap 2	25.2	1.1				
6	26.6	3.4	8	12	7.00	6.96
7	30.3	3.4	8	12	7.00	6.96
8	34.0	3.4	8	15	7.00	6.96
9	37.7	3.4	8	35	8.04	8.02
Gap 3	41.4	1.1				
10	42.4	2.1	6	10	40.0	34.0

Table 5.3: The positions, lengths and currents of the coils making up the Li-Yb Zeeman slower. Each coil is wound using rectangular wire, 4.2 mm wide and 2.7 mm high. The simulated and measured currents are used to obtain the traces in Figure 5.3.

$$B_z = I \times \frac{\mu_0}{2\pi\, r} \frac{1}{\sqrt{(r+r_c)^2+(z-z_c)^2}} \times \left(\text{EllipticK}\left[\frac{4\, r_c\, r}{(r+r_c)^2+(z-z_c)^2}\right] + \left(\frac{r_c^2+r^2-(z-z_c)^2}{(r_c-r)^2+(z-z_0)^2} \times \text{EllipticE}\left[\frac{4\, r_c\, r}{(r+r_c)^2+(z-z_c)^2}\right]\right)\right), \quad (5.14)$$

$$B_r = I \times \frac{\mu_0}{2\pi} \frac{z-z_c}{\sqrt{(r+r_c)^2+(z-z_c)^2}} \times \left(-\text{EllipticK}\left[\frac{4\, r_c\, r}{(r+r_c)^2+(z-z_c)^2}\right] + \left(\frac{r_c^2+r^2-(z-z_c)^2}{(r_c-r)^2+(z-z_0)^2} \times \text{EllipticE}\left[\frac{4\, r_c\, r}{(r+r_c)^2+(z-z_c)^2}\right]\right)\right), \quad (5.15)$$

where EllipticK and EllipticE are the complete elliptic integrals of the first and second kind, and z and r are the axial and radial coordinates. These equations can be added up for all wire loops in the arrangement to find the total magnetic field profile of the slower.

For the Li-Yb slower we chose to wind 10 independent coils (see Figure 5.6). This design provided a lot of flexibility to fine-tune the final magnetic field profile. We

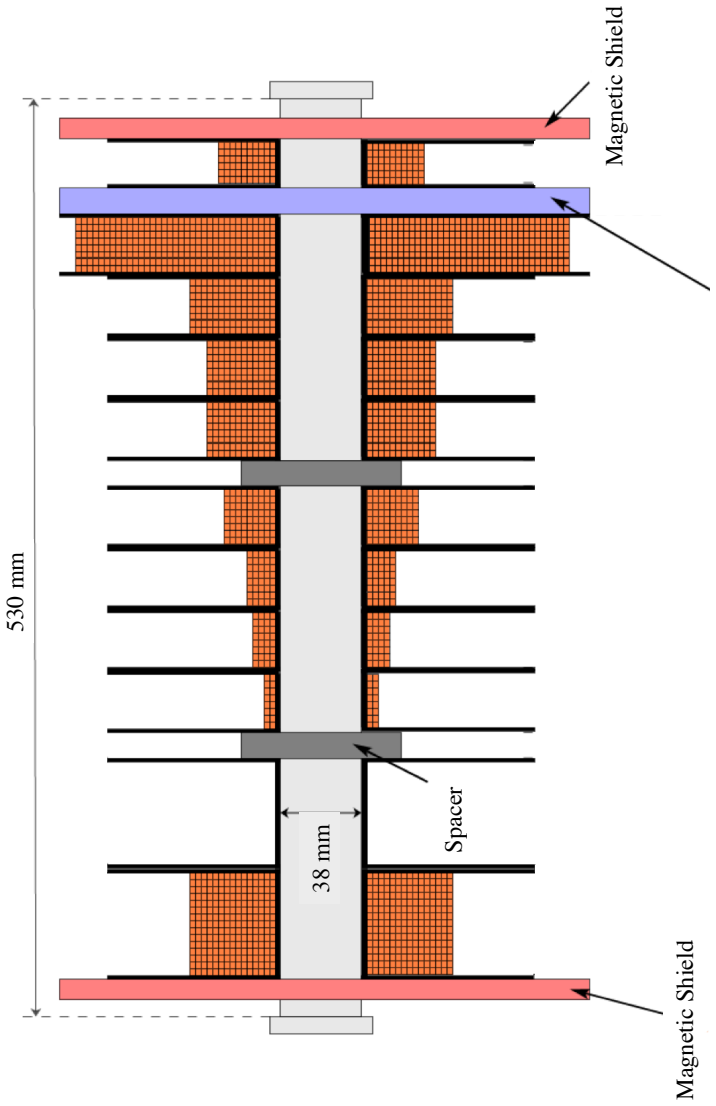

Figure 5.6: Schematic coil arrangement of the Li-Yb Zeeman slower. Ten coils are used to create the magnetic fields. Magnetic shields are used to terminate the magnetic field in the shortest distance.

Coil	Cs Currents [A]		Yb currents [A]	
	Design	Optimised	Design	Optimised
Solenoid	-18.85	-19.65	38.1	36.5
1	-1.25	-1.235	-4	-3.82
2	1.25	1.235	4	3.82
3	33.6	27.98	149	141.4
4	-26.9	-23.02	-116.5	-109.2

Table 5.4: The designed and optimised currents for the Cs-Yb Zeeman slower.

could change the exact position of each coil as well as the current flowing through each. To ensure that this design could produce a satisfactory magnetic field profile we simulated the coils using *MATHEMATICA* to find the currents required through each coil to match the ideal field as closely as possible (see Table 5.3). From the simulated trace in Figure 5.3 we can see that we are expecting some small discrepancies between the ideal field and the real field. These discrepancies will lead to small changes in the acceleration in that section and should not affect the performance of the slower as we will see in the section 5.3.2 where simulations of the slower are discussed. In the final design of the Zeeman slower we added two magnetic shields to ensure a sharper magnetic field drop-off and avoid the field from the Zeeman slower leaking into the trapping region. Furthermore we required a water cooling jacket in-between coils 9 and 10 to reduce the temperature. By measuring the field with a Hall probe, we could adjust the currents to find the best fit to our simulations. The currents we used are outlined in Table 5.3 and the measured field is shown in Figure 5.3. The curve does not match around the origin because the coils could not be compressed to the original designed length. The rest of the measured points lie slightly higher than the simulated curve, but overall show good agreement. Furthermore we measure sharper field drop offs at the end due to the magnetic shields, that were not simulated. The measured field was used in the numerical simulation to ensure we could expect a satisfactory performance (see section 5.3).

For the Cs-Yb Zeeman slower we chose an arrangement of five coils (see Figure 5.7). A solenoid is wound the whole length of the Zeeman slower and serves mainly the purpose of controlling the offset field and thereby the required laser detuning δ. Coils 1 & 2 are wound on top of the solenoid and create the bulk of the Zeeman slower field. The coils were wound separately as they need the current supplied in opposing directions. This ensures that the profile crosses through 0 G (see Figure 5.4). By

Coil 1

Layer	1	2	3	4	5	6	7	8	9	10	11	12	13	14	15	16
Turns	153	147	135	126	117	108	96	84	75	61	50	40	27	20	10	10

Coil 2

Layer	1	2	3	4	5	6	7	8	9	10	11	12	13
Turns	77	69	62	55	48	42	36	31	28	24	20	17	15

Coil 3

Layer	1	2	3
Turns	3	3	3

Coil 4

Layer	1	2
Turns	4	4

Solenoid

Layer	1
Turns	183

Coils 1 and 2 wound with 3×1 mm wire
Coils 3 and 4 wound with 3.4×3.4 mm wire
Solenoid wound with 4.3×4.3 mm wire

Figure 5.7: Schematic coil arrangement of the Cs-Yb Zeeman slower. Coils 1 & 2 are shown in purple, Coil 3 & 4 are green and the solenoid is red. The tables outline the number of turns for each layer and the wire used in each coil (see also [1]).

including this zero crossing we keep the overall field smaller and therefore reduce the currents and coil windings required. Coil 3 & 4 are used to create the large magnetic field and sharp cut-off at the end of the slower. By running two coils with opposite currents close to each other we gain fine control over the exact maximum field and the sharp cut off. This is important as it tunes the exact velocity of the atoms exiting the Zeeman slower, which will directly relate to loading rate of the MOT. As no magnetic shield was implemented in this design, we need to use a combination of shim and compensation coils to cancel the magnetic field from the Zeeman slower in the MOT region. The exact positions of these coils is outlined in section 6.2. We again used a Hall probe to match the desired field as closely as possible and the measurements are shown in Figure 5.4. As discussed before any deviation from the ideal field will simply result in a small change of the acceleration in that section. The maximum field of the slower is again cut short to avoid turning atoms around inside the slower.

5.3 Numerical Simulation

In collaboration with Mike Tarbutt, I constructed a numerical simulation in *MATHEMATICA* to simulate the evolution of the atoms through the Zeeman slower. This was done to find the optimum design for the slowers and to investigate the important parameters we can manipulate. The following section discusses the simulation and the results that can be drawn from them. The code of the program can be found in Appendix A.

5.3.1 Simulation Code

The simulation tries to follow the basic physics principles of the Zeeman slower as closely as possible. The program takes the measured magnetic field as an input. It assumes a Gaussian laser beam and requires as input the position of the waist with respect to the beginning of the slower z_w and the Rayleigh range z_0 of the laser beam. We create an initial atom distribution emerging from a small aperture based on the Maxwell-Boltzmann distribution (see equation 5.9). We calculate every atom individually as it travels through the slower. We do this by evaluating the change in position $\overrightarrow{r}$ and velocity $\overrightarrow{v}$ of every atom over a small time step δt. The average number of scattering events per atom and time step is given by $R\,\delta t$. The scattering rate R can be calculated using equation (5.1) with the appropriate s for the position of the atom in

the beam. The actual number of scattering events in any time step is random, therefore we pick a random number n from a Poisson distribution with an average $R\,\delta t$ for each time step. Each of these scattering events will consist of an absorption and emission event that will lead to a momentum kick. We will start by discussing the momentum kick due to the absorptions. These absorption events are in the direction the photon is travelling, which will depend on the position of the atom in the laser beam. The velocity changes due to the absorption is given as:

$$\overrightarrow{\Delta v_{\text{Absorption}}} = -\frac{nh}{M\lambda}\begin{pmatrix} x/\rho \\ y/\rho \\ \sqrt{\left(1-\left(x^2+y^2\right)\right)/\rho^2} \end{pmatrix}, \tag{5.16}$$

where x, y and z define the position of the atom at the beginning of the time step and ρ is the radius of curvature of the laser beam at that position. It is given by:

$$\rho = (z+z_w)\left(1+\left(\frac{z_0}{z+z_w}\right)^2\right). \tag{5.17}$$

We also need to consider the spontaneous emission event, which will result in a momentum kick in a random isotropic direction. The resulting velocity change due to one photon k is:

$$\left(\overrightarrow{\Delta v_{\text{Emission}}}\right)_k = \frac{h}{M\,\lambda}\begin{pmatrix} \sin\theta\cos\phi \\ \sin\theta\sin\phi \\ \cos\theta \end{pmatrix}, \tag{5.18}$$

where ϕ is selected from a uniform distribution between 0 and 2π and θ is selected from a sin distribution between 0 and π to ensure uniform distribution around a sphere. We can compute the overall velocity change due to emission by summing over all scattering events:

$$\overrightarrow{\Delta v_{\text{Emission}}} = \sum_k^n \left(\overrightarrow{\Delta v_{\text{Emission}}}\right)_k. \tag{5.19}$$

We can therefore construct a recursive formula for the velocity of the atom after the i^{th} time step:

$$\overrightarrow{v_i} = \overrightarrow{v_{i-1}} + \overrightarrow{v_{\text{Absorption}}} + \overrightarrow{v_{\text{Emission}}} + \begin{pmatrix} -g\,\delta t \\ 0 \\ 0 \end{pmatrix}. \tag{5.20}$$

where g is the acceleration due to gravity which is simulated in the x direction. The new position of the atom is computed from the previous position and velocity:

$$\overrightarrow{r_i} = \overrightarrow{r_{i-1}} + \overrightarrow{v_{i-1}}\,\delta t\,. \tag{5.21}$$

Using the formulas we can calculate the position and velocity of an atom after every time step. The main interest of the simulations are the velocity and position spread of the atoms after leaving the Zeeman slower. We therefore need to run the simulation over enough time steps so that all atoms have left the slower.

By going through these equations for every atom in the simulation we can record how an atom travels through the slower. From that we can draw conclusions on the various parameters that control the Zeeman slower, such as the magnetic field profile and the laser detuning, power and beam shape. We therefore used this simulation to get reasonable estimates for both Zeeman slowers.

5.3.2 Simulation Results

This section focuses on the results for ytterbium of the Cs-Yb slower. The conclusions also apply to Li-Yb slower. We omit Cs from this discussion as it is easier to slow and trap.

For all the simulations below we used the magnetic fields we expect when using the optimised currents given in Table 5.4. The atoms originate on the z-axis at $z = -0.3\,\mathrm{m}$, with axial velocity distributed according to a Maxwell-Boltzmann distribution. The transverse velocity is zero. The laser beam of the experiment is described in section 4.2.5. We use a Gaussian beam for the simulation that resembles the actual beam as closely as possible.

We will first discuss the results that can be obtained from a single run of the simulation. The movement of the atoms in a single run are shown in Figure 5.8 (a). Atoms faster than 300 m/s are not slowed and travel straight through the slower. Most atoms are slowed slightly as the magnetic field is ramped up. Then they travel through the slower at constant velocity until they are in resonance with the laser beam. From this point all atoms follow the same trajectory to the end of the slower. Atoms can drop out of the Zeeman slower prematurely because, by chance, they do not undergo enough scattering events. Atoms that travel to the end of the Zeeman slower can

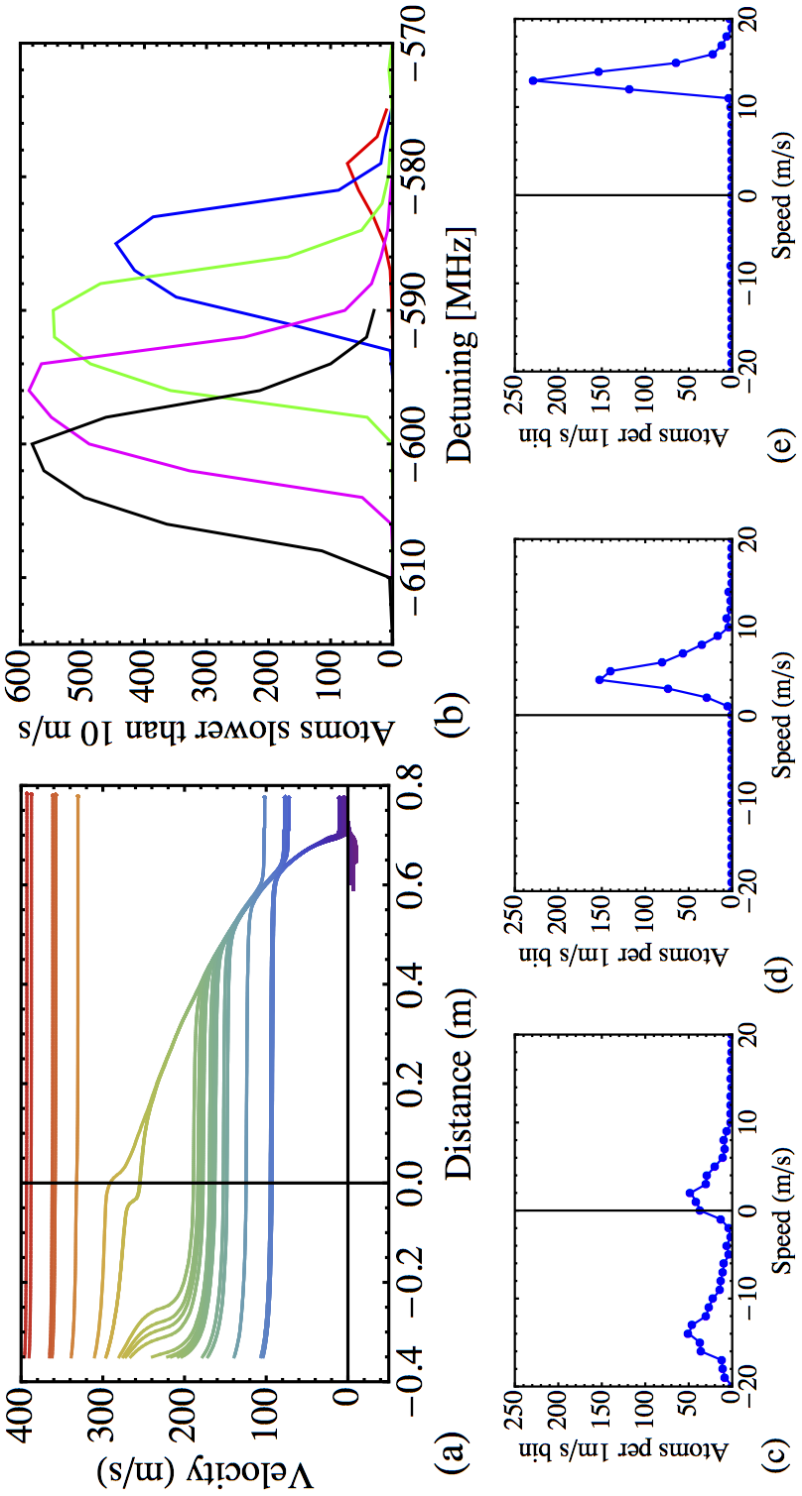

Figure 5.8: Results of the numerical simulations (a)Trajectories of atoms travelling through the Zeeman slower, showing the velocities of several atoms as they travel through the slower. (b) Number of atoms travelling slower than 10 m/s at the end of the slower against the laser detuning used for the simulation. The different curves are simulations with different laser power: Black = 50 mW, Magenta = 40 mW, Green = 30 mW, Blue = 25 mW, Red = 22 mW. (c)-(e) Final velocity distribution of simulations with 1000 atoms and different laser detuning: (c) - 592 MHz (d) - 596 MHz (e) -608 MHz.

receive too many scattering events and be turned around. Only the atoms that are ejected from the slower at a small positive velocity can be captured inside the MOT. The final velocity of the atoms can be controlled by a number of parameters.

We are mainly interested in this final velocity. Figure 5.8 (c)-(e) show the final velocity distributions of simulations with 1000 atoms and 40 mW of laser power. Realistically we can only trap atoms that are travelling slower than 10 m/s (see chapter 6). The three graphs show that we can control the final velocity distribution by changing the detuning of the laser. If the laser is too far detuned, -608 MHz (Figure 5.8 (e)), the atoms will leave the Zeeman slower at velocities larger than 10 m/s. Those atoms can therefore not be trapped. With too little detuning, -592 MHz, some of the atoms will undergo too many scattering events and are turned around inside the slower. Figure 5.8 (c) shows that the final velocity distribution is split. This splitting is due to the end conditions of the simulation. The simulation will run for a long time to ensure that all atoms have passed through the Zeeman slower. It stops when an atoms passes through the MOT region. However atoms that are slowed down to 0 m/s will not pass through the MOT region and will therefore be simulated for a longer time. Therefore it is likely that a few scattering events will eventually turn them around. In practice we expect atoms that reach 0 m/s to drop under gravity and therefore collide with the walls. The optimum trapping is expected when most atoms exit the slower between 0 and 10 m/s at a detuning of -596 MHz (Figure 5.8 (d)).

This behaviour can be explored further by running several simulations and changing the detuning. Figure 5.8 (b) shows the number of atoms travelling slower than 10 m/s for different powers and detunings. We observe that the optimum power and detuning are interlinked giving each curve a maximum at different detunings. More power will lead to more off-resonant scattering at the end of the slower, which increases the chance of turning atoms around. Therefore higher powers will have an optimum at larger detuning. There is a sharp cut-off in the power required to slow atoms effectively. The graph shows that hardly any atoms are slowed at 22 mW, but this rapidly increases at 25 and 30 mW. The slower will need a minimum power, which is controlled by the η factor we chose earlier. Therefore if the power drops below a certain threshold the atoms will drop out of the Zeeman slower before the end. However increasing the power above 40 mW will not lead to a significant gain in slowed atoms. The power is sufficient to eliminate almost all early drop outs and therefore a power increase will not improve the trap. The curves have a FWHM of around 15 MHz.

From these simulations we can gain a clear insight into the workings of the Zeeman slower. The results above will be compared to the experimental results outlined in section 5.4.

5.4 Experimental Results

5.4.1 Ytterbium

All results discussed here will be in terms of total atom number in the MOT. The ytterbium experiments all follow the same experimental procedures. The MOT (described in chapter 6) is loaded for 3 s and the maximum fluorescence is recorded with the photodiode. This is repeated 8 to 15 times to obtain an error estimate on the measurement. The output voltage from the fluorescence photodiode is then converted into an actual atom number as outlined in section 4.2.5. We did not conduct any experiments on the final velocity distribution of the atoms exiting the Zeeman slower. When investigating the Zeeman slower by studying the MOT we have to ensure that the MOT is not affected by other effects unrelated to the Zeeman slower. Most notably we observed that the MOT position changed with varying the laser power and detuning of the Zeeman slowing laser, as well as the final magnetic field of the slower. For all experiments below we tried to ensure that the MOT was in the centre of the Science Chamber. Furthermore we should note that the optimum configuration was only found for certain MOT parameters. While in general we expect the MOT and Zeeman slower to work independently, we did not explore a possible connection of their parameters.

We will explore the results for slowing ytterbium first. For all the Yb experiments the MOT was run with a field gradient of $3.66\,\mathrm{G\,cm^{-1}}$. The MOT light was red detuned by 5 MHz and the FWHM of the sidebands was 3.35 MHz (see chapter 6 for an explanation of these parameters). All results are shown for ^{174}Yb. We have also trapped ^{172}Yb and ^{176}Yb, but have not found any differences in Zeeman slowing behaviour.

The first step in optimising the Zeeman slower was optimising the magnetic field coils. For these experiments the Zeeman beam was run at 69 mW power and -589 MHz detuning. The coils cannot be optimised independently because changing one coil will change the optimum of the other coils. For this process we brought all coils close to the optimum we could find. After that we varied the currents in each coil individually. A more thorough investigation of the dependencies of the coils could lead to improvements in the Zeeman slower. Figure 5.9 shows that clear optima for all the coils can be found.

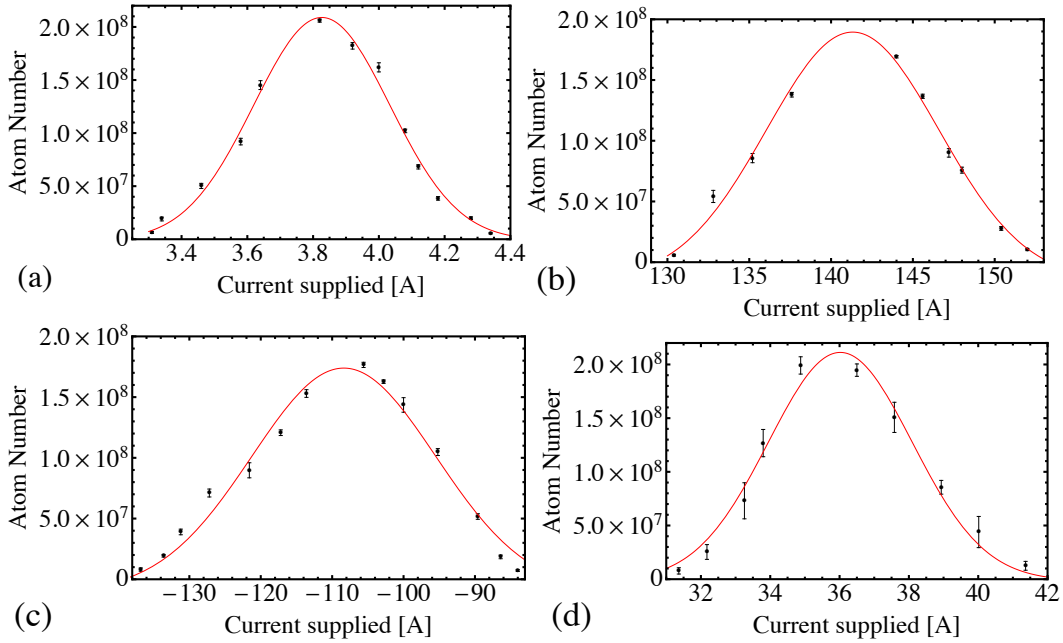

Figure 5.9: Zeeman coil optimisation for ytterbium. The graphs show the 3 s MOT load atom number against the supplied current of the different Zeeman coils: (a) Coil 1 & 2 (b) Coil 3 (c) Coil 4 (d) Solenoid. The lines show the best Gaussian fit.

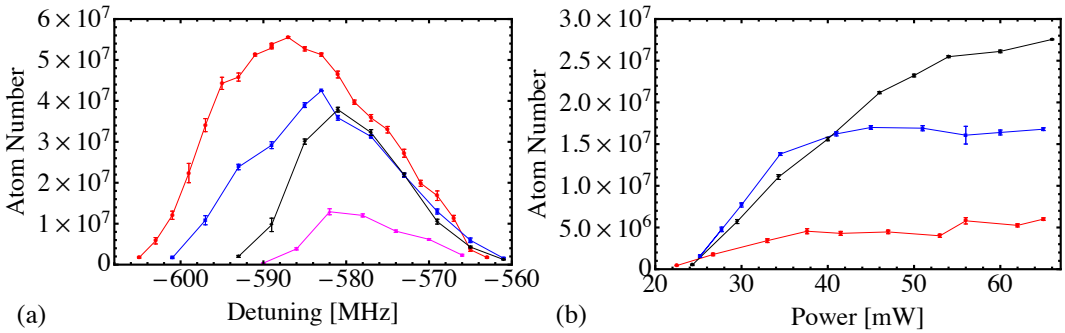

Figure 5.10: Zeeman slower data obtained by loading a MOT for 3 s and recording the atom number. (a) Data for varying the Zeeman light detuning with different overall powers: Red = 69 mW, Blue = 60.5 mW, Black = 37.5 mW, Magenta = 35 mW (b) Data for varying power of Zeeman light with different detunings: Red = -573 MHz , Blue = -580 MHz , Black = -589 MHz. Lines are included as a guide to eye.

Coils 1 & 2 (Figure 5.9 (a)) create the bulk of the Zeeman slowing field. The optimum is found at 3.82 ± 0.01 A, which is 5 % smaller than the design value of 4 A. Coil 3 (Figure 5.9 (c)) creates the large field required at the end of the slower. Its optimum current is at 141.4 ± 0.1, which is also 5 % smaller than the design parameter of 149 A. Coil 4 (Figure 5.9 (d)) creates the sharp field drop off. It is optimised at -109.2 ± 0.4 A, the magnitude of which is 6 % small than the design current of -116.5 A. These differences maybe due to imperfections in the winding of the coil or field distortions due to the MOT or Shim coils. The differences could also be due to a systematic calibration error in the ammeter used to measure the currents. The solenoid current is closely linked to the laser detuning, therefore the above graph only optimises the coil for the specific detuning used. The best value for the given detuning was found at 36.5 ± 0.1 A, which is 4 % smaller than the design parameter of 38.1 A. The optimum coil parameters are outlined in Table 5.4.

The optimum power and detuning of the Zeeman slower are closely interlinked as observed in the numerical simulation (section 5.3). Therefore in order to optimise the Zeeman slower we run two different experiments. Figure 5.10 (a) shows curves with varying detuning, but fixed power. Figure 5.10 (b) shows curves with changing power and constant detuning. We find a good agreement between these measurements and the numerical simulations. We observe that with more power a larger detuning leads to the optimum trapping, as predicted by the simulations. Furthermore the measurement also demonstrates a cut-off power at around 20 mW. We do however find some differences between the simulations and the experiments. The atom number seems to flatten off after a certain power has been reached. However from the simulations we expected a clear optimum power for a given detuning. Subsequent experiments did show a misalignment of the Zeeman slowing beam, which could have limited the power available for slowing. The optimum detuning in the experiment at 69 mW is -589 MHz, which is about 20 MHz lower than predicted. Furthermore the curves in the simulation are about 30 MHz wider than in the simulation. This can have several reasons, which makes it hard to determine the actual cause. A possible cause is that the light reflected inside the Zeeman slower results in some scattering events that push the atoms in the opposite direction. Even a small reflection could lead to a significant shift in the optimal detuning. A different possibility is that the shim coils of the MOT distort the magnetic field of the Zeeman slower leading to a different optimal detuning. Lastly it is possible that one of the assumptions made in the simulation significantly

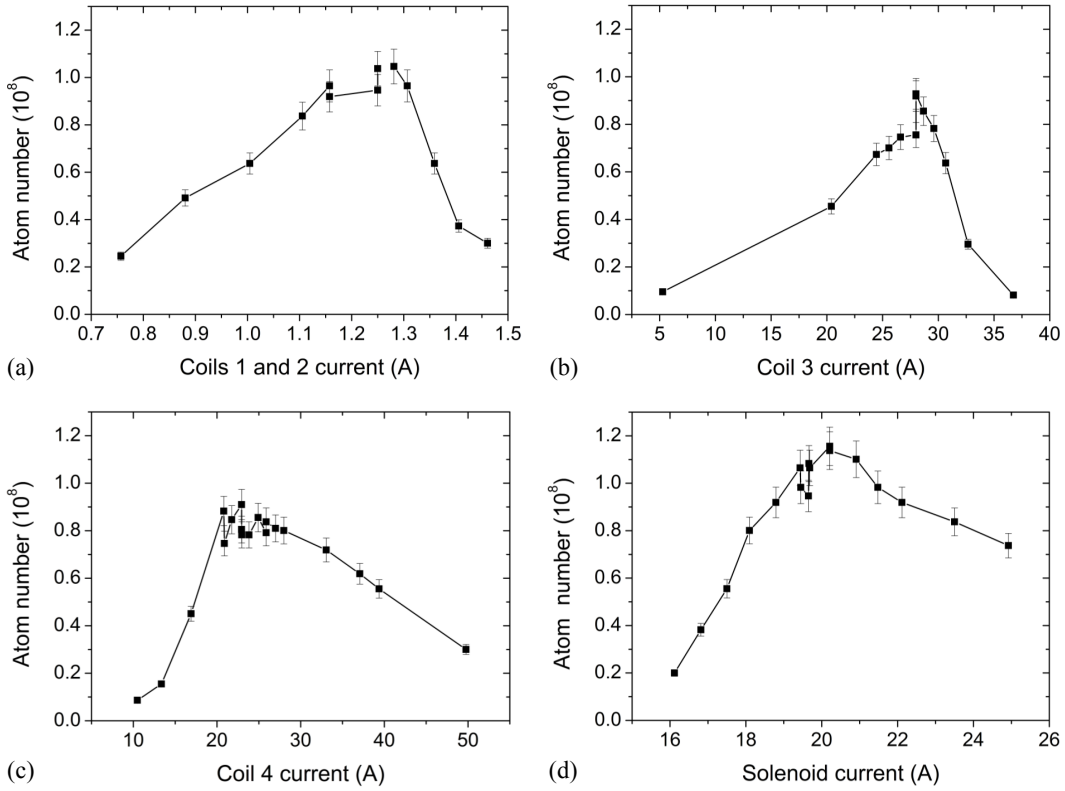

Figure 5.11: Optimisation of Zeeman Slower Coils for caesium. The total MOT load is recorded with changing currents for (a) Coils 1 & 2, (b) Coil 3, (c) Coil 4 and (d) Solenoid. The lines are included as a guide to the eye [1].

distorts the result.

5.4.2 Caesium

The caesium results were previously reported in [1]. They will therefore only be discussed briefly for completeness. In the case of Cs, we use both a main cooling beam and repump beam for the slower. The repump ensures that Cs atoms are not lost to the $F = 3$ hyperfine state. The main cooling light drives the $|F, M_F\rangle = |4, 4\rangle \rightarrow |5, 5\rangle$ transition, while the Zeeman repump drives the $F = 3 \rightarrow F' = 4$ transition (see section 2.2.1). All experiments for the Zeeman slower were again conducted by monitoring the total fluorescence of the MOT. Figure 5.11 shows the optimum current for all the coils. All the optimum currents are given in Table 5.4. The Zeeman detuning was not changed

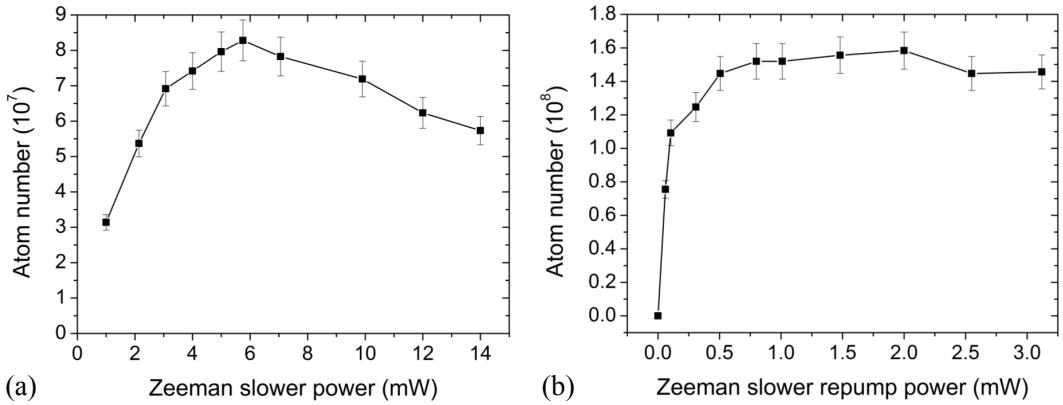

Figure 5.12: Optimisation of the Zeeman slower laser and repump power for caesium. Both experiments investigate the atom number of the MOT. (a) MOT atom number against power of Zeeman slower beam (b) MOT atom number against power of repump beam. Lines are included as a guide to the eye [1].

as changing the solenoid current is essentially equivalent. Figure 5.12 shows the dependencies of the MOT atom number with Zeeman power (a) and Zeeman repump power (b). There is a clear optimum for the power at $6 \pm 0.5\,\mathrm{mW}$. Unlike in ytterbium we do not have a strict threshold power that is required for the MOT. This is because the MOT capture velocity for caesium is a lot higher and therefore some atoms will be trapped without any Zeeman slower. However the atom number increases rapidly with increased power in the Zeeman beam. We expect to find an optimum power as too much power will lead to atoms turning around inside the Zeeman slower due to off-resonant scattering. Figure 5.12 (b) shows that all atoms are lost from the cooling cycle with no repump light. At low repump power any increase will lead to a sharp increase in MOT atom number. At roughly 1 mW power the atom number plateaus, hence the repump light was operated at $3.12 \pm 0.01\,\mathrm{mW}$. The measurements indicates that at least some repump beam is needed to load a MOT successfully. However with enough repump light the loss routes from the cooling cycle can be almost completely suppressed.

Chapter 6

Magneto-Optical Trap

Magneto-optical traps (MOT) have become a standard tool for confining and cooling neutral atoms. The first MOT was constructed in 1987 by Raab *et al.* and trapped 10^7 sodium atoms [125]. Just like modern traps it used the magnetic field created by a pair of anti-Helmholtz coils and 3 retro-reflected laser beams. Through the polarisation of the laser beams a force is created that cools and traps the atoms. In this chapter we outline the underlying physics of the trap (section 6.1) and explore the results obtained for the caesium MOT (section 6.3) and ytterbium MOT (section 6.4). Lastly we show that Cs and Yb could be trapped simultaneously in this experiment (section 6.5).

6.1 Basic Physics

Magneto-optical traps were designed to cool and trap neutral atoms at the same time. The force that makes this possible is created by 6 laser beams in combination with a magnetic field created by an anti-Helmholtz coil arrangement. The inhomogeneous magnetic field in combination with the polarisation of the laser beams can create a force that cools the atoms while pushing them back into the centre of the trap. For the discussion below we will assume a two-level atom. Section 6.1.1 will explore how the magnetic field is created and the resulting Zeeman splitting of the energy levels. We then discuss the cooling and trapping force created by the laser beams (section 6.1.2). Lastly we include a brief discussion of additional cooling effects which can occur when there is hyperfine splitting in the ground state (section 6.1.3).

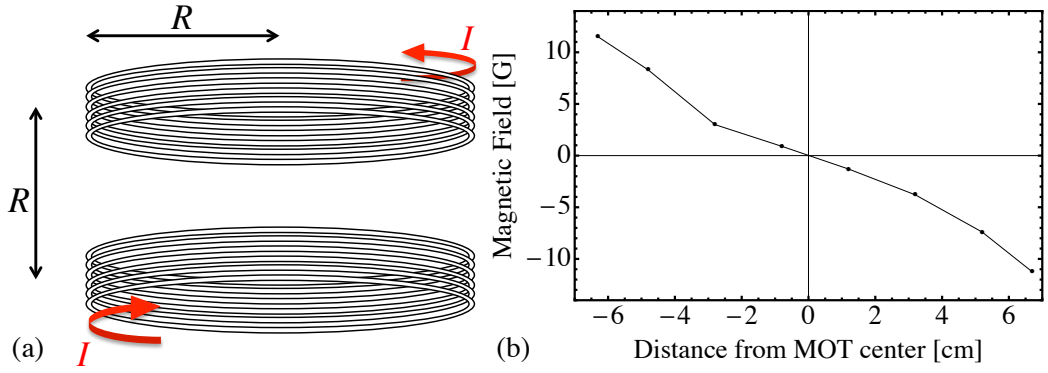

Figure 6.1: (a) Schematic drawing of anti-Helmholtz coil arrangement. Two coils of radius R are separated by the same distance. A current I is run in opposite directions through both coils. (b) Measured vertical magnetic field of the MOT coils at Imperial College London. The slope is not perfectly straight as the coils were not separated exactly by their radius. Lines are included as a guide to the eye.

6.1.1 Magnetic Field

The magnetic field is typically created with two magnetic coils of radius R separated by a distance d so that $d = R$. Figure 6.1 (a) shows the geometric arrangement of the coils. A current I is run through both coils, but in opposite directions. Due to the symmetry of the arrangement there must be a zero magnetic field crossing in the centre between the two coils. Figure 6.1 (b) shows the vertical magnetic field measured with the Imperial College MOT coils. It can be observed that the coils create an approximately linear magnetic field slope with a zero crossing in the centre. A similar field is created in the horizontal directions, but with half the gradient. Hence the Zeeman effect will create an energy splitting of the M_J quantum states. In Figure 6.2 the example of ytterbium is illustrated, where $J_g = 0$ in the ground state and $J_e = 1$ for the excited state. The level structure for caesium is more complicated, but the basic principles remain the same. The Zeeman shift is given by equation (2.13):

$$E_{\mathrm{Ze}} = g_J M_J \mu_{\mathrm{B}} B \,. \tag{6.1}$$

As the magnetic field B is varying approximately linearly with position ($B = B' z$, where B' is a constant), the energy shift is position dependent:

$$E_{\mathrm{Ze}} = g_J \, M_J \, \mu_{\mathrm{B}} \, B' \, z \tag{6.2}$$

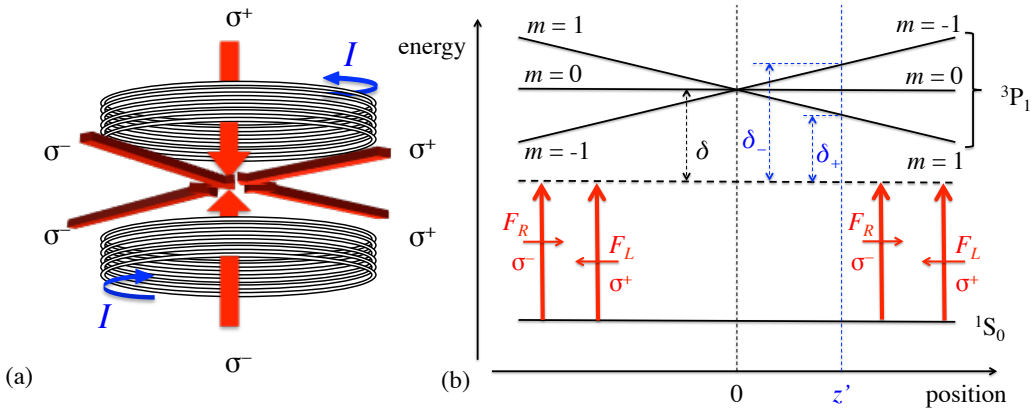

Figure 6.2: (a) Schematic drawing of the six laser beams with the relevant polarisation and the two MOT coils. (b) Illustration of the relevant energy levels of ytterbium and their Zeeman splitting due to the magnetic field. The energy gap addressed by the laser beams is shown with red arrows. We highlight a position z' at which the laser beam is δ_- detuned from the $M_J = -1$ level and δ_+ detuned from the $M_J = 1$ level. Not to scale.

This effect can be used in combination with laser beams to create a position-dependent force, which pushes the atoms into the centre.

6.1.2 Laser Force

Six laser beams are aligned through the centre of the MOT where the magnetic field is crossing zero. Figure 6.2 (a) shows that two counter-propagating beams are aligned along each 3D axis. This arrangement is necessary so the atoms can be pushed back to the centre from any position inside the MOT region. An atom in the MOT can interact with all 6 laser beams. Therefore the interactions need to be engineered so that the main scattering occurs with the beams that will push the atom back to the centre of the trap. We will discuss a one dimensional system in detail to explain the interactions.

We consider the force on an atom at position z' as indicated in Figure 6.2 (b). The atoms interacts with a laser beam from the left with σ^+ polarisation and with a σ^- polarised beam from the right. Figure 6.2 (b) also shows the energy shift of the excited state. The position dependent force of the atom will therefore be the sum of the force

from the beam from the right and the beam from the left:

$$F_{\text{pos}} = F_R + F_L \,. \tag{6.3}$$

The force from one laser is the product of the scattering rate R (see equation 5.1) and the photon momentum h/λ:

$$F_{\text{R}} = \frac{s}{(2\delta_+/\Gamma)^2 + 1 + s} \frac{\Gamma}{2} \frac{h}{\lambda} \tag{6.4}$$

$$F_{\text{L}} = -\frac{s}{(2\delta_-/\Gamma)^2 + 1 + s} \frac{\Gamma}{2} \frac{h}{\lambda} \,, \tag{6.5}$$

where $\delta_{+,-}$ are the detunings of the laser from the $M_J = +1$ and $M_J = -1$ levels respectively (see Figure 6.2 (b)). They can be determined from equation (6.2):

$$\delta_\pm = \delta \pm \frac{\mu B'}{\hbar} z' \,, \tag{6.6}$$

where δ is the detuning of the laser from the $M_J = 0$ level. The coefficient μ can be deduced from equation (6.2):

$$\mu = ((g_J M_J)_e - (g_J M_J)_g)\, \mu_{\text{B}} \,, \tag{6.7}$$

where the subscripts g and e indicate the ground and excited state. By Taylor expanding the two forces to first order we can obtain an approximate position dependent force of:

$$F_{\text{pos}} \approx -\frac{8\,\pi\, s\, \delta\, B'}{(1 + s + (2\delta/\Gamma)^2)^2} \frac{z'}{\lambda} \,. \tag{6.8}$$

Hence the position-dependent force is proportional to $-z'$, which means that any atom will experience a force towards the centre of the trap. The force experienced by the lasers however will not only depend on the position, but also on the velocity of the atom. As a travelling atom will see the light Doppler shifted it will be brought closer to resonance with the beam it is travelling towards. If we ignore the position dependence of the detuning and only consider the velocity dependence, the detuning of the left and right beams can be given as:

$$\delta_{r,l} = \delta \pm 2\pi \frac{v}{\lambda} \,. \tag{6.9}$$

Again by Taylor expanding to first order the velocity-dependent force can be given as:

$$F_{\text{vel}} \approx -\frac{16\pi\, h\, s\, \delta}{(1+s+(2\delta/\Gamma)^2)^2}\frac{v}{\Gamma\lambda^2}\,. \tag{6.10}$$

Hence, to a good approximation, the total force consists of two parts; one proportional to the position $-z'$ and one proportional to the velocity of the atom $-v$. The velocity-dependent part of the force acts as a friction term, which always acts to slow down the atom. This force will therefore provide the cooling in the MOT. The position-dependent part always provides a push towards the centre of the trap confining the atoms. In 3D these consideration apply for all three laser axes separately.

We can derive a cooling limit due to this technique by considering the spontaneous emission events. Again only one dimension will be considered. For n scattering events, the average momentum change of the atom is given by:

$$\Delta p = \sqrt{n}\frac{h}{\lambda} = \sqrt{Rt}\frac{h}{\lambda}\,. \tag{6.11}$$

The average number of scattering events n in a time t is given by $R \times t$. The average energy of the atom can be expressed as:

$$\left\langle \frac{1}{2\,M}(\Delta\vec{p})^2 \right\rangle = \frac{1}{2\,M}(\Delta p^2) = \frac{1}{2\,M}\left(Rt\frac{h^2}{\lambda^2}\right)\,. \tag{6.12}$$

The heating rate is therefore given by:

$$\frac{d}{dt}\left(\frac{1}{2\,M}\left(Rt\frac{h^2}{\lambda^2}\right)\right) = \frac{h^2}{2\,M\,\lambda^2}R = \frac{h^2\,\Gamma}{M\,\lambda^2}\,\frac{s}{1+s+4\delta^2/\Gamma^2}\,. \tag{6.13}$$

This needs to be compared to the cooling rate rate, which is the rate at which the atom loses kinetic energy:

$$\frac{d}{dt}\left(\frac{1}{2}Mv^2\right) = mv\frac{dv}{dt} = vF_{\text{vel}}\,, \tag{6.14}$$

where F_{vel} is given by equation (6.10). In equilibrium the heating and cooling rates are equal. Hence using the equipartition theorem in 1D

$$\frac{k_B T}{2} = \frac{mv^2}{2} \tag{6.15}$$

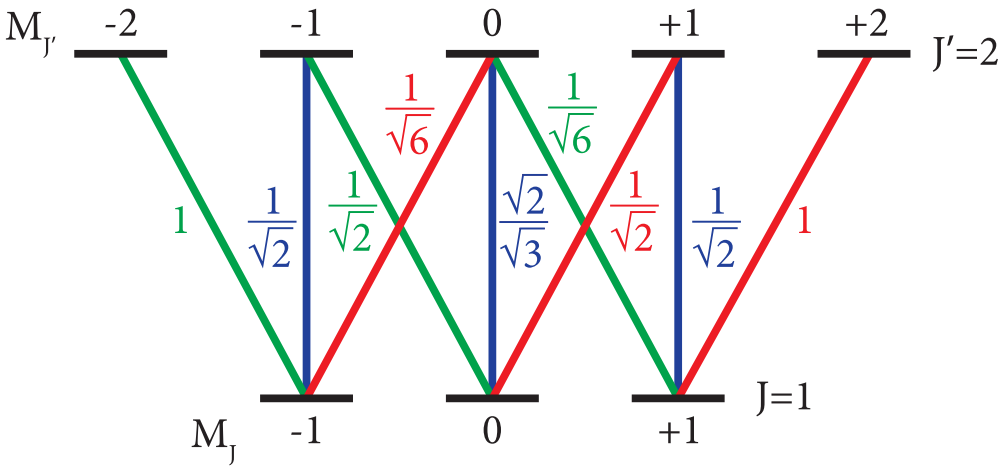

Figure 6.3: Clebsch-Gordan coefficients for the ground state $|g, J = 1\rangle$ and excited state $|e, J' = 2\rangle$ transitions. Figure take from [2].

a temperature limit can be deduced:

$$T = \frac{h\Gamma^2}{16\pi k_B |\delta|}(1 + s + 4\delta^2/\Gamma^2)\,. \tag{6.16}$$

This temperature is minimised when $s \ll 1$ and $\delta = -\Gamma/2$:

$$T_D = \frac{h\Gamma}{4\pi k_B} = \frac{\hbar\,\Gamma}{2\,k_B}. \tag{6.17}$$

In the case of ytterbium this leads to a limit of $4.5\,\mu$K for the ${}^1S_0 \rightarrow {}^3P_1$ transition. The $6\,{}^2S_{1/2} \rightarrow 6\,{}^2P_{3/2}$ Caesium transition has a Doppler limited temperature of $125.6\,\mu$K. However due to the hyperfine structure of Caesium sub-doppler cooling is possible.

6.1.3 Sub-Doppler Cooling

There are two common sub-Doppler cooling mechanisms that can occur in an optical trap. For beams with linear-polarisation Sisyphus cooling will occur. As this method would require changing the polarisation of our MOT beams, we did not test for this cooling mechanism. A detailed description is given by Dalibard and Cohen-Tannoudji [126]. For σ^+ and σ^- polarised beams, as we have in the MOT, the sub-Doppler cooling force originates from a selective absorption process due to optical

pumping. The beam arrangement leads to an overall linear polarisation, where the polarisation angle rotates through 2π over the distance λ. We will discuss an atom with ground state $|g, J = 1\rangle$ and excited state $|e, J' = 2\rangle$ for simplicity. Figure 6.3 shows the Clebsch-Gordon coefficients for the two states. Consider this atom at rest under linearly polarised light. An atom excited through π-absorption from $M_J = \pm 1$ will decay to the $M_J = \pm 1$ and $M_J = 0$ levels with equal probability. However an atom excited from the $M_J = 0$ level is twice as likely to decay back to $M_J = 0$. This will result in pumping into the $M_J = 0$ level, which is the steady state solution. However for a moving atom the polarisation axis will rotate. Due to the intrinsic pumping time the steady state solution is not always maintained and the population of $M_J = \pm 1$ can be greater. Which sub-level has greater population depends on the travelling direction of the atom. An atom travelling towards the σ^+ beam will have greater population in $M_J = +1$ and an atom travelling towards the σ^- beam will have more population in the $M_J = -1$ level. As can be seen in Figure 6.3, the Clebsch-Gordan coefficients make it six times more likely for an atom in $M_J = +1$ to absorb σ^+ light than σ^- light. The opposite is true for the $M_J = -1$ level. Hence the atom will absorb more light from the beam it is travelling against. This adds an additional friction effect, which will lead to more cooling. For Cs this scheme works similarly for the M_F quantum numbers.

6.2 MOT Design

The MOT is built around the science chamber shown in Figure 3.9 (a). Eight of the sideview ports are designated for the MOT and the absorption imaging of the MOT. Furthermore the top and bottom viewports are used for the vertical MOT beams of both Yb and Cs. The MOT coils are placed inside the re-entrant viewports on the top and bottom. Each coil is wound with square wire 4.3 mm wide and high and consists of 24 turns stacked 6 layers high and 4 layers wide. To fully control the magnetic field offset inside the MOT chamber three pairs of shim coils are placed around the Science chamber (see Figure 6.4). These shims operate in pairs of East-West, North-South and Top-Bottom. Furthermore there is a single compensation coil, which can compensate a field gradient, that may occur from the Zeeman slower.

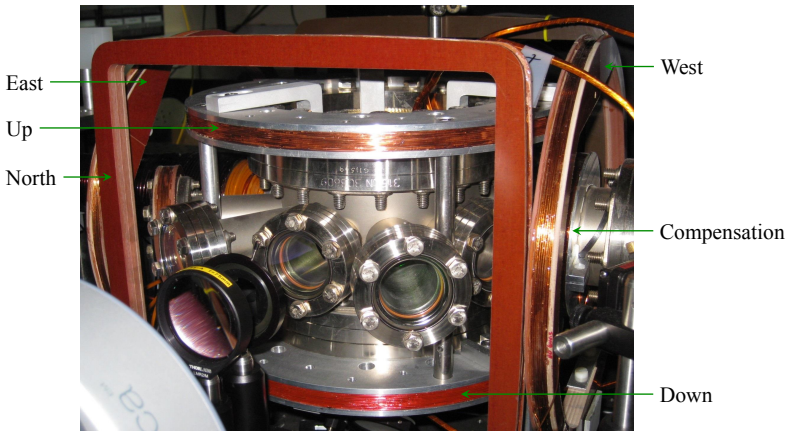

Figure 6.4: The position of the shim and compensation coil around the MOT. The East, West, North, Top and Bottom shim coils can be seen. The South shim coil is located on the other side of the Science chamber [1].

6.3 Caesium MOT

The caesium MOT operates on the $6\,S_{1/2} \rightarrow 6\,P_{3/2}\ D_2$ transition. We address the $|F, M_F\rangle = |4, 4\rangle \rightarrow |5, 5\rangle$ hyperfine transition for the main cooling light and the $F = 3 \rightarrow F' = 4$ transition as repump light. After a MOT of caesium was obtained and the Zeeman slower was optimised, we optimised the various MOT parameters (section 6.3.1). We studied the loading rate and lifetime of the MOT (section 6.3.2) and finally took absorption and temperature measurements (section 6.3.3).

6.3.1 MOT Optimisation

The results for optimising the Cs MOT are discussed in [1]. They are also included here for completeness. When optimising the Cs MOT we waited until the MOT was fully loaded before measuring the fluorescence. Figure 6.5 (a) shows a clear optimum detuning for a magnetic field gradient of $8.53\,\mathrm{G\,cm^{-1}}$. Similar curves can be obtained for different magnetic field gradients. Figure 6.5 (b) shows that a magnetic field increase requires the MOT beam to be more red detuned for optimum operation. The graphs demonstrate that a MOT can be obtained at a low magnetic field gradient, which may be important when loading a dual MOT of Cs and Yb. The MOT gradient was set to $8.53\,\mathrm{G\,cm^{-1}}$ for the remaining optimisation processes. At this gradient the optimal detuning from the $F' = 5$ transition is $-6.5 \pm 0.1\,\mathrm{MHz}$.

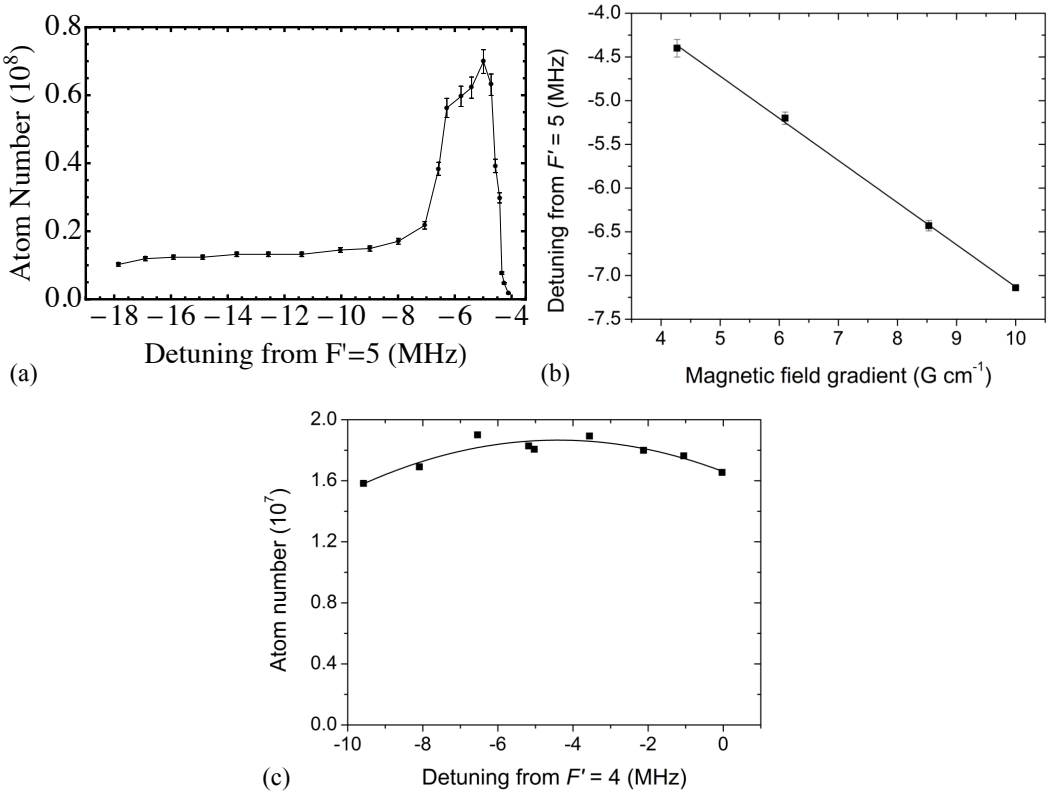

Figure 6.5: (a) The total atom number in the MOT against the MOT beam detuning. The MOT gradient was set to $8.53\,\mathrm{G\,cm^{-1}}$. (b) The optimum MOT detuning for different magnetic field gradients. (c) The MOT number against the detuning of the repump beam [1].

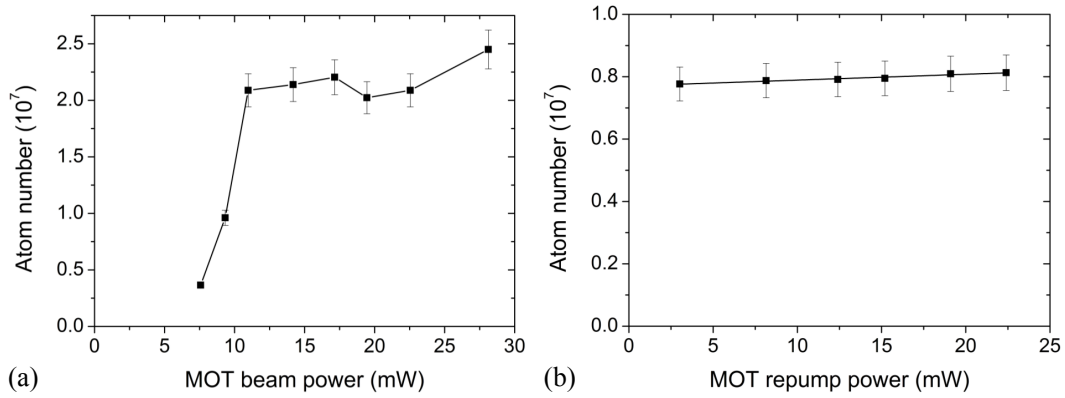

Figure 6.6: Cs MOT number as a function of (a) MOT beam power and (b) repump power [1].

Figure 6.5 (c) shows that the repump detuning is not critical for the operation of the MOT. Good MOT numbers were found between 0 MHz and -10 MHz. The detuning was therefore set at -5.0 ± 0.5 MHz. A more detailed description of the gradient and detuning of the Cs MOT is not necessary for the purposes of this experiment. A dual operation MOT will require a compromise of parameters, which will have to be determined at a later date.

We also investigated the optimal power of the MOT and repump beam. Figure 6.6 (a) shows a minimum power of around 7.5 mW is required in each beam to obtain a MOT. The atom number seems to plateau at around 10 mW, after which increasing the power does not yield a great improvement in atom number. Nevertheless it is advisable to use all the available power for the MOT. Therefore each MOT beam was set to carry 29.9 ± 0.1 mW of power. We also varied the power of the repump light, which can be seen in Figure 6.6 (b). The total atom number in the MOT only varies slightly with the repump power. The MOT was therefore supplied with 13.5 ± 0.1 mW so the Zeeman slower could be supplied with more light.

6.3.2 MOT Loading and Lifetime

Especially for the sequential loading scheme proposed here for loading a dual MOT of Yb and Cs, a fast loading rate and a long lifetime is important. We can measure both by monitoring the fluorescence during a loading sequence or a decay sequence. The loading and lifetime for Cs was also presented in [1]. It is again included for

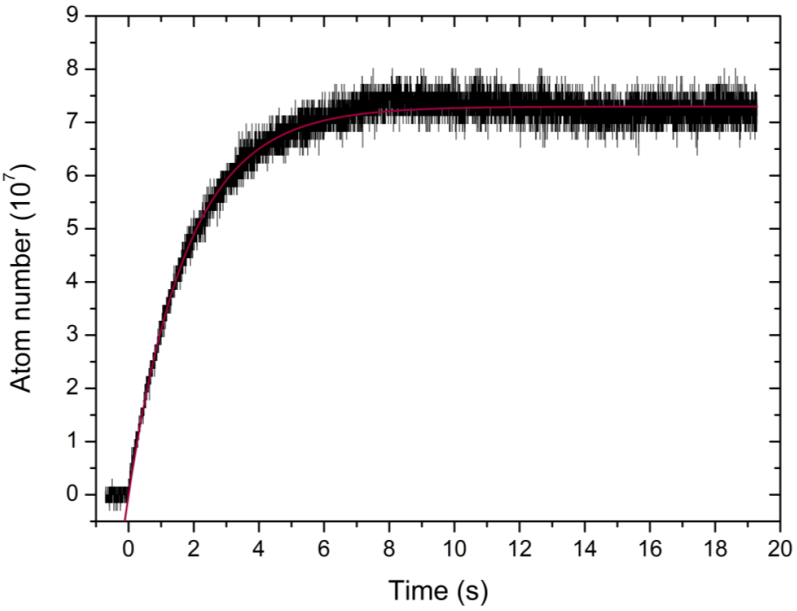

Figure 6.7: A typical Cs MOT load. The red curve shows the fit according to equation (6.19)[1].

completeness.

The rate at which atoms are loaded into the MOT dN_{load}/dt is given by the capture rate from the Zeeman slower κ subtracted by the loss rate:

$$\frac{dN_{\text{load}}}{dt} = \kappa - \frac{N_{\text{load}}}{\gamma} - \frac{\beta N_{\text{load}}^2}{V} \,. \tag{6.18}$$

In the above equation γ is the single body loss rate, that is applicable for atoms being lost due to atom-light collisions or background gas scattering, and β is the two body loss rate from inelastic collisions in the MOT. V is the volume of the MOT as the two body loss rate depends on the density of the atoms. During loading we expect that the two body loss rate is negligible. Hence the MOT atom number can be expressed as:

$$N_{\text{load}}(t) = \frac{\kappa}{\gamma}(1 - e^{-\gamma t}) \,. \tag{6.19}$$

This equation was fitted to the data in Figure 6.7 and we obtain a loading rate of $\kappa = (4.04 \pm 0.01) \times 10^7\,\text{s}^{-1}$ and a loss rate of $\gamma = (0.554 \pm 0.001)\,\text{s}^{-1}$. This loading rate is most likely limited by the oven temperature.

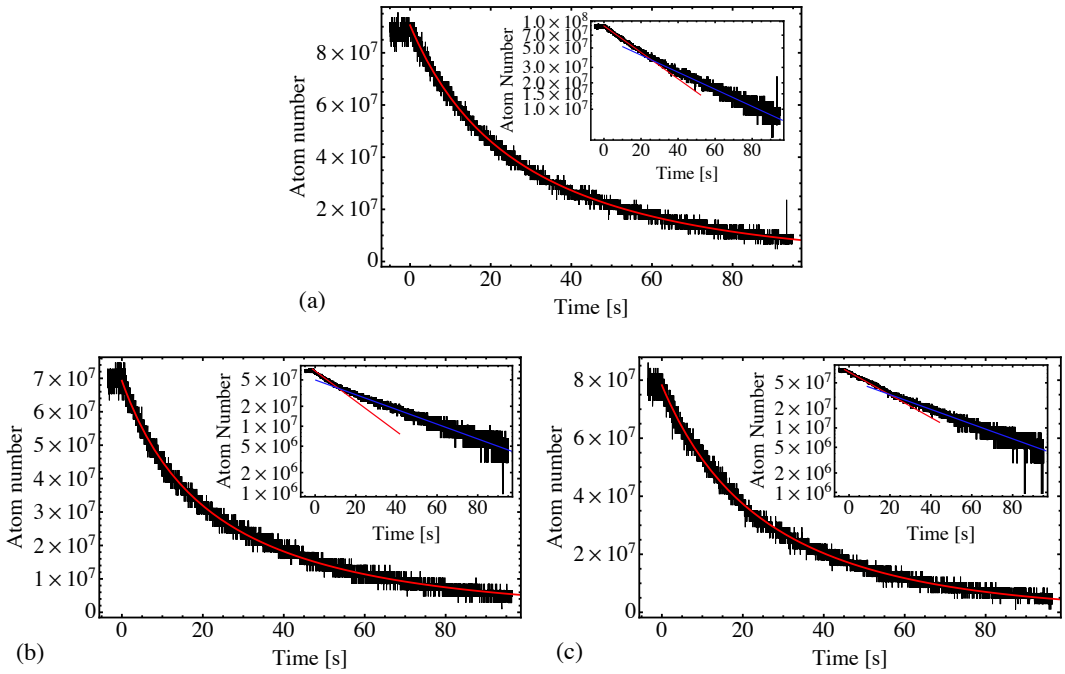

Figure 6.8: The decay of the Cs MOT for different scenarios: (a) Both Zeeman laser beam and atomic beam blocked, (b) only atomic beam blocked and (c) only Zeeman laser beam blocked. The red lines show a fit according to equation (6.21). The insets show the same plot on a logarithmic scale. The red line shows the duration over which two body decay dominates and the blue line shows the time at which single body decay dominate [1].

	γ [s^{-1}]	β/V [s^{-1}]
Atoms and Zeeman beam blocked	0.0170 ± 0.0001	$(2.71 \pm 0.02) \times 10^{-10}$
Atoms blocked	0.0169 ± 0.0001	$(4.81 \pm 0.04) \times 10^{-10}$
Zeeman beam blocked	0.0235 ± 0.0001	$(2.59 \pm 0.03) \times 10^{-10}$

Table 6.1: The single body and two body decay rates of the Cs MOT under various conditions.

The decay rate is given by the single body and two body loss rates:

$$\frac{dN_{\text{decay}}}{dt} = -\frac{N_{\text{decay}}}{\gamma} - \frac{\beta N_{\text{decay}}^2}{V}\,. \tag{6.20}$$

The atom number of the MOT is therefore given by:

$$N_{\text{decay}}(t) = \frac{N_0\left(1 - \tanh\left(\frac{\gamma t}{2}\right)\right)}{1 + \tanh\left(\frac{\gamma t}{2}\right)\left[\frac{2N_0\beta}{\gamma} + 1\right]}\,, \tag{6.21}$$

where N_0 is the initial number of atoms in the MOT. As the volume V could not be measured at the time we have evaluated the quantity β/V. The two body decay rate β will dominate the early decay when the MOT is denser. The single body decay rate γ will dominate the decay after the density of the MOT has dropped. We measure several decay curves with different conditions. Figure 6.8 (a) shows the decay with both the Zeeman slowing beam and the atomic beam blocked. For Figure 6.8 (b) the atomic beam was blocked, but the Zeeman laser beam was still passing through the MOT. Figure 6.8 (c) plots the decay with only the Zeeman laser beam blocked. The insets in each figure shows the same plot on a logarithmic scale. Each plot is fitted with a red and purple line that highlight the areas were the two body and single body decays dominate.

Table 6.1 lists the decay rates obtained by fitting equation (6.21) to the data. The $1/\gamma$ lifetime with both atoms and laser blocked is $58.8 \pm 0.3\,$s. For the atomic beam blocked, we obtain a lifetime of $59.34 \pm 0.4\,$s. These values are the same within error bars showing that the Zeeman laser beam does not lead to any increase in single body loss. The two body loss rate however does increase as the Zeeman beam can heat the atoms, which will increase the inelastic scattering rate. When the Zeeman beam is blocked, but the atoms are not, the fast atomic beam will collide with atoms in the MOT. This can knock the atoms from the trap leading to an increase in the single

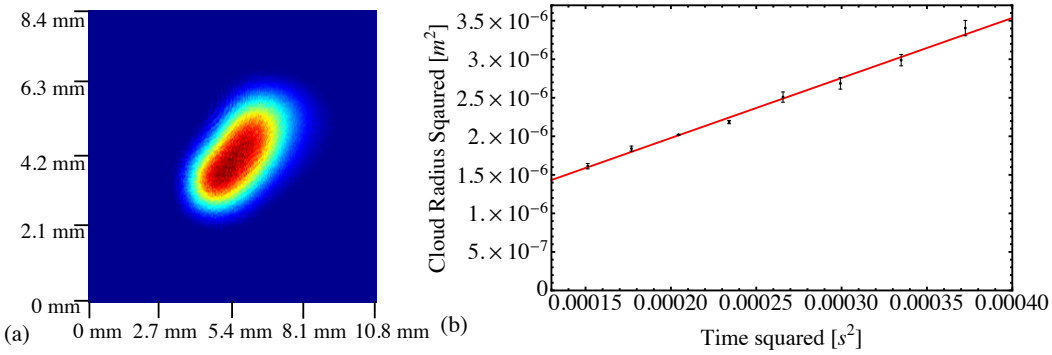

Figure 6.9: (a) Absorption image of Cs atoms inside the MOT. (b) Time of flight expansion of a Cs MOT after it is released from the trap. Red line shows the linear best fit.

body loss rate. The lifetime was measured to be $42.6 \pm 0.2\,\mathrm{s}$.

6.3.3 Absorption Imaging and Temperature

The optics for the Cs absorption imaging are outlined in section 4.1.3. The images obtained by the CCD camera can be analysed to find the atom number and the temperature of the atoms.

The atom number can be determined by summing over the optical depth of all pixels of the camera. It is given by:

$$N = m\frac{A_{\mathrm{pixel}}}{\sigma}\sum_{\text{all pixels}} O.D._{\mathrm{pixel}}\,, \tag{6.22}$$

where A_{pixel} is the size of the pixel of the camera, m is the magnification of the image and σ is the scattering cross section (see equation (3.9)). For Cs we measured the absorption image with $m = 2.08$ and a 2 by 2 binning. Figure 6.9 (a) shows a typical absorption image of caesium. Using the above equation the atom number of the best Cs MOT measured was 5.5×10^8.

The temperature can be evaluated by turning off the MOT beams and letting the Cs cloud expand. Absorption images can be taken during different points of the expansion to determine the size of the cloud. From the speed of the expansion the temperature of the cloud can be determined. The relation between the radius of the could r and

the temperature is given by [127]:

$$r^2(t) = r_0^2 + \frac{2k_B T}{M} t^2 \,, \tag{6.23}$$

where r_0 is the initial radius of the MOT. The gradient of a plot of r^2 against t^2 is therefore proportional to the temperature of the MOT. Figure 6.9 (b) shows this plot for the caesium MOT. The temperature is determined as $125 \pm 4\,\mu$K. This is lower then the temperature limit of $234\,\mu$K, which is obtained through equation (6.16) and the optimal MOT parameters. The extra cooling can be explained through sub-Doppler cooling (see section 6.1.3).

6.4 Ytterbium MOT

The ytterbium MOT was designed on the $^1S_0 \rightarrow {}^3P_1$ intercombination line. As it has a small linewidth of 183 kHz we expect to achieve a very cold MOT. Obtaining an initial MOT signal on the intercombination line can be a challenge. In section 6.4.1 the successful procedure in finding a MOT is discussed. Section 6.4.2 reviews the various parameters that influence the MOT and shows the optimisation process. The loading rate and lifetime of the optimised MOT is discussed in section 6.4.3. And lastly section 6.4.4 presents the final atom number and temperature of the MOT obtained by absorption imaging.

6.4.1 Search for Ytterbium MOT

The main problem in observing the first MOT turned out to be nulling the magnetic field in the centre of the science chamber. The MOT has several coils around it (see section 6.2), which all contribute to the central magnetic field. Therefore when changing the current through one coil it is likely that a different coil will need to be adjusted to maintain the magnetic field zero in the centre of the system. As the system is closed off the magnetic field at the centre cannot be measured with a Hall probe. However in the Durham system the caesium MOT could be effectively used for measuring the magnetic field, as it will always sit at the magnetic field zero. We could therefore switch all currents to the desired Yb currents and observe the position of the MOT. When switching directly the caesium MOT disappeared completely indicating that the magnetic field zero was not inside the cross over area of the MOT beams. However

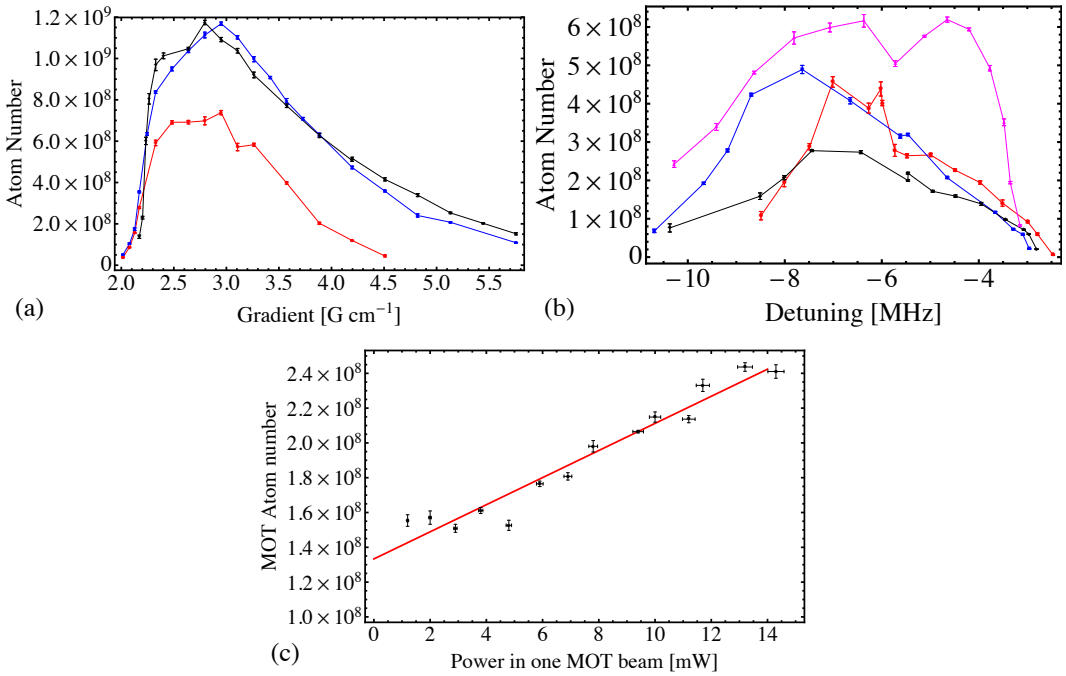

Figure 6.10: Ytterbium MOT optimisation. (a) The 3 s MOT load atom number against the magnetic field gradient in the centre of the MOT. The different curves shows different MOT beam detuning: Red - 4 MHz, Blue - 6 MHz, Black - 8 MHz. Lines are included as a guide to the eye. (b) 3 s MOT load atom number against the MOT beam detuning with various parameters (Sidebands FWHM, MOT beam power, Magnetic field gradient): Red - (Off, 14 mW, 2.9 G cm^{-1}), Blue - (3.35 MHz, 14 mW, 5.1 G cm^{-1}), Black - (3.35 MHz, 7.2 mW, 5.1 G cm^{-1}), Magenta - (6 MHz, 14 mW, 2.9 G cm^{-1}). Lines are included as guide to the eye. (c) The 3 s MOT load against the power in a single MOT beam. Measured with 3.35 MHz sidebands and 2.9 G cm^{-1} MOT magnetic field gradient.

we could observe the direction in which the caesium atoms were pushed. With this information the shim coils were adjusted so that eventually the MOT remained in the centre when the Zeeman slower was switched to ytterbium currents. With those adjustments the ytterbium MOT was found quickly by simply scanning the detuning of the Zeeman slowing beam.

6.4.2 MOT Optimisation

The atom number in the MOT can be influenced by a wide variety of parameters that can be dependent on each other. We will discuss the optimisation of the MOT beam

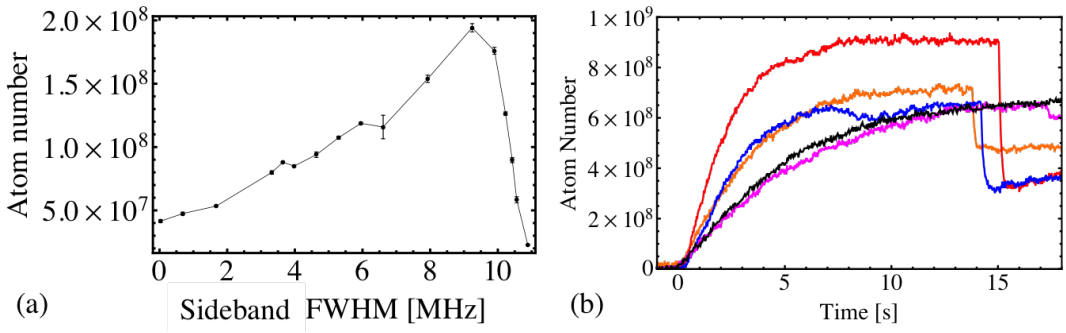

Figure 6.11: (a) The 3 s MOT load atom number against the sideband FWHM. The data was taken with 2.9 G cm^{-1} magnetic field gradient, 6 MHz detuning and 14.3 mW power in each laser beam. (b) Fluorescence measurement of MOT loading curves for different sideband settings. The magnetic field gradient was set to 2.9 G cm^{-1} and the detuning was 4.8 MHz. The sharp steps in the curve show the point at which the sidebands were turned off. The FWHM of the sidebands was: Black - No Sidebands, Magenta - 2 MHz, Orange - 4 MHz, Blue - 6 MHz, Red - 7 MHz.

detuning, sidebands and power, as well as the MOT gradient. All data is obtained by loading the MOT for 3 s 8 to 10 times and averaging the results of the detected fluorescence. The atom numbers were calculated from this as outlined in section 4.2.5.

We began by investigating the effect of the MOT magnetic field gradient. For these experiments we kept the MOT sidebands at 3.35 MHz FWHM (for detail on the sidebands see section 4.2.4). Figure 6.10 (a) shows the 3 s MOT load with varying gradient for different detunings. We do not observe a different optimal MOT gradient for different detunings as we did in the Cs MOT. Instead there seems to be an optimum for all detunings at a gradient of 2.9 G cm^{-1}. Figure 6.10 (b) investigates the MOT load when varying the MOT beam detuning. For this we operated the MOT under various parameters. For all the parameters we discover an optimum between 6 and 8 MHz. The black and blue curves indicate that a smaller optimum detuning is needed if the power of the MOT beams is lowered. The red curve shows that without sidebands we obtain a good MOT with detunings between 6 and 7 MHz. Figure 6.10 (c) plots the MOT atom number against the power in a single MOT beam. The 3 beams were balanced during this experiment so that roughly equal power was present in all. It is observed that the MOT number drops steadily with decreasing power. The red line shows the best linear fit to the data points. As we cannot have a MOT without light we expect a very sharp drop in atom number between 0 and 2 mW. However at those

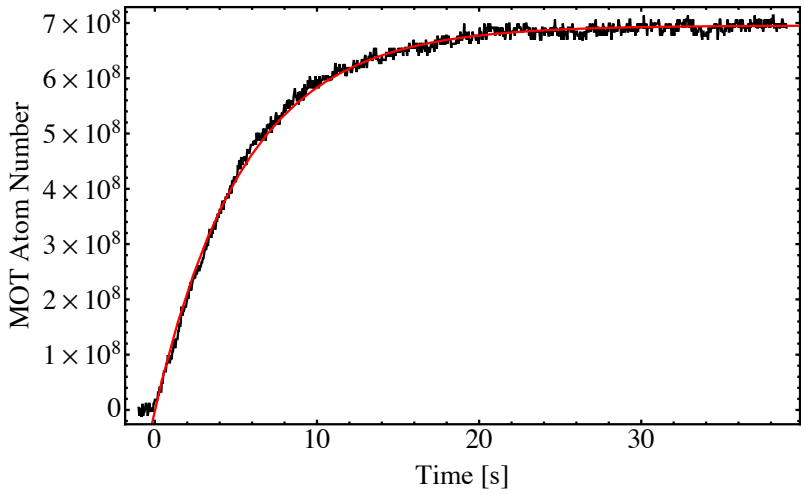

Figure 6.12: Loading curve of the Yb MOT. The red line shows a fit according to equation (6.19).

levels the fluorescence was not bright enough to measure a signal. Furthermore we do not observe the atom number levelling off as was the case in caesium. We therefore suspect that if more power was available a larger MOT could be obtained. Figure 6.11 (a) shows the effect of the sidebands on the total MOT atom number. It is observed that the atom number has a clear maximum at sidebands with 9 MHz FWHM. For larger sidebands the atom number drops rapidly as part of the light will move close to resonance. Figure 6.11 (b) shows MOT loading curves for different sidebands. After the MOT was fully loaded the sidebands were switched off, which shows as a sharp drop in the curves. We observe that the MOT loads faster and holds more atoms with larger sidebands. However when the sidebands are switched off we do rapidly lose atoms. All the atom numbers were calculated using equation (4.12). This equation does include the sidebands, but it cannot be independently verified. It is therefore possible that the sharp fluorescence drop is simply due to loss of fluorescence and not loss of atoms. As it was possible to load a good MOT without sidebands we concluded that they were not necessary for future experiments. The MOT is operated with a magnetic field gradient of $2.9\,\mathrm{G\,cm^{-1}}$, a detuning of 6.0 ± 0.1 MHz and the maximum available power of 14.3 ± 0.2 mW in each MOT beam.

	γ [s^{-1}]	β/V [s^{-1}]
Atoms and Zeeman beam blocked	0.0232 ± 0.0003	$(2.7 \pm 0.1) \times 10^{-11}$
Atoms blocked	0.0470 ± 0.0007	$(1.2 \pm 0.2) \times 10^{-10}$
Zeeman beam blocked	0.0475 ± 0.0004	

Table 6.2: The single body and two body decay rates of the Yb MOT under various conditions.

6.4.3 MOT Loading and Lifetime

As in the case with Cs we measure the loading rate and lifetime of the ytterbium MOT. It is necessary to compare these values to the results of Cs as in the dual MOT the species will have to be loaded sequentially. For this a sequential loading scheme needs to be designed that should be based on the loading rates and lifetimes of both MOTs.

The loading of the Yb MOT can be analysed according to the same theory as the Cs MOT (see section 6.3.2). We therefore fitted the data according to equation (6.19). We obtain the loading rate $\kappa_{\mathrm{Yb}} = (1.27 \pm 0.01) \times 10^8$ s^{-1} and a single body decay rate $\gamma_{\mathrm{Yb}} = 0.182 \pm 0.001$ s^{-1}. Compared to the loading of the Cs MOT we obtain about triple the loading rate. This indicates the Yb MOT is loading much faster.

The lifetime was again analysed in three different scenarios. Figure 6.13 (a) shows the decay curve of the MOT with both the Zeeman slower light and the atomic beam blocked. Figure 6.13 (b) shows the decay rate with the atoms blocked and (c) plots the the decay curve with the Zeeman slowing beam blocked. The two and single body decay rates are outlined in Table 6.2. The blocking and unblocking of the atomic and Zeeman beam has similar effects as with the Cs MOT. If only the atoms are blocked the Zeeman beam will lead to increased heating, which increases the two body decay rate. However we also see a significant increase in the single body decay rate, which is most likely due to atoms escaping from the cooling cycle. With only the Zeeman beam blocked, the un-decelerated atoms will cause collisions inside the MOT increasing the single body decay rate. As can be seen in the insets in Figure 6.13 (c) this effect is so strong that the two body decay is almost completely negligible. It was therefore not possible to measure an accurate two body decay in this case. The $1/\gamma$ lifetimes of the three scenarios are 43.1 ± 0.7 s, 21.3 ± 0.2 s and 21.1 ± 0.2 s respectively.

As can be seen ytterbium has a faster loading rate, but a shorter lifetime compared with the caesium MOT. It is therefore advisable, in the sequential loading scheme, to load Cs before Yb. Section 6.5 outlines the loading sequence used to obtain a dual

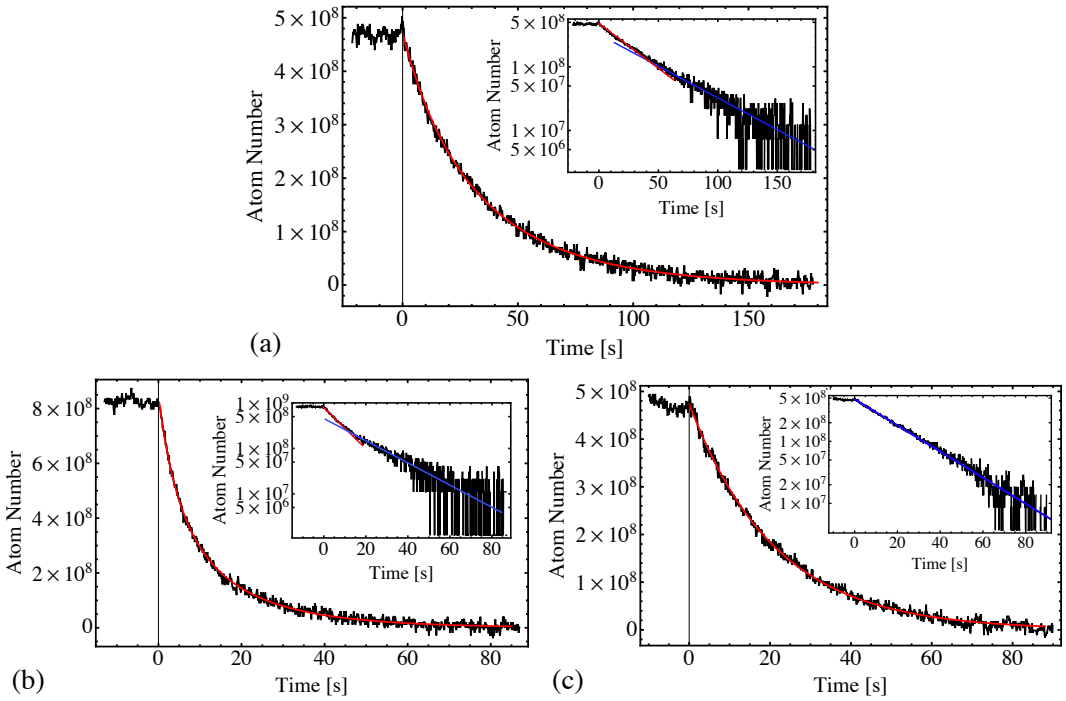

Figure 6.13: Decay curves of Yb MOT. The red lines in each curve show a fit according to equation (6.21). The insets in each curve show the same data on a log scale. The red line shows the timespan dominated by two body decay and the blue line shows the timespan dominated by single body decay. (a) Both Zeeman beam and atomic beam blocked, (b) atomic beam blocked and (c) Zeeman beam blocked.

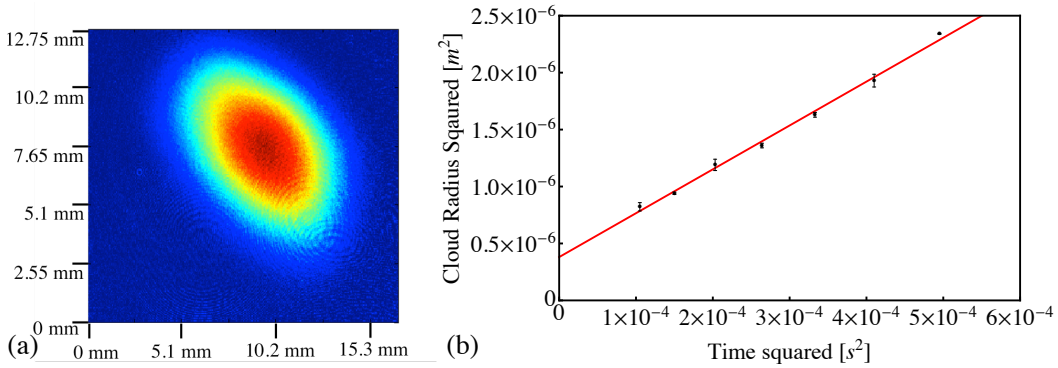

Figure 6.14: Absorption imaging data of the Yb MOT. (a) Absorption image of atoms captured inside the MOT. (b) Expansion of ytterbium cloud after release from MOT.

MOT.

6.4.4 Absorption Imaging and Temperature

The optics used for the absorption imaging of the Yb MOT was outlined in section 4.2.5. An absorption image of the Yb cloud can be seen in Figure 6.14 (a). We imaged the Yb MOT with a magnification $m = 2.5$ and 2 by 2 binning. The image was taken with the Zeeman beam present, which did heat the cloud significantly. As with the Cs setup the total atom number of the MOT can be calculated from the optical depth of the image (see equation (6.22)). For the strongest MOT loads we observed 4.7×10^9 atoms.

The temperature was measured with the same method employed for Cs (see section 6.3.3). The expansion of the cloud after release from the MOT can be seen in Figure 6.14 (b). The fitted red line according to equation (6.23) indicates a temperature of $81 \pm 2\,\mu$K. The initial cloud radius was evaluated as 0.61 ± 0.02 mm. This temperature curve was taken with 11.7 mW in each MOT beam and a detuning of 4.7 MHz. Using equation (6.16) with these parameters we obtain a Doppler limited temperature of $27\,\mu$K. The additional heating can be due to multiple scattering events of a single photon inside the optically thick cloud [128].

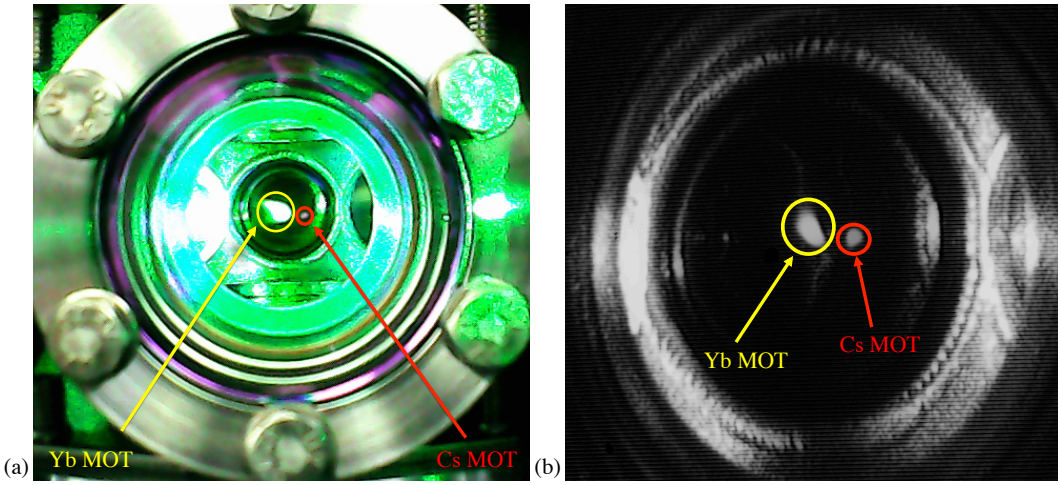

Figure 6.15: Pictures of the Dual MOT. (a) Sideview in colour of the Yb and Cs MOT taken while the Yb MOT was loading. (b) Black and white image of the MOTs separated in space.

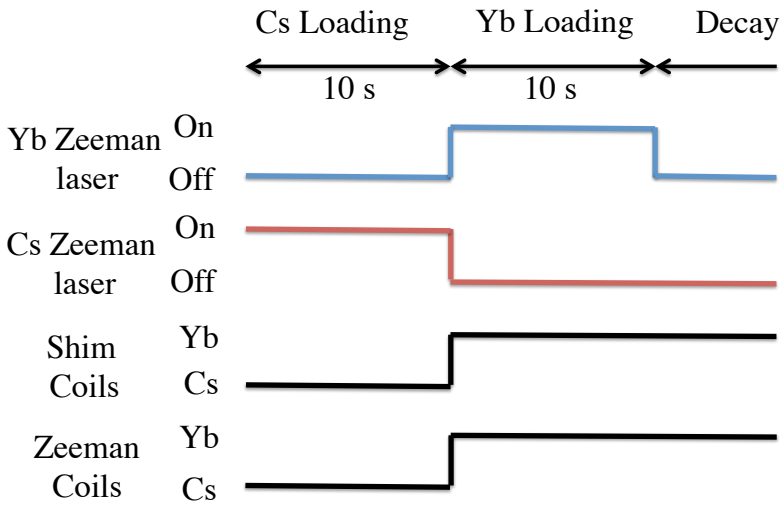

Figure 6.16: Loading sequence used to obtain preliminary dual MOT. Cs is loaded first. After 10 s Cs Zeeman beam is switched off and Yb Zeeman beam switched on. Simultaneously the Shim and Zeeman coils are switched from Cs to Yb settings. Ytterbium is loaded for another 10 s. Then the Yb Zeeman beam is switched off so both MOTs are decaying.

6.5 Dual MOT operation

Figure 6.15 shows two pictures of both MOTs present in the Science chamber at the same time. The two species were loaded sequentially for 10 s each (see Figure 6.16). We first loaded a Cs MOT for 10 seconds with a MOT Gradient of $5\,\mathrm{G\,cm^{-1}}$. We then switched the currents of the Zeeman slower and the shims to the values required for loading Yb. We did not change the MOT magnetic field gradient. With this switch the Cs MOT started to decay and the Yb MOT started to load. The picture in Figure 6.15 (a) was taken when the Yb MOT was loading. The beam pushing of the Zeeman beam, especially at the edges where the MOT force is weak, stretch the MOT out in the form of a sail. After loading the Yb MOT for another 10 seconds the Yb Zeeman beam was blocked. It is important to note that this process only represents a starting point for further optimisation of the loading process. Figure 6.15 (b) shows a black and white image of both MOTs after the loading process was completed. The MOTs should be overlapped as they should both be situated at the zero magnetic field point. However, as the MOT beams are retro-reflected, it is likely that the atoms are receiving more push from one side. This pushing can displace the MOT from the magnetic field zero and separate the two atomic species in space. This effect can be counter-acted by changing the collimation of the MOT beams to equalise the intensity of the direct and retro-reflected beams. With this change it should be possible to bring both MOTs to the magnetic field zero, where they should overlap. It is important to do this so that scattering behaviour of the overlapping MOTs can be studied.

Chapter 7

Conclusion

This chapter provides a summary of the work in this thesis. It also outlines the next steps to be taken towards creating an optical lattice with ultracold polar molecules.

7.1 Summary

This thesis shows the initial steps taken towards producing ultracold ground state polar molecules of caesium and ytterbium. For this it is necessary to cool and trap both species separately. This thesis shows that the current apparatus is capable of trapping ytterbium and caesium simultaneously in a magneto-optical trap.

Such an experiment requires a large complicated vacuum chamber. Initially a vacuum chamber at Imperial College London was constructed for lithium and ytterbium. However due the mechanical error the atomic beam did not travel straight through the chamber. Furthermore it was impossible to accurately cancel the magnetic field in the centre of the trap. As the plan was to move all the laser systems to Durham, the Imperial system was discontinued. At Durham University a vacuum chamber for caesium and ytterbium was built. It was designed so both species could be slowed with the same Zeeman slower. For this a dual species oven was required. The oven built is split into different sections for caesium and ytterbium, which can be held at different temperatures. Strong atomic beams could be achieved for both species. The vacuum chamber consisted of a long tube for Zeeman slowing leading into a large chamber for trapping and cooling. This chamber was designed with several viewports to give the optical access required for the experiment. The vacuum system was continuously pumped by several ion pumps and two non-evaporable getter pumps.

Different laser systems were needed to slow and cool ytterbium and caesium. The caesium laser system consisted of two commercial diode laser systems. One was used to address the cooling transition and the second to address the repump transition. The cooling light is amplified through a tapered amplifier to achieve the necessary power. Two laser frequency stabilisation methods are employed to lock the lasers. The cooling laser is stabilised using modulation transfer spectroscopy. As this method only yields strong signals for closed transitions the repump laser was locked using frequency modulation spectroscopy. For ytterbium two atomic transitions needed to be addressed at very different wavelengths. The 399 nm light, which was used for the Zeeman slower, is created by a pair of diode lasers which are set up in an injection system. One diode serves as the master diode which is housed in an extended cavity system to ensure it is lasing single mode. The second laser is injected with the light from the first. If the laser is injected with the right amount of power it will lase on the same mode as the incoming light. This scheme was used to obtain the power required for Zeeman slowing. The laser was locked using a transfer cavity lock. A small portion of its light was coupled into a scanning Fabry-Perot cavity. The light from the 556 nm laser, which is separately stabilised, was passed through the same cavity. Therefore transmission peaks of both lasers could be measured relative to each by relating them to the cavity length. By keeping this relative separation constant the 399 nm light was locked in frequency. The 556 nm light was obtained from a frequency doubled fiber laser, which provided enough power for all necessary applications. To lock the laser several different methods were attempted. Finally the laser was locked simply to a fluorescence signal of a collimated Yb beam. To obtain a good signal a high-gain shielded photodiode was designed. The 556 nm light could be frequency broadened by applying modulation to an acousto-optical modulator. This was done to improve the loading of atoms into the MOT.

The Zeeman slower uses a magnetic field and laser radiation to slow atoms. The spatially varying magnetic field compensates for the Doppler shift a decelerating atom experiences. The Zeeman slower can only decelerate atoms which are travelling below a certain capture velocity. This capture velocity needs to be chosen so a significant fraction of the atoms from the oven are trapped. However a large capture velocity will result in a long Zeeman slower, which is why a compromise is needed. As the laser beam for the Zeeman slower is required to travel through the magneto-optical trap, it is important that the Zeeman light is tuned off resonance. Especially for Yb a

large detuning is required as the 399 nm will lead to considerable heating and pushing of the atoms in the MOT. To avoid that we chose a large detuning for the Zeeman slower. This also has the advantage of creating a steep field cut-off which is required to tune the final velocity of the atoms exiting the Zeeman slower. Two Zeeman slowers were constructed; one for lithium and ytterbium and one for caesium and ytterbium. The lithium-ytterbium slower consisted of an array of coils producing a single field profile that could slow both species. The caesium-ytterbium slower consisted of five magnetic field coils that needed to be switched in current to ensure both species could be slowed sequentially. To ensure the success of the Zeeman slower a numerical simulation following the basic physics principles was used. It shows that the final output velocity of the Zeeman slower can be tuned by the laser power and detuning. The caesium-ytterbium slower was tested and optimised for both species. The MOT atom number was monitored while changing the magnetic field profile and the Zeeman laser power and detuning to achieve optimum operation. We compared the ytterbium experimental results with the numerical simulation and achieved good agreement.

Finally the MOT results for both caesium and ytterbium are discussed. For both MOTs we optimise the MOT light detuning and power as well as the magnetic field gradient. For caesium we also investigate the effects of the repump laser and optimise its power and detuning. For ytterbium we find that broadening the MOT light with sidebands does improve the loading rate and total atom number of the MOT. However a good MOT can also be loaded without sidebands. The sidebands were therefore not used after optimisation. For the optimised MOT the loading rate from the Zeeman slower is measured. Caesium typically loads at a rate of 4×10^7 atoms s^{-1} and ytterbium at 1.2×10^8 atoms s^{-1}. The lifetime is measured for three different scenarios; with both the atomic and Zeeman laser beam blocked, with only the atomic beam blocked and with only the Zeeman laser beam blocked. We find for both species that leaving the Zeeman laser beam on leads to an increase in two body decay rate due to the heating of the atoms. For ytterbium it also significantly increases the apparent single body loss rate due to off-resonant optical pumping into the metastable D states. The fast atoms from the Zeeman slower can knock out atoms trapped in the MOT, leading to an increased single body decay rate. With both atomic and Zeeman beam blocked the Cs MOT lifetime was measured at 58.9 ± 0.3 s and the Yb MOT lifetime was measured as 43.1 ± 0.7 s. The final atom number and temperature of the MOT was determined by absorption imaging. We trapped 5.5×10^8 Cs atoms at $125\pm4\,\mu$K. For Yb we

trapped 4.7×10^9 atoms at $81 \pm 2\,\mu$K. Lastly we demonstrate that a dual MOT of Yb and Cs can be achieved through sequential loading.

This presents significant progress in confining Cs and Yb in an overlapping trap. This is vital for the future steps of the experiment, which are outlined below.

7.2 Outlook

The next steps in creating ultracold CsYb will be to get the Cs and Yb atoms to overlap. This will already open up the opportunity to measure some properties of a CsYb molecule. Through two-photon spectroscopy the energies of the ground state bound molecular levels can be measured. This can be done by illuminating the dual species MOT with laser light red detuned from the 894.6 nm D_1 transition of caesium. The laser will need 450-900 mW power and a large frequency tuning range, which makes this task suitable for a distributed Bragg reflector (DBR) laser. At a CsYb molecular excited state resonance a large amount of atoms will be lost from the trap. As the Cs_2* resonances are known [129], the Cs*Yb resonances can be identified. By using a second laser beam (probe beam) it is possible to scan the two-photon photoassociation. When the second laser is on resonance with transitions between the ground and excited state fewer atoms should be lost. There are three possible causes for this [130]. At low probe intensity the atoms can decay to a molecular ground state. This will lead to fewer spontaneous emission events, which will reduce the loss of atoms from the trap. Bound molecules can also be recaptured if they are returned to their disassociated state through a Raman transition. At higher probe intensity the excited molecular can be shifted out of resonance due to the Autler-Townes effect. From this the energies of the bound molecular levels can be determined. A more detailed method is given in Münchow *et al.* [68].

An overlapping MOT also allows the atoms to be transferred to a bichromatic dipole trap. By using a dipole trap operating at 1064 nm and 532 nm laser, the trap depth can be balanced for both species. In the dipole trap evaporative cooling can be employed to get Cs and the bosonic isotopes of Yb to quantum degeneracy. As ^{174}Yb is the most abundant isotope, it will be the first that should be cooled to quantum degeneracy. Subsequently the ^{170}Yb and ^{176}Yb can be cooled. Fermi cases can be formed by cooling ^{171}Yb and ^{173}Yb. Cooling all isotopes of Yb is important as it is not known which isotope will be favourable for magnetoassociation with a Feshbach resonance. In the

dipole trap it will also be possible to measure the background scattering rate, which is important in predicting the magnetic field that will be required for finding Feshbach resonances.

Whether magnetoassociation with caesium and ytterbium is viable will depend on the magnetic field that is required to find a Feshbach resonances. Currently the calculations predict Feshbach resonances between 1000 G and 4000 G [86]. The experiment is designed with re-entrant viewports to bring magnetic field coils close to the trap and enable large magnetic fields to be produced. However even with such a setup fields much higher than 1000 G will be hard to achieve. The main problem will be that a very precise control of the magnetic field will be required to associate molecules over a potentially narrow Feshbach resonance. This will require very precise control over the current that is passed through the coils. Successfully created Feshbach molecules can be separated from the remaining atoms [131]. Therefore by adiabatically disassociating the molecules through a reversed magnetic field ramp, the disassociated atoms can be detected through absorption imaging. If magnetoassociation of the molecule is not possible, the molecules can be associated using photoassociation [50] or a STIRAP transition [69].

The Feshbach molecule or photoassociated molecule will need to be transferred to its ro-vibrational ground state using STIRAP. The STIRAP process for transferring molecules to their ground state is outlined in Takekoshi *et al.* [65]. A STIRAP process uses a laser pulse coupled between the initial state and an intermediary state and a laser pulse coupled between the final state and the same intermediary state. The process makes it possible to transfer atoms from the initial to the final state without population of the intermediary state. The ground state molecule can potentially be used in a number of interesting experiments. The direction in which the experiment goes will therefore depend on the most promising developments in the research area.

References

[1] Kirsteen Louisa Butler. *A dual species MOT of Yb and Cs*. PhD thesis, Durham University, July 2014.

[2] Aisha Kaushik. *Trapping, transport and polarisation of ultracold lithium*. PhD thesis, Imperial College London, Sep 2014.

[3] S. Truppe, R. J. Hendricks, S. K. Tokunaga, H. J. Lewandowski, M. G. Kozlov, Christian Henkel, E. A. Hinds, and M. R. Tarbutt. A search for varying fundamental constants using hertz-level frequency measurements of cold CH molecules. *Nat Commun*, 4, 10 2013.

[4] S. Truppe, R. J. Hendricks, E. A. Hinds, and M. R. Tarbutt. Measurement of the lowest millimeter-wave transition frequency of the CH radical. *The Astrophysical Journal*, 780(1):71, 2014.

[5] Eric R. Hudson, Christopher Ticknor, Brian C. Sawyer, Craig A. Taatjes, H. J. Lewandowski, J. R. Bochinski, J. L. Bohn, and Jun Ye. Production of cold formaldehyde molecules for study and control of chemical reaction dynamics with hydroxyl radicals. *Phys. Rev. A*, 73(6):063404, Jun 2006.

[6] B. H. McGuyer, M. McDonald, G. Z. Iwata, M. G. Tarallo, A. T. Grier, F. Apfelbeck, and T. Zelevinsky. High-precision spectroscopy of ultracold molecules in an optical lattice. arXiv:1501.01236, 2015.

[7] D. DeMille, S. Sainis, J. Sage, T. Bergeman, S. Kotochigova, and E. Tiesinga. Enhanced sensitivity to variation of m_e/m_p in molecular spectra. *Phys. Rev. Lett.*, 100:043202, Jan 2008.

[8] S. Sainis, J. Sage, E. Tiesinga, S. Kotochigova, T. Bergeman, and D. DeMille. Detailed spectroscopy of the Cs_2 $a\,^3\Sigma_u^+$ state and implications for measurements sensitive to variation of the electron-proton mass ratio. *Phys. Rev. A*, 86:022513, Aug 2012.

[9] J. J. Hudson, B. E. Sauer, M. R. Tarbutt, and E. A. Hinds. Measurement of the electron electric dipole moment using YbF molecules. *Phys. Rev. Lett.*, 89:023003, Jun 2002.

[10] D. Kawall, F. Bay, S. Bickman, Y. Jiang, and D. DeMille. Precision Zeeman-Stark spectroscopy of the metastable $a(1)[^3\sigma^+]$ state of PbO. *Phys. Rev. Lett.*, 92:133007, Apr 2004.

[11] J. J. Hudson, D. M. Kara, I. J. Smallman, B. E. Sauer, M. R. Tarbutt, and E. A. Hinds. Improved measurement of the shape of the electron. *Nature*, 473(7348):493–496, 05 2011.

[12] The ACME Collaboration, J. Baron, W. C. Campbell, D. DeMille, J. M. Doyle, G. Gabrielse, Y. V. Gurevich, P. W. Hess, N. R. Hutzler, E. Kirilov, I. Kozyryev, B. R. OLeary, C. D. Panda, M. F. Parsons, E. S. Petrik, B. Spaun, A. C. Vutha, and A. D. West. Order of magnitude smaller limit on the electric dipole moment of the electron. *Science*, 343(6168):269–272, 2014.

[13] D. DeMille, S. B. Cahn, D. Murphree, D. A. Rahmlow, and M. G. Kozlov. Using molecules to measure nuclear spin-dependent parity violation. *Phys. Rev. Lett.*, 100:023003, Jan 2008.

[14] Fudong Wang, Xiaodong He, Xiaoke Li, Bing Zhu, Jun Chen, and Dajun Wang. Formation of ultracold NaRb feshbach molecules. *New Journal of Physics*, 17(3):035003, 2015.

[15] Goulven Quéméner, Jean-Michel Launay, and Pascal Honvault. Ultracold collisions between Li atoms and Li_2 diatoms in high vibrational states. *Phys. Rev. A*, 75:050701, May 2007.

[16] Wolfgang Lechner and Peter Zoller. From classical to quantum glasses with ultracold polar molecules. *Phys. Rev. Lett.*, 111:185306, Oct 2013.

[17] Richard P. Feynman. Simulating physics with computers. *International Journal of Theoretical Physics*, 21(6-7):467–488, 1982.

[18] D. Jaksch and P. Zoller. The cold atom Hubbard toolbox. *Annals of Physics*, 315(1):52 – 79, 2005. Special Issue.

[19] Immanuel Bloch, Jean Dalibard, and Wilhelm Zwerger. Many-body physics with ultracold gases. *Rev. Mod. Phys.*, 80:885–964, Jul 2008.

[20] D. Jaksch, C. Bruder, J. I. Cirac, C. W. Gardiner, and P. Zoller. Cold bosonic atoms in optical lattices. *Phys. Rev. Lett.*, 81:3108–3111, Oct 1998.

[21] M. Greiner, O. Mandel, T. Essilinger, T. W. Hänsch, and Immanuel Bloch. Quantum phase transition from a superfluid to a Mott insulator in a gas of ultracold atoms. *Nature*, 415:39–44, 2001.

[22] Maciej Lewenstein, Anna Sanpera, Veronica Ahufinger, Bogdan Damski, Aditi Sen De, and Ujjwal Sen. Ultracold atomic gases in optical lattices: mimicking condensed matter physics and beyond. *Advances in Physics*, 56(2):243–379, 2007.

[23] L.-M. Duan, E. Demler, and M. D. Lukin. Controlling spin exchange interactions of ultracold atoms in optical lattices. *Phys. Rev. Lett.*, 91:090402, Aug 2003.

[24] Immanuel Bloch, Jean Dalibard, and Sylvain Nascimbene. Quantum simulations with ultracold quantum gases. *Nat Phys*, 8(4):267–276, 04 2012.

[25] A. Micheli, G. K. Brenner, and P. Zoller. A toolbox for lattice-spin models with polar molecules. *Nature*, 2:341, 2006.

[26] Bo Yan, Steven A. Moses, Bryce Gadway, Jacob P. Covey, Kaden R. A. Hazzard, Ana Maria Rey, Deborah S. Jin, and Jun Ye. Observation of dipolar spin-exchange interactions with lattice-confined polar molecules. *Nature*, 501(7468):521–525, 09 2013.

[27] D. DeMille. Quantum computation with trapped polar molecules. *Phys. Rev. Lett.*, 88:067901, 2002.

[28] A. Andre, D. DeMille, J. M. Doyle, M. D. Lukin, S. E. Maxwell, P. Rabl, R. J. Schoelkopf, and P. Zoller. A coherent all-electrical interface between polar

molecules and mesoscopic superconducting resonators. *Nat Phys*, 2(9):636–642, 09 2006.

[29] M. R. Tarbutt, H. L. Bethlem, J. J. Hudson, V. L. Ryabov, V. A. Ryzhov, B. E. Sauer, G. Meijer, and E. A. Hinds. Slowing heavy, ground-state molecules using an alternating gradient decelerator. *Phys. Rev. Lett.*, 92(17):173002, Apr 2004.

[30] H. L. Bethlem, G. Berden, and G. Meijer. Decelerating neutral dipolar molecules. *Phys. Rev. Lett.*, 83(8):1558, 1999.

[31] Hendrick L. Bethlem, Floris M. H. Crompvoets, Rienk T. Jongma, Sebastiaan Y. T. van de Meerakker, and Gerard Meijer. Deceleration and trapping of ammonia using time-varying electric fields. *Phys. Rev. A*, 65:053416, May 2002.

[32] Sebastiaan Y. T. van de Meerakker, Paul H. M. Smeets, Nicolas Vanhaecke, Rienk T. Jongma, and Gerard Meijer. Deceleration and electrostatic trapping of OH radicals. *Phys. Rev. Lett.*, 94:023004, Jan 2005.

[33] Steven Hoekstra, Markus Metsälä, Peter C. Zieger, Ludwig Scharfenberg, Joop J. Gilijamse, Gerard Meijer, and Sebastiaan Y. T. van de Meerakker. Electrostatic trapping of metastable NH molecules. *Phys. Rev. A*, 76:063408, Dec 2007.

[34] S. D. Hogan, A. W. Wiederkehr, H. Schmutz, and F. Merkt. Magnetic trapping of hydrogen after multistage Zeeman deceleration. *Phys. Rev. Lett.*, 101:143001, Sep 2008.

[35] S. Chervenkov, X. Wu, J. Bayerl, A. Rohlfes, T. Gantner, M. Zeppenfeld, and G. Rempe. Continuous centrifuge decelerator for polar molecules. *Phys. Rev. Lett.*, 112:013001, Jan 2014.

[36] D. J. Wineland, R. E. Drullinger, and F. L. Walls. Radiation-pressure cooling of bound resonant absorbers. *Phys. Rev. Lett.*, 40:1639–1642, Jun 1978.

[37] William D. Phillips and Harold Metcalf. Laser deceleration of an atomic beam. *Phys. Rev. Lett.*, 48:596–599, Mar 1982.

[38] M. H. Anderson, J. R. Ensher, M. R. Matthews, C. E. Wieman, and E. A. Cornell. Observation of Bose-Einstein condensation in a dilute atomic vapor. *Science*, 269(5221):198–201, 1995.

[39] V. Zhelyazkova, A. Cournol, T. E. Wall, A. Matsushima, J. J. Hudson, E. A. Hinds, M. R. Tarbutt, and B. E. Sauer. Laser cooling and slowing of CaF molecules. *Phys. Rev. A*, 89:053416, May 2014.

[40] Matthew T. Hummon, Mark Yeo, Benjamin K. Stuhl, Alejandra L. Collopy, Yong Xia, and Jun Ye. 2D magneto-optical trapping of diatomic molecules. *Phys. Rev. Lett.*, 110:143001, Apr 2013.

[41] J. F. Barry, D. J. McCarron, E. B. Norrgard, M. H. Steinecker, and D. DeMille. Magneto-optical trapping of a diatomic molecule. *Nature*, 512(7514):286–289, 08 2014.

[42] Alisdair O. G. Wallis and Jeremy M. Hutson. Production of ultracold NH molecules by sympathetic cooling with Mg. *Phys. Rev. Lett.*, 103:183201, Oct 2009.

[43] Alisdair O.G. Wallis, Edward J.J. Longdon, Piotr S. Zuchowski, and Jeremy M. Hutson. The prospects of sympathetic cooling of NH molecules with Li atoms. *The European Physical Journal D*, 65(1-2):151–160, 2011.

[44] S.K. Tokunaga, W. Skomorowski, P.S. uchowski, R. Moszynski, J.M. Hutson, E.A. Hinds, and M.R. Tarbutt. Prospects for sympathetic cooling of molecules in electrostatic, ac and microwave traps. *The European Physical Journal D*, 65(1-2):141–149, 2011.

[45] Nicholas R. Hutzler, Hsin-I Lu, and John M. Doyle. The buffer gas beam: An intense, cold, and slow source for atoms and molecules. *Chemical Reviews*, 112(9):4803–4827, 2012. PMID: 22571401.

[46] Martin Zeppenfeld, Barbara G. U. Englert, Rosa Glockner, Alexander Prehn, Manuel Mielenz, Christian Sommer, Laurens D. van Buuren, Michael Motsch, and Gerhard Rempe. Sisyphus cooling of electrically trapped polyatomic molecules. *Nature*, 491(7425):570–573, 11 2012.

[47] Benjamin K. Stuhl, Matthew T. Hummon, Mark Yeo, Goulven Quemener, John L. Bohn, and Jun Ye. Evaporative cooling of the dipolar hydroxyl radical. *Nature*, 492(7429):396–400, 12 2012.

[48] L. D. Carr, D. DeMille, R. V. Krems, and J. Ye. Cold and ultracold molecules: science, technology and applications. *New. J. Phys.*, 11:055049, 2009.

[49] A. N. Nikolov, J. R. Ensher, E. E. Eyler, H. Wang, W. C. Stwalley, and P. L. Gould. Efficient production of ground-state potassium molecules at sub-mK temperatures by two-step photoassociation. *Phys. Rev. Lett.*, 84:246–249, Jan 2000.

[50] Toshihiko Shimasaki, Michael Bellos, C. D. Bruzewicz, Zack Lasner, and David DeMille. Production of rovibronic-ground-state RbCs molecules via two-photon-cascade decay. *Phys. Rev. A*, 91:021401, Feb 2015.

[51] Marko Gacesa, Subhas Ghosal, Jason N. Byrd, and Robin Côté. Feshbach-optimized photoassociation of ultracold ^{6}Li^{87}Rb molecules with short pulses. *Phys. Rev. A*, 88:063418, Dec 2013.

[52] Sourav Dutta, John Lorenz, Adeel Altaf, D. S. Elliott, and Yong P. Chen. Photoassociation of ultracold LiRb* molecules: Observation of high efficiency and unitarity-limited rate saturation. *Phys. Rev. A*, 89:020702, Feb 2014.

[53] K. E. Strecker, G. B. Partridge, and R. G. Hulet. Conversion of an atomic Fermi gas to a long-lived molecular bose gas. *Phys. Rev. Lett.*, 91(8):080406, 2003.

[54] M. W. Zwierlein, C. A. Stan, C. H. Schunck, S. M. F. Raupach, S. Gupta, Z. Hadzibabic, and W. Ketterle. Observation of Bose-Einstein condensation of molecules. *Phys. Rev. Lett.*, 91(25):250401, 2003.

[55] K. Xu, T. Mukaiyama, J. R. Abo-Shaeer, J. K. Chin, D. E. Miller, and W. Ketterle. Formation of quantum-degenerate sodium molecules. *Phys. Rev. Lett.*, 91(21):210402, 2003.

[56] C. A. Regal, C. Ticknow, J. L. Bohn, and D. S. Jin. Creation of ultracold molecules from a Fermi gas of atoms. *Nature*, 424:47, 2003.

[57] E. A. Donley, N. R. Claussen, S. T. Thompson, and C. E. Wieman. Atom-molecule coherence in a Bose-Einstein condensate. *Nature*, 417:529–533, 2002.

[58] S. Dürr, T. Volz, A. Marte, and G. Rempe. Observation of molecules produced from a Bose-Einstein condensate. *Phys. Rev. Lett.*, 92(2):020406, 2004.

[59] Jens Herbig, Tobias Kraemer, Michael Mark, Tino Weber, Cheng Chin, Hanns-Christoph Naegerl, and Rudolf Grimm. Preparation of a pure molecular quantum gas. *Science*, 301(5639):1510–1513, 2003.

[60] K.-K. Ni, S. Ospelkaus, M. H. G. de Miranda, A. Pe'er, B. Neyenhuis, J. J. Zirbel, S. Kotochigova, P. S. Julienne, D. S. Jin, and J. Ye. A high phase-space-density gas of polar molecules. *Science*, 322(5899):231–235, 2008.

[61] F. M. Spiegelhalder, A. Trenkwalder, D. Naik, G. Kerner, E. Wille, G. Hendl, F. Schreck, and R. Grimm. All-optical production of a degenerate mixture of ^{6}Li and ^{40}K and creation of heteronuclear molecules. *Phys. Rev. A*, 81:043637, Apr 2010.

[62] Myoung-Sun Heo, Tout T. Wang, Caleb A. Christensen, Timur M. Rvachov, Dylan A. Cotta, Jae-Hoon Choi, Ye-Ryoung Lee, and Wolfgang Ketterle. Formation of ultracold fermionic NaLi Feshbach molecules. *Phys. Rev. A*, 86:021602, Aug 2012.

[63] Cheng-Hsun Wu, Jee Woo Park, Peyman Ahmadi, Sebastian Will, and Martin W. Zwierlein. Ultracold Fermionic Feshbach molecules of ^{23}Na^{40}**K**. *Phys. Rev. Lett.*, 109:085301, Aug 2012.

[64] Michael P. Köppinger, Daniel J. McCarron, Daniel L. Jenkin, Peter K. Molony, Hung-Wen Cho, Simon L. Cornish, C. Ruth Le Sueur, Caroline L. Blackley, and Jeremy M. Hutson. Production of optically trapped ^{87}RbCs Feshbach molecules. *Phys. Rev. A*, 89:033604, Mar 2014.

[65] Tetsu Takekoshi, Lukas Reichsöllner, Andreas Schindewolf, Jeremy M. Hutson, C. Ruth Le Sueur, Olivier Dulieu, Francesca Ferlaino, Rudolf Grimm, and Hanns-Christoph Nägerl. Ultracold dense samples of dipolar RbCs molecules in the rovibrational and hyperfine ground state. *Phys. Rev. Lett.*, 113:205301, Nov 2014.

[66] Alexander Khramov, Anders Hansen, William Dowd, Richard J. Roy, Constantinos Makrides, Alexander Petrov, Svetlana Kotochigova, and Subhadeep Gupta. Ultracold heteronuclear mixture of ground and excited state atoms. *Phys. Rev. Lett.*, 112:033201, Jan 2014.

[67] Hideaki Hara, Hideki Konishi, Shuta Nakajima, Yosuke Takasu, and Yoshiro Takahashi. A three-dimensional optical lattice of ytterbium and lithium atomic gas mixture. *Journal of the Physical Society of Japan*, 83(1):014003, 2014.

[68] Frank Munchow, Cristian Bruni, Maximilian Madalinski, and Axel Gorlitz. Two-photon photoassociation spectroscopy of heteronuclear YbRb. *Phys. Chem. Chem. Phys.*, 13:18734–18737, 2011.

[69] Simon Stellmer, Benjamin Pasquiou, Rudolf Grimm, and Florian Schreck. Creation of ultracold Sr_2 molecules in the electronic ground state. *Phys. Rev. Lett.*, 109:115302, Sep 2012.

[70] T Lahaye, C Menotti, L Santos, M Lewenstein, and T Pfau. The physics of dipolar bosonic quantum gases. *Reports on Progress in Physics*, 72(12):126401, 2009.

[71] Cheng Chin, Rudolf Grimm, Paul Julienne, and Eite Tiesinga. Feshbach resonances in ultracold gases. *Rev. Mod. Phys.*, 82:1225–1286, Apr 2010.

[72] Juris Ulmanis, Johannes Deiglmayr, Marc Repp, Roland Wester, and Matthias Weidemller. Ultracold molecules formed by photoassociation: Heteronuclear dimers, inelastic collisions, and interactions with ultrashort laser pulses. *Chemical Reviews*, 112(9):4890–4927, 2012. PMID: 22931226.

[73] Kevin M. Jones, Eite Tiesinga, Paul D. Lett, and Paul S. Julienne. Ultracold photoassociation spectroscopy: Long-range molecules and atomic scattering. *Rev. Mod. Phys.*, 78:483–535, May 2006.

[74] C. J. Foot. *Atomic Physics*. Oxford University Press, 2005.

[75] J. O. Stack. *An Ultra-Cold Lithium Source For Investigating Cold Dipolar Gases*. PhD thesis, Imperial College London, September 2010.

[76] J.E. Sansonetti, W.C. Martin, and S.L. Young. Handbook of basic atomic spectroscopic data. Website, 2005.

[77] T. Kuwamoto, K. Honda, Y. Takahashi, and T. Yabuzaki. Magneto-optical trapping of Yb atoms using an intercombination transition. *Phys. Rev. A*, 60(2):R745–R748, Aug 1999.

[78] U.D. Rapol, A. Krishna, A. Wasan, and V. Natarajan. Laser cooling and trapping of Yb from a thermal source. *The European Physical Journal D - Atomic, Molecular, Optical and Plasma Physics*, 29(3):409–414, 2004.

[79] Herman Feshbach. Unified theory of nuclear reactions. *Annals of Physics*, 5(4):357 – 390, 1958.

[80] T. Köhler, K. Góral, and P. S. Julienne. Production of cold molecules via magnetically tuneable Feshbach resonances. *Rev. Mod. Phys.*, 78(4):1311–1361, Dec 2006.

[81] A. J. Moerdijk, B. J. Verhaar, and A. Axelsson. Resonances in ultracold collisions of ^{6}Li, ^{7}Li, and ^{23}Na. *Phys. Rev. A*, 51:4852–4861, Jun 1995.

[82] Eddy Timmermans, Paolo Tommasini, Mahir Hussein, and Arthur Kerman. Feshbach resonances in atomic Bose-Einstein condensates. *Physics Reports*, 315(13):199 – 230, 1999.

[83] F. A. van Abeelen and B. J. Verhaar. Time-dependent Feshbach resonance scattering and anomalous decay of a Na Bose-Einstein condensate. *Phys. Rev. Lett.*, 83:1550–1553, Aug 1999.

[84] F. H. Mies, E. Tiesinga, and P. S. Julienne. Manipulation of Feshbach resonances in ultracold atomic collisions using time-dependent magnetic fields. *Phys. Rev. A*, 61:022721, Jan 2000.

[85] Markus Debatin, Tetsu Takekoshi, Raffael Rameshan, Lukas Reichsollner, Francesca Ferlaino, Rudolf Grimm, Romain Vexiau, Nadia Bouloufa, Olivier Dulieu, and Hanns-Christoph Nagerl. Molecular spectroscopy for ground-state transfer of ultracold RbCs molecules. *Phys. Chem. Chem. Phys.*, 13:18926–18935, 2011.

[86] Daniel A. Brue and Jeremy M. Hutson. Prospects of forming ultracold molecules in $^2\sigma$ states by magnetoassociation of alkali-metal atoms with Yb. *Phys. Rev. A*, 87:052709, May 2013.

[87] D. Jaksch, V. Venturi, C.I. Cirac, C.J. William, and P. Zoller. Creation of a molecular condensate by dynamically melting a Mott insulator. *Phys. Rev. Lett.*, 89(4):040402, 2002.

[88] F. Lang, K. Winkler, C. Strauss, R. Grimm, and J. Hecker Denschlag. Ultracold triplet molecules in the rovibrational ground state. *Phys. Rev. Lett.*, 101:133005, Sep 2008.

[89] Edmund R. Meyer and John L. Bohn. Electron electric-dipole-moment searches based on alkali-metal- or alkaline-earth-metal-bearing molecules. *Phys. Rev. A*, 80:042508, Oct 2009.

[90] G. Scoles. *Atomic and Molecular Beam Methods, Vol. 1.* Oxford University Press, UK,1988, 1988.

[91] C. B. Alcock, V. P. Itkin, and M. K. Horrigan. Vapour pressure equations for the metallic elements: 298 - 2500K. *Canadian Metallurgical Quarterly*, 23(3):309–313, 1984.

[92] H. Metcalf and P. van der Straten. *Laser Cooling and Trapping.* Springer, 1999.

[93] C. F. Bohren and D. R. Huffman. *Absorption and scattering of light by small particles.* New York; Chichester: Wiley, 1998.

[94] J. Millen. *A cold strontium Rydberg gas.* PhD thesis, Durham University, 2011.

[95] Anders H. Hansen, Alexander Y. Khramov, William H. Dowd, Alan O. Jamison, Benjamin Plotkin-Swing, Richard J. Roy, and Subhadeep Gupta. Production of quantum-degenerate mixtures of ytterbium and lithium with controllable interspecies overlap. *Phys. Rev. A*, 87:013615, Jan 2013.

[96] Vladan Vuletić, Cheng Chin, Andrew J. Kerman, and Steven Chu. Degenerate raman sideband cooling of trapped cesium atoms at very high atomic densities. *Phys. Rev. Lett.*, 81:5768–5771, Dec 1998.

[97] Fabrizio Bertinetto, P. Cordiale, Gianluca Galzerano, and Elio Bava. Frequency stabilization of DBR diode laser against Cs absorption lines at 852 nm using the modulation transfer method. *Instrumentation and Measurement, IEEE Transactions on*, 50(2):490–492, Apr 2001.

[98] D. J. McCarron. *A Quantum Degenerate Mixture of ^{87}Rb and ^{133}Cs.* PhD thesis, Durham University, 2011.

[99] G.C. Bjorklund, M.D. Levenson, W. Lenth, and C. Ortiz. Frequency modulation (FM) spectroscopy. *Applied Physics B*, 32(3):145–152, 1983.

[100] D J McCarron, S A King, and S L Cornish. Modulation transfer spectroscopy in atomic rubidium. *Measurement Science and Technology*, 19(10):105601, 2008.

[101] C. G. Townsend, N. H. Edwards, C. J. Cooper, K. P. Zetie, C. J. Foot, A. M. Steane, P. Szriftgiser, H. Perrin, and J. Dalibard. Phase-space density in the magneto-optical trap. *Phys. Rev. A*, 52:1423–1440, Aug 1995.

[102] C.S. Adams and A.I. Ferguson. Tunable narrow linewidth ultra-violet light generation by frequency doubling of a ring Ti:sapphire laser using lithium tri-borate in an external enhancement cavity. *Optics Communications*, 90(13):89 – 94, 1992.

[103] Marco Pizzocaro, Davide Calonico, Pablo Cancio Pastor, Jacopo Catani, Giovanni A. Costanzo, Filippo Levi, and Luca Lorini. Efficient frequency doubling at 399 nm. *Appl. Opt.*, 53(16):3388–3392, Jun 2014.

[104] C. Abou-Jaoudeh, C. Bruni, F. Baumer, and A. Gorlitz. A compact source of ultracold ytterbium for an optical lattice clock. In *Frequency Control Symposium, 2009 Joint with the 22nd European Frequency and Time forum. IEEE International*, pages 756–759, April 2009.

[105] Kaduki Komori, Yosuke Takasu, Mitsutaka Kumakura, Yoshiro Takahashi, and Tsutomu Yabuzaki. Injection-locking of blue laser diodes and its application to the laser cooling of neutral ytterbium atoms. *Japanese Journal of Applied Physics*, 42(8R):5059, 2003.

[106] Chang Yong Park and Tai Hyun Yoon. Frequency stabilization of injection-locked violet laser diode with doppler-free absorption signal of ytterbium. *Japanese Journal of Applied Physics*, 42(7A):L754, 2003.

[107] Chang Yong Park, Dai-Hyuk Yu, Won-Kyu Lee, Sang Eon Park, and E.B. Kim. 556 nm light generation by frequency doubling of a diode laser amplifed Yb-doped fiber amplifer for precision spectroscopy of ytterbium atoms. In *Precision Electromagnetic Measurements Digest, 2008. CPEM 2008. Conference on*, pages 186–187, June 2008.

[108] S. Uetake, A. Yamaguchi, S. Kato, and Y. Takahashi. High power narrow linewidth laser at 556 nm for magneto-optical trapping of ytterbium. *Applied Physics B*, 92(1):33–35, 2008.

[109] Carl E. Wieman and Leo Hollberg. Using diode lasers for atomic physics. *Review of Scientific Instruments*, 62(1):1–20, 1991.

[110] C. J. Hawthorn, K. P. Weber, and R. E. Scholten. Littrow configuration tunable external cavity diode laser with fixed direction output beam. *Review of Scientific Instruments*, 72(12):4477–4479, 2001.

[111] Huanqian Loh, Yu-Ju Lin, Igor Teper, Marko Cetina, Jonathan Simon, James K. Thompson, and Vladan Vuletić. Influence of grating parameters on the linewidths of external-cavity diode lasers. *Appl. Opt.*, 45(36):9191–9197, Dec 2006.

[112] R.F. Kazarinov and C.H. Henry. The relation of line narrowing and chirp reduction resulting from the coupling of a semiconductor laser to passive resonator. *Quantum Electronics, IEEE Journal of*, 23(9):1401–1409, Sep 1987.

[113] R. Lang. Injection locking properties of a semiconductor laser. *Quantum Electronics, IEEE Journal of*, 18(6):976–983, Jun 1982.

[114] S. Wieczorek, B. Krauskopf, T.B. Simpson, and D. Lenstra. The dynamical complexity of optically injected semiconductor lasers. *Physics Reports*, 416(12):1 – 128, 2005.

[115] P C De Jagher, W A van der Graaf, and D Lenstra. Relaxation-oscillation phenomena in an injection-locked semiconductor laser. *Quantum and Semiclassical Optics: Journal of the European Optical Society Part B*, 8(4):805, 1996.

[116] John H. T. Burke, Ofir Garcia, K. Jeramy Hughes, Brian Livedalen, and Charles A. Sackett. Compact implementation of a scanning transfer cavity lock. *Review of Scientific Instruments*, 76(11):–, 2005.

[117] William D. Phillips and Harold Metcalf. Laser deceleration of an atomic beam. *Phys. Rev. Lett.*, 48:596–599, Mar 1982.

[118] John Prodan, Alan Migdall, William D. Phillips, Ivan So, Harold Metcalf, and Jean Dalibard. Stopping atoms with laser light. *Phys. Rev. Lett.*, 54:992–995, Mar 1985.

[119] S. C. Bell, M. Junker, M. Jasperse, L. D. Turner, Y.-J. Lin, I. B. Spielman, and R. E. Scholten. A slow atom source using a collimated effusive oven and a single-layer variable pitch coil Zeeman slower. *Rev. Sci. Instrum.*, 81(1):013105, 2010.

[120] P. Cheiney, O. Carraz, D. Bartoszek-Bober, S. Faure, F. Vermersch, C. M. Fabre, G. L. Gattobigio, T. Lahaye, D. Guery-Odelin, and R. Mathevet. A Zeeman slower design with permanent magnets in a Halbach configuration. *Rev. Sci. Instrum.*, 82(6):063115, 2011.

[121] M. Okano, H. Hara, M. Muramatsu, K. Doi, S. Uetake, Y. Takasu, and Y. Takahashi. Simultaneous magneto-optical trapping of lithium and ytterbium atoms towards production of ultracold polar molecules. *Applied Physics B: Lasers and Optics*, 98:691–696, 2010. 10.1007/s00340-009-3728-0.

[122] Eric Wille. *Preparation of an Optically Trapped Fermi-Fermi Mixture of ^6Li and ^{40}K Atoms and Characterization of the Interspecies Interactions by Feshbach Spectroscopy.* PhD thesis, Universitat Innsbruck, 2009.

[123] G. Edward Marti, Ryan Olf, Enrico Vogt, Anton Öttl, and Dan M. Stamper-Kurn. Two-element Zeeman slower for rubidium and lithium. *Phys. Rev. A*, 81:043424, Apr 2010.

[124] A. Paris-Mandoki, M. D. Jones, J. Nute, J. Wu, S. Warriar, and L. Hackermller. Versatile cold atom source for multi-species experiments. *Review of Scientific Instruments*, 85(11):–, 2014.

[125] E. L. Raab, M. Prentiss, Alex Cable, Steven Chu, and D. E. Pritchard. Trapping of neutral sodium atoms with radiation pressure. *Phys. Rev. Lett.*, 59:2631–2634, Dec 1987.

[126] J. Dalibard and C. Cohen-Tannoudji. Laser cooling below the Doppler limit by polarization gradients: simple theoretical models. *J. Opt. Soc. Am. B*, 6(11):2023–2045, Nov 1989.

[127] Pantita Palittapongarnpim. *Characterization of Magneto-optical Trap For Experiments in Light-Atom Interfacing.* PhD thesis, University of Calgary, 2012.

[128] G. Hillenbrand, C. J. Foot, and K. Burnett. Heating due to long-range photon exchange interactions between cold atoms. *Phys. Rev. A*, 50:1479–1489, Aug 1994.

[129] Marin Pichler, Hongmin Chen, and William C. Stwalley. Photoassociation spectroscopy of ultracold Cs below the $^6P_{1/2}$ limit. *The Journal of Chemical Physics*, 121(4):1796–1801, 2004.

[130] E. R. I. Abraham, W. I. McAlexander, C. A. Sackett, and Randall G. Hulet. Spectroscopic determination of the s-wave scattering length of lithium. *Phys. Rev. Lett.*, 74:1315–1318, Feb 1995.

[131] M. W. Zwierlein, C. A. Stan, C. H. Schunck, S. M. F. Raupach, A. J. Kerman, and W. Ketterle. Condensation of pairs of fermionic atoms near a Feshbach resonance. *Phys. Rev. Lett.*, 92:120403, Mar 2004.

Appendix A

Appendix outlining the code used for the numerical simulations of the Zeeman slower.

Function that calculates the radius of curvature of beam at a given point on the axis z. It depends om the position of the waist of the beam and the Rayleigh range. Any symbol that is not explicitly explained is the same given in the equations for the Zeeman slower.

$$\textbf{radiusOfCurvature[z\_]:=}$$

$$\textbf{(}z\textbf{ + laserWaistToSlowerEntrance) (1 + (rangeRayleigh/(}z\textbf{ + laserWaistToSlowerEntrance))}^{\textbf{2}}\textbf{)}$$

Function to calculate the spot size of the beam at a postion z, given waist, the position of the waist and the Rayleigh range.

$$\textbf{spotSize[z\_]:=waist} * \sqrt{\textbf{1 + ((}z\textbf{ + laserWaistToSlowerEntrance)/rangeRayleigh)}^{\textbf{2}}}$$

Function to calcualte the saturation parameter s of the Zeeman beam at any position (ρ, z) with a given power, where z is the position along the axis and ρ is the transverse distance from the axis. The saturationIntensity is the the saturation intensity of the transition I_s.

$$\textbf{saturationParameter[power\_, }\rho\textbf{\_, z\_]:=}$$

$$\textbf{2power /(}\pi\textbf{spotSize[}z\textbf{]}^{\textbf{2}}\textbf{saturationIntensity) Exp [}-\textbf{2}\rho^{\textbf{2}}\textbf{/spotSize[}z\textbf{]}^{\textbf{2}}\textbf{]}$$

Calculates a vector of the direction of a photon in a beam given cartesian coordinates (x, y, z).

$$\textbf{photonMomentumComponents[x\_, y\_, z\_]:=Module[\{}R\textbf{\},}$$

$$R\textbf{ = radiusOfCurvature[}z\textbf{];}$$

$$\left\{x/R, y/R, \sqrt{1 - \left(x^2 + y^2\right)/R^2}\right\}\ \Big]$$

Calculates the detuning from transtion for any atom travelling at velocity v at a

external magnetic field B with an overall laser detuning δ_0.

$$\mathbf{detuning[\delta 0\_, B\_, v\_]:=\delta 0 - \Delta\mu B/\hbar - 2\pi v/\lambda}$$

Calcualtes the scattering rate R for an atom travelling at velocity v at a external magnetic field B. The overall laser laser detuning $\delta_0$and saturation parameter s.

$$\mathbf{scatterRate[s\_, \delta 0\_, B\_, v\_]:=\frac{s\Gamma/2}{1+s+4detuning[\delta 0, B, v]^2/\Gamma^2}}$$

The average number of scattered photons in a time interval τ.

$$\mathbf{meanPhotonsScattered[s\_, \delta 0\_, B\_, v\_, \tau\_]:=scatterRate[s, \delta 0, B, v]\tau}$$

Angular distributions to ensure isotropic spontaneous emission events given a polar coordinate system. θ is the polar angle and ϕ is the azimuthal angle.

$$\mathbf{\theta Distrib =}$$

$$\mathbf{Flatten[Table[RandomReal[\{k\pi/200, (k+1)\pi/200\}, Round[1000Sin[(k+1/2)\pi/200]]],}$$

$$\mathbf{\{k, 0, 199\}]];}$$

$$\mathbf{\phi Distrib = RandomReal[\{0, 2\pi\}, Length[\theta Distrib]];}$$

The velocity change of an atom due to n spontaneous emission events.

$$\mathbf{diffusion[n\_]:=Module[\{n1, \theta, \phi, v, vtot\},}$$

$$\mathbf{vtot = \{0, 0, 0\};}$$

$$\mathbf{Do[n1 = RandomInteger[\{1, Length[\theta Distrib]\}, 2];}$$

$$\mathbf{\theta = \theta Distrib[[n1[[1]]]];}$$

$$\mathbf{\phi = \phi Distrib[[n1[[2]]]];}$$

$$\mathbf{v = h/(M\lambda)\{Sin[\theta]Cos[\phi], Sin[\theta]Sin[\phi], Cos[\theta]\};}$$

$$\mathbf{vtot = vtot + v, \{n\}];}$$

$$\mathbf{vtot]}$$

As the number of scattering events is given by a poisson distribution this function gives 100 random numbers for mean scattering numbers between 0.1 and 200 with a step interval 0.1.

$$\mathbf{randomSet = RandomInteger[PoissonDistribution[\#], 100]\&/@Range[0.1, 200, 0.1];}$$

Takes a number from the random the randomSet for a mean scattering number x, if

x is between 0.1 and 200. If not it takes a random number from a Poisson distribution. This is done because selectring a random number from a Poisson distribution is slow compared to just picking a random number out of a set.

```
fastRandom[x_]:=Module[{q, r},
If[x < 0.1||x > 200, RandomInteger[PoissonDistribution[x]],
q = Round[10x];
r = RandomInteger[{1, 100}];
randomSet[[q, r]]]]
```

Function that takes the coordinates coord made up of the position and velocity of the atoms (x, y, z, v_x, v_y, v_z) , the magnetic field profile fieldFunction, the power of the beam P and the Zeeman beam detuning δ_0 to calculate the new coordinates after a time tStep. It uses the saturation parameter sz and the momentum components of the photons at the relevant position rr to calculate the mean number of scattering events mp. It calculates the velocity changes due to diffusion and outputs the new coordinates according to the emission and absorption events. It also includes a gravitational acceleration gg in the x direction.

```
oneTStep[coord_, tStep_, fieldFunction_, P_, δ0_]:=
Module[{mag, sz, rr, mp, np, diff, pmc, xnew, ynew, znew, vxnew, vynew, vznew},
mag = fieldFunction[coord[[3]]]; (* + 0.0005 * RandomReal[{-1, 1}]; *)
sz = saturationParameter [P, Sqrt[coord[[1]]^2 + coord[[2]]^2], coord[[3]]] ;
rr = Re[photonMomentumComponents[coord[[1]], coord[[2]], coord[[3]]]];
mp = Evaluate[meanPhotonsScattered[sz, δ0, mag, coord[[6]], tStep]];
Check [If [Re[mp] < 10^-10, np = 0; ,
np = fastRandom[Re[mp]]; ], Abort[]; ];
diff = diffusion[np];
pmc = -np h/(M λ) rr;
xnew = coord[[1]] + coord[[4]]tStep - 0.5 * gg * tStep^2;
ynew = coord[[2]] + coord[[5]]tStep;
```

```
znew = coord[[3]] + coord[[6]]tStep;
vxnew = coord[[4]] + pmc[[1]] + diff[[1]] − gg ∗ tStep;
vynew = coord[[5]] + pmc[[2]] + diff[[2]];
vznew = coord[[6]] + pmc[[3]] + diff[[3]];
{xnew, ynew, znew, vxnew, vynew, vznew, sz, mp}]
```

Function that stops evaluation of the program if the atom has passed the MOT region or is travelling at -10 m/s.

```
terminatedTStep[coord_, tStep_, fieldFunction_, P_, δ0_]:=
If[coord[[3]] > 0.775||coord[[6]] < −10, coord,
oneTStep[coord, tStep, fieldFunction, P, δ0]];
```

Functions that execute the full program. nTStep gives all the coordinates of every atom at every time step. nTLastStep gives only the coordinates of all the atoms after the final time step.s

```
nTStep[coord_, tStep_, fieldFunction_, P_, δ0_, n_]:=
NestList[terminatedTStep[#, tStep, fieldFunction, P, δ0]&, coord, n];
nTLastStep[coord_, tStep_, fieldFunction_, P_, δ0_, n_]:=
Nest[oneTStep[#, tStep, fieldFunction, P, δ0]&, coord, n];
```